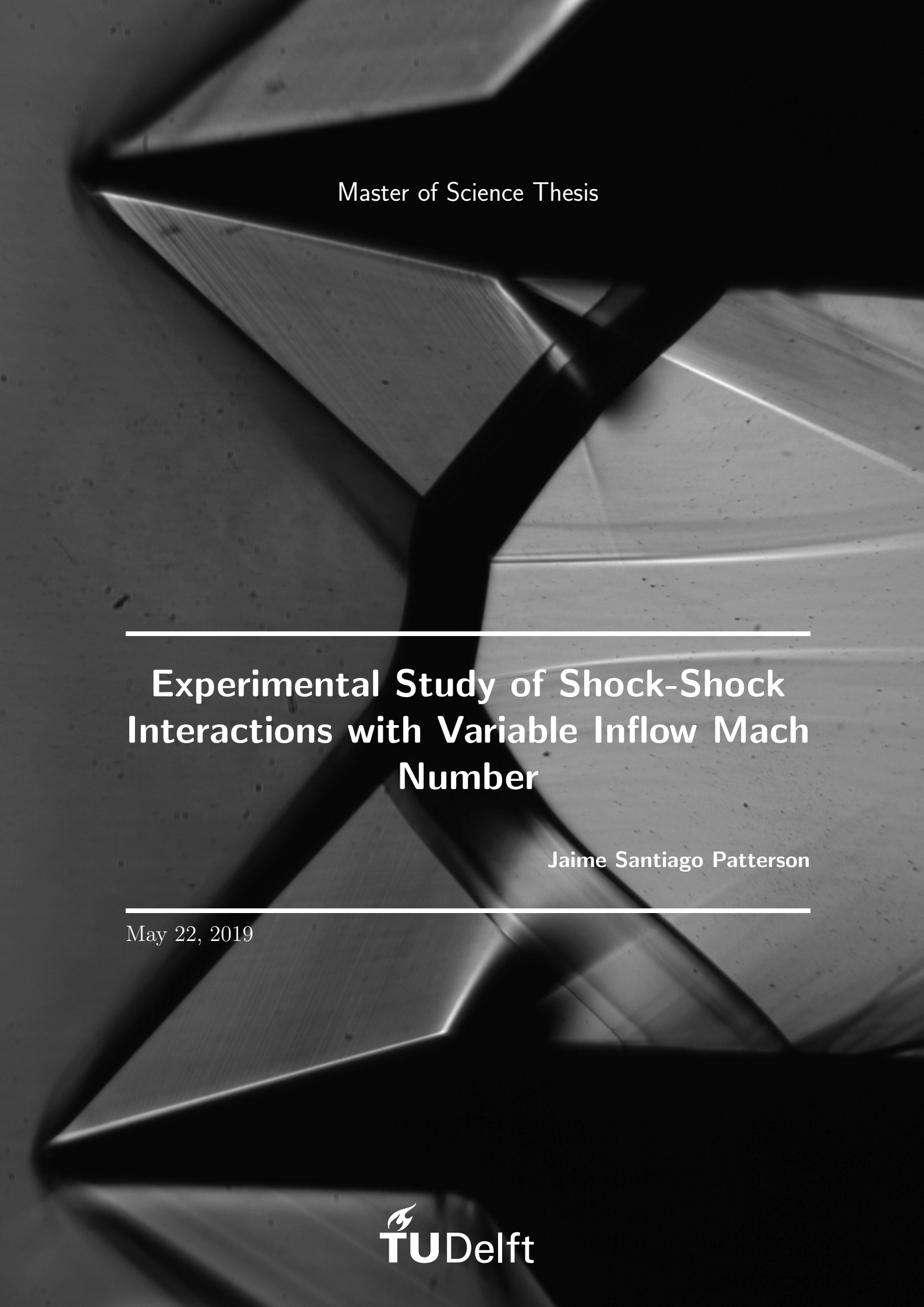

Master of Science Thesis

Experimental Study of Shock-Shock Interactions with Variable Inflow Mach Number

Jaime Santiago Patterson

May 22, 2019

TU Delft

Experimental Study of Shock-Shock Interactions with Variable Inflow Mach Number

Master of Science Thesis

For obtaining the degree of Master of Science in Aerospace Engineering
at Delft University of Technology

Jaime Santiago Patterson

May 22, 2019

Faculty of Aerospace Engineering · Delft University of Technology

Delft University of Technology

DELFT UNIVERSITY OF TECHNOLOGY
DEPARTMENT OF AERODYNAMICS

The undersigned hereby certify that they have read and recommend to the Faculty of Aerospace Engineering for acceptance the thesis entitled **"Experimental Study of Shock-Shock Interactions with Variable Inflow Mach Number"** by **Jaime Santiago Patterson** in fulfillment of the requirements for the degree of **Master of Science**.

Dated: May 22, 2019

Dr.ir. F.F.J. Schrijer

Dr.ir. B.W. van Oudheusden

Prof.dr. S. Hickel

Dr.ir. G.E. Elsinga

L. Laguarda Sánchez

Acknowledgments

This thesis represents the conclusion of not only my Master studies at Delft but also the end of a long journey that began almost seven years ago when I started my Aerospace Engineering studies. These last fourteen months have been full of happy days, such as the conference trip to Paris or the fun days in the lab, and other not so enjoyable times where nothing worked in the wind tunnel or the data would not make any sense. All of them have helped me grow as a person and an engineer and achieve things I never thought possible before embarking on this odyssey.

First of all I would like to thank my supervisors Ferry Schrijer, Bas van Oudheusden, Stefan Hickel and Luis Laguarda for offering me this fascinating topic and for your excellent guidance and support throughout the project. Special thanks to Ferry for sharing your incredible expertise in the lab and for having the patience to teach me from the very basics in the early days in the tunnel all the way to my hardest problems with my final results at the very end. All this while keeping your characteristic relaxed personality. I am also really grateful to Luis for being the best daily supervisor I could have asked for. I have to thank you for your tireless dedication and constant help and feedback. I really enjoyed our great conversations, either over a coffee in the lab or a beer in Delft. I am also thankful to Alessandro D'Aguanno for sharing with me the secrets of the TST-27 tunnel and for the fun times in Paris. I also want to thank the technical staff of the High Speed Lab, especially Frits and Peter, without whom none of the experiments would have been possible. Also thanks to Colette for your very professional help with everything.

Most of the work of this project took place in a bunker hidden under TU Delft, commonly known as The Basement. We constantly joke and complain about it, but deep down we all know it's a fantastic workplace. Special mentions go to Niels Terleth, who I will never understand how he survived as my desk neighbor and through my never ending terrible jokes and sense of humor, and Dorian Heitzig, who I met in the Introduction Program three years ago and have stuck together with through assignments, thesis and improvised internship reunions in Germany. Also thanks to Javi, for the long days in both the Basement and the Sports Center, Derek, for your inextinguishable energy, Christoph, for being one of the chillest people I know, Blanca for your always cheerful personality, Jordi, for the fun nights out in Rotterdam, Roberto, for all the crazy plans in Delft and many other friends I made inside and outside the Basement including Victor, Mart, Koen, Arun, Carlos, Ventsislav, Jonathan and Lucas, among others.

Finally and most importantly, I want to thank my parents Louise and José Luis and my brother Pablo. None of this would have been possible without your constant support and encouragement throughout the years, both through happy times and through the stressful periods when I know I wasn't the nicest person to be around.

Jaime Santiago Patterson
Delft, 22nd of May 2019

Don't Panic.

-Douglas Adams, The Hitchhiker's Guide to the Galaxy.

Abstract

An experimental investigation on shock-shock interactions has been conducted with the aim of studying the transition between Regular (RI) and Mach interactions (MI) under the condition of variable inflow Mach number. The RI contains only oblique shocks while the MI has a quasi-normal shock segment, known as the Mach stem. MI configurations generate larger total pressure losses, which is specially relevant for the design of supersonic inlets and rocket nozzles. The study was conducted in the TST-27 transonic-supersonic wind tunnel at Delft University of Technology, which allows a variation of the Mach number during a run through a flexible nozzle system. The wind tunnel model was built using two full span wedges that deflected the freestream flow to generate a shock-shock interaction. The minimum vertical distance between the wedges was kept constant throughout the runs. The Mach number was determined through continuous pressure readings in both the settling chamber and the test section. Schlieren and Focusing Schlieren systems were used to visualize the shock wave pattern. For all cases, the wind tunnel runs were initialized in the RI domain after which the Mach number was slowly decreased to the MI domain, thereby traversing the whole dual solution domain. The process was then inverted to reach again the RI domain in order to investigate a possible transition hysteresis. The Focusing Schlieren setup was capable of eliminating three-dimensional effects that contaminated the images obtained with the Schlieren visualization system. It also revealed that the main three-dimensional effect in the setup was a boundary layer detachment at the sidewalls. Schlieren visualization was used as the main quantitative flow diagnostics tool, allowing a clear view of the shock pattern and revealing the absence of any hysteresis effect. A custom built image processing software was used to obtain accurate measurements of the Mach stem height (MSH) evolution and detect transition. The MSH measurements confirmed the nonexistence of the hysteresis loop and an increase of the rate of change of the MSH with the Mach number as the deflection angle was decreased. The detected transition points between RI and MI showed a very good experimental repeatability and revealed that transition always occurred at the von Neumann condition regardless of the initial shock configuration. These results suggest that flow perturbations present in the TST-27 wind tunnel may prevent a RI from existing within the theoretical dual solution domain and thus suppressing any hysteresis loop. Further experiments and simulations are required to characterize these perturbations and fully understand the physical mechanism that triggers premature transition.

Table of Contents

List of Figures

List of Tables

Nomenclature

Acronyms

$2D$	Two-dimensional
$3D$	Three-dimensional
AR	Aspect Ratio
CFD	Computational fluid dynamics
FOV	Field of view
MI	Mach interaction
MSH	Mach stem height
RI	Regular interaction
TST	Transonic-supersonic wind tunnel

Greek symbols

θ	Wedge deflection angle
θ_N	Nominal wedge deflection angle
θ_T	Transition wedge deflection angle
δ	Flow angle
ξ	Pressure ratio across a shock wave
γ	Specific heat ratio
μ	Mach angle
α	Negative wedge angle
ε_{Min}	Minimum detectable light deflection angle
Δz	Depth of focus
λ	Wavelength
ϕ	Shock angle

Latin symbols

$2g$	Minimum vertical distance between the two wedges
A	Aperture
A_0	Inlet area of the wedge system
A^*	Critical area of the wedge system
b	Wedge span
c	Wedge chord
d	Width of dark strips on the cutoff grid
f	Focal length
h	Wedge inlet height
H_c	Cutoff grid height
H_s	Source grid size
i	Incident shock
I	Interaction point
l	Distance between focusing lens and plane of interest
l'	Distance between focusing lens and image plane
L	Distance between focusing lens and source grid
L'	Distance between focusing lens and cutoff grid
M_0	Freestream Mach number
m	Mach stem
p	Pressure
p_s	Static pressure
p_t	Total pressure
r	Reflected shock
R^2	Statistic coefficient of determination
s	Slipline
t	Time
$T_{1,2}$	Triple points
T_∞	Freestream temperature
T_t	Total temperature
u_∞	Freestream flow velocity
w	Wedge hypothenuse length
Δw	Resolution size

Chapter 1

Introduction

1.1 Introduction and motivation

Any body moving through a fluid emits pressure waves which travel at the speed of sound, defined by the properties of the fluid. When this body moves with a velocity below the speed of sound, the emitted pressure signals are capable of traveling upstream allowing the fluid to smoothly adapt to the incoming body, leading to a situation such as the one in Figure 1.1(a). In the case of supersonic flight, the emitter will travel faster than the resulting pressure signals. Under these circumstances, the fluid upstream will no longer receive any information in advance about the incoming body and a shock wave is generated leading to the situation in Figure 1.1(b). This flow feature is characterized by a sudden compression that generates a sharp increase in pressure, density, temperature and entropy. Because the thickness of a shock wave is usually in the order of the mean free path between fluid particles, it is usually considered to be an infinitesimally thin discontinuity in the flow.

The property changes of a fluid across a single steady normal or oblique shock wave are well understood and can be accurately modeled through analytic equations (see Anderson Jr. (2001), for example). The physical system becomes more complex when multiple, interacting shocks are considered. This is a very common situation that can be found in any aircraft or spacecraft traveling through the atmosphere with a Mach number higher than one. An example of this can be seen in Figure 1.2 where, due to the aircraft geometry, multiple shock waves are emitted from a single vehicle. In many relevant aerospace applications involving internal flows, the situation becomes even more complex when these shocks intersect each other, generating shock-shock interactions. Under these circumstances, past experiments have shown that it is not always possible to study the system from an analytical point of view, so more sophisticated tools are necessary.

Planar shock waves can be divided into two families: right running shocks, when they deflect the flow in a counter-clockwise direction, or left running shocks, when they do it in a

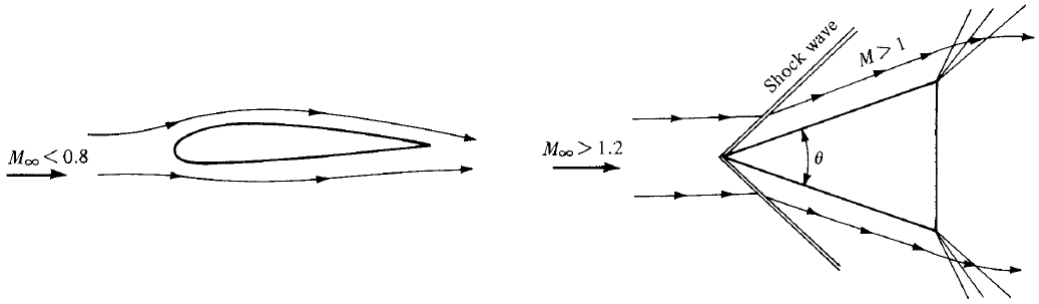

(a) Subsonic flow (b) Supersonic flow

Figure 1.1: Schematic representation of two bodies traveling below (a) and above (b) the speed of sound (Anderson Jr., 2001).

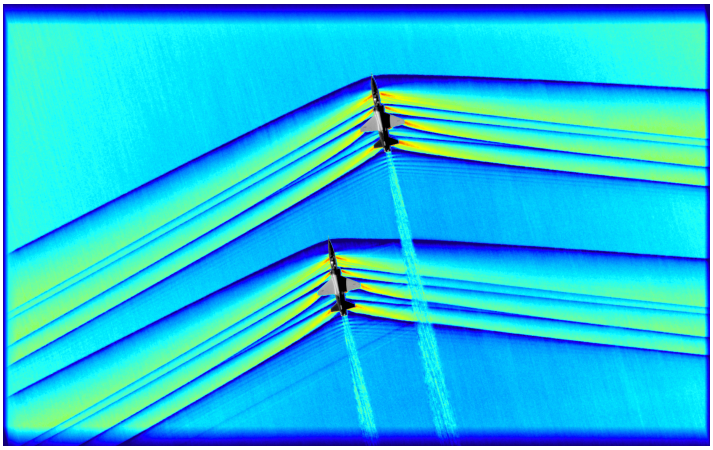

Figure 1.2: Schlieren image of two aircraft flying in a supersonic regime. Source: NASA.

clockwise direction. When two of these shocks interact, the resulting shock system depends on the nature of the intersecting shocks. If the shocks are from opposite families, two shock waves with different possible patterns, such as those shown in Figure 2.1, emanate from the interaction. This type of shock interactions are the point of focus of the current project and will be extensively studied throughout the report.

Shock-shock interactions can be found in several high speed aerodynamic applications involving internal flows. A very common one is the over-expanded jet of a rocket nozzle exhaust, where shock waves interact with each other forming a set of characteristic patterns such as those in Figure 1.3(a). Supersonic intake flows are another relevant application, shown in Figure 1.3(b). The efficient performance of these systems rely on a series of oblique shocks in order to compress the flow and reach suitable conditions for combustion. Special care must be taken when considering these flows as, for a range of parameters, the situation in Figure 1.3(b), known as the Regular interaction (RI), is not the only physical solution. Another configuration, the Mach interaction (MI), can also materialize. This configuration, shown

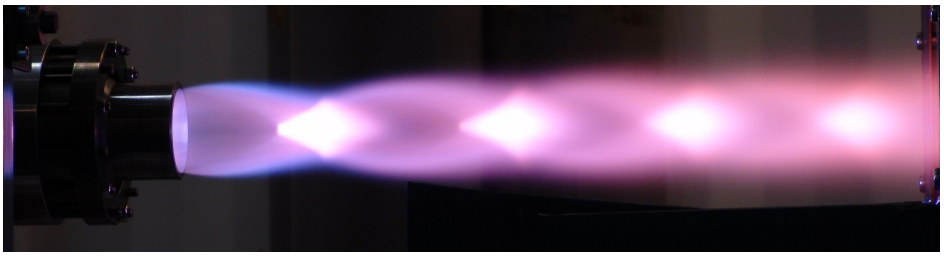

(a) Over-expanded nozzle exhaust flow. Source: https://www.spl.ch/.

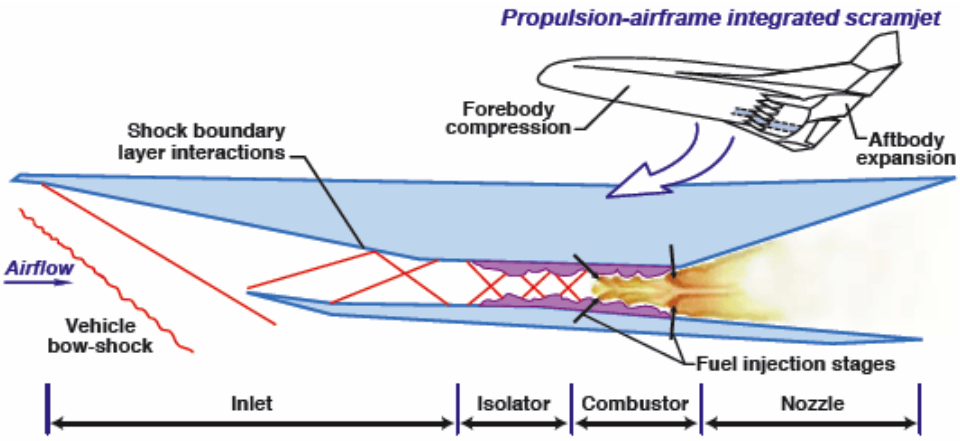

(b) Schematic of a scramjet engine. Source: NASA.

Figure 1.3: Example of two engineering applications where shock-shock interactions play an important role.

in Figure 2.1(b), is characterized by its quasi-normal shock segment at the interaction point, known as that Mach stem. This normal shock segment makes the MI considerably less efficient than the RI and can even lead to an unstart of the inlet.

Due to the complexity of this type of flow fields and despite the extensive research done on the topic over the last century, there are still some aspects, such as the transition between RI and MI or the evolution of the Mach stem, that are still not fully understood. Because of this, there is still no model that can completely predict the behavior of these physical systems. One of the biggest obstacles of space exploration is the extremely high cost and low efficiency of the current rocket engines used to propel launchers. In order to overcome this, a better understanding of the fluid structure interaction within rocket nozzles or a usage of the more futuristic scramjet engines will be required. In order to design these supersonic and hypersonic devices, a fundamental and complete understanding of the shock-shock interaction phenomenon is essential. The current project aims to contribute to the body of knowledge on this topic and expand on the existing research in this field.

1.2 Thesis Outline

Chapter 2 begins with an overview of the theoretical background necessary to understand the rest of the report. After this, the main relevant literature is presented in order to to place the current project in its appropriate research context. The research question that the current project tries to answer, which results from the previous theory and literature study, is then introduced.

Chapter 3 is then dedicated to presenting the design process followed to obtain the experimental parameter space and wind tunnel model used in the experimental campaign. This is done by first discussing the available facilities and the design of the experimental space, defined by the selected M_0, θ_1 and θ_2 values. The wind tunnel model used and the main design challenges that had to be solved to obtain it are then explained. The chapter ends with the test matrix and experimental procedure followed during the project.

Once all experimental parameters and the resulting test model are defined, the flow measurement techniques used during the experiments are shown in Chapter 4. First, the pressure measurements used to determine M_0 and the Schlieren visualization systems are presented. After this, the Focusing Schlieren setup is explained in more detail. Since it is the first Focusing Schlieren setup used at TU Delft, special attention is given to the design process and decisions followed in order to reach the final design.

The experimental results are then discussed in Chapter 5. This is done by first presenting the Focusing Schlieren results and how they compare to Schlieren visualization. After this, transition between RI and MI is studied through the Schlieren visualization images. The Mach stem evolution results are then discussed after presenting the data processing method used. Finally, the transition points between RI and MI, obtained through the Mach stem analysis, are presented. The report is concluded in Chapter 6 together with some recommendations for future work.

Chapter 2

Theoretical Background and State of the Art

Since the discovery of shock-shock interactions by Ernst Mach (Mach, 1828), this physical process has remained as a relevant topic in the field of Gas Dynamics. Thea aim of this chapter is to introduce the main theoretical tools required to understand this phenomenon and present an overview of the relevant research previously done on the topic. This will then be used to formulate the Research Question the current project attempts to answer.

2.1 Theoretical Background

When two steady, planar shock waves of opposite families intersect, a shock-shock interaction is generated. Shock interactions occur on a regular basis in high speed aerodynamic applications such as the propulsion systems of supersonic and hypersonic vehicles or the exhaust nozzles of rocket engines. To be able to progress and improve the design of this type of high speed aerodynamic devices, a complete understanding of the shock interaction phenomenon is crucial. The current section provides the reader with a general understanding of the basic theoretical background needed to understand this phenomenon. More detailed information on the topic can be found in Ben-Dor (1992), Chapman (2000) and Li et al. (1999).

2.1.1 Regular and Mach Interactions

When two intersecting shocks are of opposite families, deflecting the flow in opposite directions (clockwise and counterclockwise), the resulting interaction can be classified as either a Regular Interaction (RI), shown in Figure 2.1(a), or a Mach Interaction (MI), as in Figure 2.1(b). The former, consists of four oblique shocks, two incident, i_1 and i_2 in the Figure, and two reflected, r_1 and r_2. The two incident shocks emanate from the shock generators and intersect at the interaction point I. After this, the two reflected shocks are generated and travel downstream

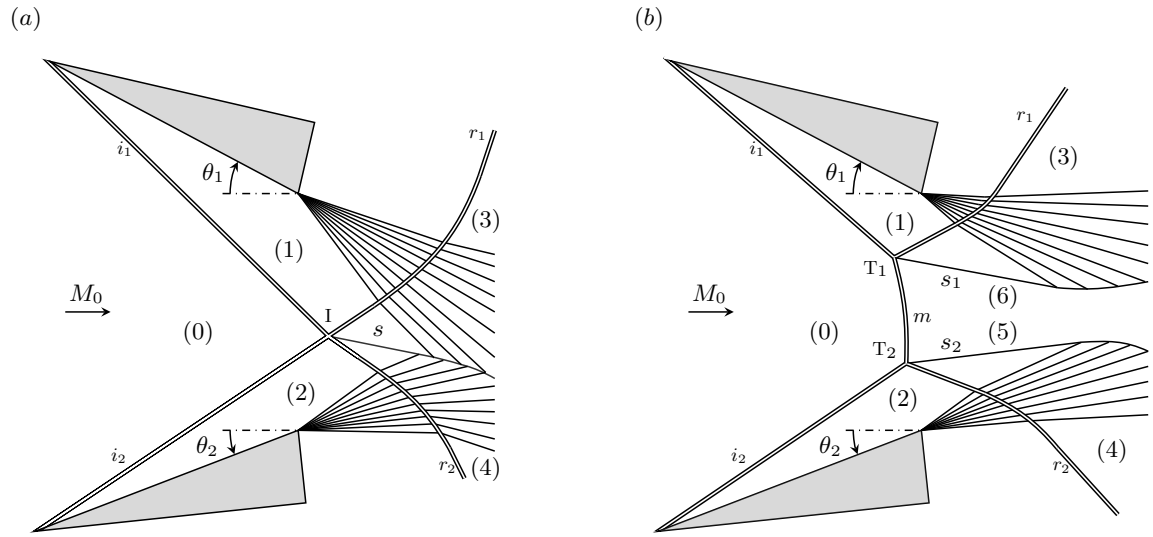

Figure 2.1: Schematic representation of a Regular Interaction (a) and a Mach Interaction (b).

until they interact with the expansion fans. At this point, they become curved due to the action of the fans. The final flow feature present in an asymmetric RI is the slipline, s in the Figure. This feature separates the two distinct domains behind the reflected shock waves with equal pressures and flow deflections but with all other intensive properties being different.

In the case of the MI, in addition to the two incident and reflected shocks, a quasi-normal shock segment, m in Figure 2.1(b), known as the Mach stem, appears in the interaction region. In this case, the two incident shocks interact at two separate points, T_1 and T_2, known as the triple points. Two sliplines are formed after the Mach stem, s_1 and s_2. It is important to notice how these two sliplines form a convergent divergent duct under the action of the expansion fans, which is essential for accelerating the flow back to supersonic speeds. This feature is required for a stable system. The reason for this is that the flow will always become subsonic after the quasi normal shock. If the resulting duct was divergent, the flow would further decelerate, creating a fluid accumulation behind the Mach stem leading to a pressure build up and an unstable system. Something similar would occur if the duct was only convergent, with the flow only capable of reaching sonic conditions leading to a similar unsteady situation. This last situation would be the result of the absence of the expansion fans.

The two RI and MI systems can also be defined through compatibility conditions. As mentioned, for a steady RI, the flow must have the same deflection and pressure across the sliplines. This can be mathematically represented as (Li et al. (1999)):

$$\theta_1 - \theta_3 = \theta_2 - \theta_4 = \delta \tag{2.1}$$

$$p_3 = p_4 \tag{2.2}$$

Where the subindices are the different regions of the flow, following the nomenclature in Figure 2.1 and δ is the flow angle behind the reflected shocks. In the case of the MI, there is a different flow deflection in regions 3 and 4. At the same time, the pressure must remain constant across the sliplines. This can all be expressed as (Li et al. (1999)):

$$\theta_1 - \theta_3 = \delta_3 \quad \theta_2 - \theta_4 = \delta_4 \tag{2.3}$$

$$p_3 = p_5 \quad p_4 = p_6 \tag{2.4}$$

Where δ_1 and δ_2 are the flow angles in regions 3 and 4, respectively, and p_5 and p_6 the pressure right across the sliplines. It is important to note that even in the symmetric case, where $p_5 = p_6$, there will always be a pressure gradient along the Mach stem direction in order to make the triple points and normal shock conditions compatible. This is what gives the Mach stem its curved shape.

2.1.2 Shock Polar Theory

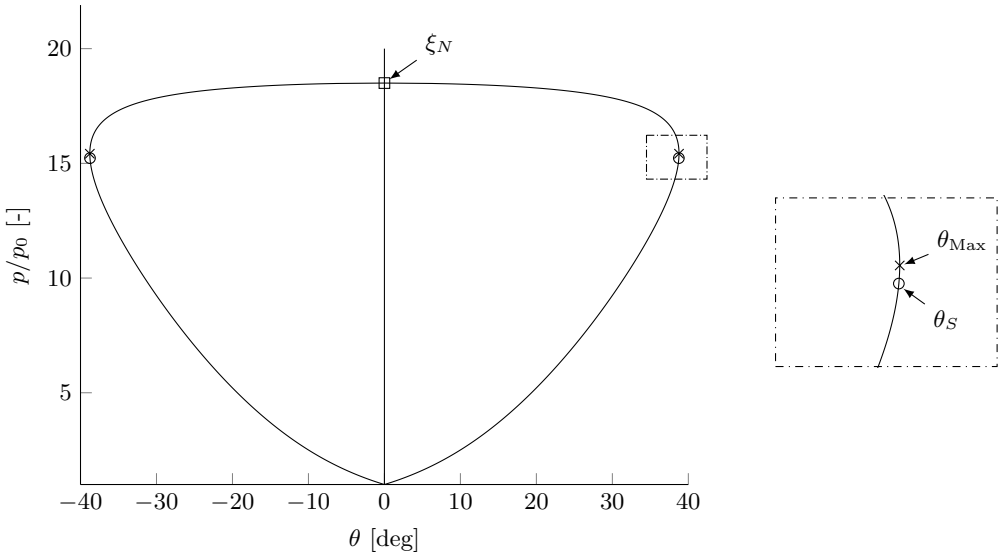

Figure 2.2: Shock polar of $M_0 = 4$ highlighting the normal shock (ξ_N), sonic (θ_S) and maximum deflection (θ_{Max}) points.

The existence of an RI or a MI for a given fluid, given by γ, is determined by three parameters: θ_1, θ_2 and M_0. A very useful tool to analyze how the combination of these parameters affects the shock system is shock polar theory, first introduced in Kawamura and Saito (1956), which uses the compatibility relations defined in terms of pressure and flow deflection. Since pressure conditions after a shock are a function of the Mach number, the flow properties, and

the deflection angle, a direct relationship can be expressed as (Han and Yin (1993)):

$$\theta = \pm f(M, \gamma, \xi) = \pm \arctan \left\{ \frac{(\xi - 1)^2 [2\gamma(M^2 - 1) - (\gamma + 1)(\xi - 1)]}{[\gamma M^2 - (\xi - 1)]^2 [2\gamma + (\gamma + 1)(\xi - 1)]} \right\}^{1/2} \tag{2.5}$$

Where ξ is the pressure ratio across a shock (p/p_0). A shock polar curve follows by computing ξ through Equation 2.5 for all θ values that satisfy $0 < |\theta| < \theta_{\text{Max}}$ for a given γ and M. θ_{Max} represents the maximum possible deflection angle for an attached shock. This way, a shock polar represents all possible pressure states after an attached shock. An example of a shock polar for $M_0 = 4$ can be seen in Figure 2.2. All shock polars intersect the y axis at two points: $p/p_0 = 1$ and $p/p_0 = \xi_N$. The former, corresponds to a Mach wave situation, where an infinitesimally weak shock produces no deflection angle or pressure jump. The second case refers the normal shock solution. There are two other important points: θ_S and θ_{Max}. The first one is the sonic condition. This point separates the strong and weak shock solutions, with all points above it corresponding to subsonic conditions after the shock and all below it to supersonic downstream conditions. The second one is the maximum deflection angle. It represents the maximum deflection angle that allows an attached shock given the inflow conditions.

Shock polars can be used to predict steady shock configurations for a given combination of deflection angles and inflow Mach number (Ben-Dor (1992), Chapman (2000)). To illustrate this, a sequence of shock polars, for different M_0 values and deflection angles fixed at $\theta_1 = 15°$, $\theta_2 = 25°$ is shown in Figure 2.1.2. These polars are obtained by plotting together the polar curves of the incident and reflected shocks. The incident curve is placed with its vertex at the (0,1) point. The shape of this polar is obtained by introducing M_0 and γ in Equation 2.5. This polar represents all possible shock wave downstream conditions for the given M_0 and γ. The vertices of the reflected polars are placed on the incident curve at $x = \theta_1$ and $x = -\theta_2$. The shape of the reflected polars is calculated by using M_1 and M_2 after the reflected shock, obtained through oblique shock relations (see Anderson Jr. (2001), for example). These polars represent all possible states downstream of the reflected shocks. In this example, due to the fixed deflection angles, the vertices of the reflected shocks are always in the same position on the incident polar. Changing M_0 results in a variation of the shape of the polar curves with higher M_0 values resulting in larger pressure jumps and larger polar curves.

Figure 2.1.2(a) shows the polar of a RI configuration at $M_0 = 3.80$. Final flow conditions are highlighted with the RI label at the intersection between the two reflected polars. This point satisfies the RI compatibility conditions presented in Equations 2.1 and 2.2. Because the two curves intersect at the final point, same pressure and flow deflections across both reflected shocks is ensured. As M_0 is decreased, the size of the polars also decreases until the condition in Figure 2.1.2(b) is reached at $M_0 = 3.17$. This point is known as the von Neumann or mechanical equilibrium condition due to the MI and RI solutions having the same pressure jump at this point. $M_0 = M_{VN}$ also represents the maximum M_0 at which a MI is physically stable. This way, both the RI and MI can coexist at this point, so the compatibility relations for the MI (Shown in Equations 2.3 and 2.4) are also satisfied here. In the case of the MI, the conditions at 5 and 6 are determined by the jump across the normal shock generated

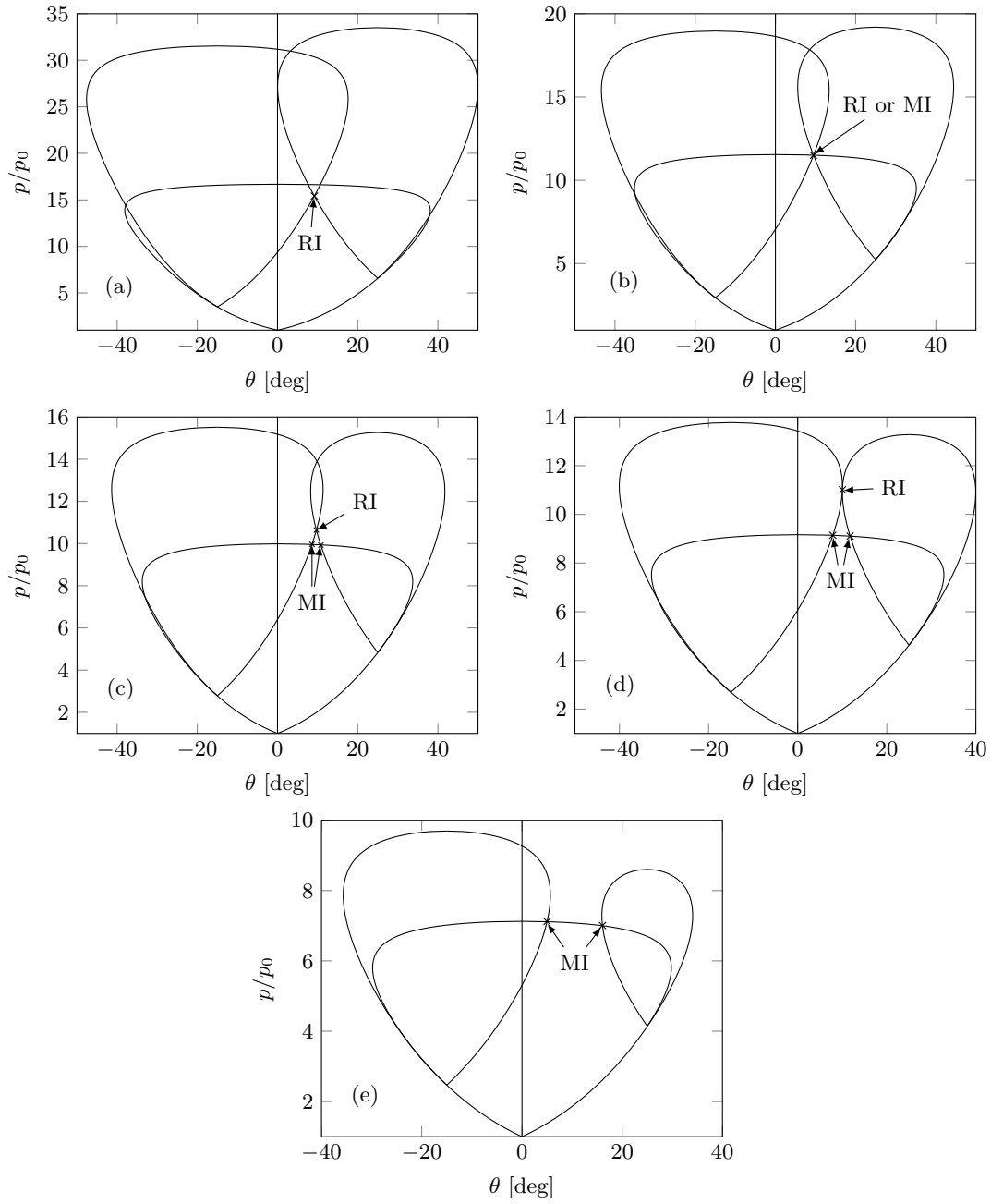

Figure 2.3: Polar examples for $\theta_1 = 15°, \theta_2 = 25°$. (a) RI polar $M_0 = 3.80$, (b) von Neumann condition polar $M_0 = 3.17$, (c) Dual solution domain polar $M_0 = 2.95$, (d) Detachment condition polar $M_0 = 2.83$, (e) MI polar $M_0 = 2.50$.

by the incident shock, which results on the final condition lying on the incident shock polar and the final configuration being determined by the intersection of the incident and reflected polars. The deflection angles given by this intersection determine the angles of the sliplines, s_1 and s_2 in Figure 2.1(b), before they interact with the expansion fans. In theory, an MI is physically possible at higher M_0 values, due to the reflected polars also intersecting the incident one, as seen in Figure 2.1.2(a). Despite this, the final MI would be unstable. This

is because the resulting sliplines would have a deflection with an opposite sign. This would result in a divergent duct, leading to a deceleration of the flow and resulting in an unstable system as described in Section 2.1.1.

If M_0 is further decreased, the polar shown in Figure 2.1.2(c) is eventually reached at $M_0 = 2.95$. In this case, both RI and MI configurations are still possible but they no longer lie on the same point. As before, the RI is given at the intersection of the two reflected polars and the MI at the intersections of the reflected and incident polars. Configurations of this type are referred to as dual solutions, where both stable RI and MI configurations are possible. The configuration in Figure 2.1.2(d) is reached when M_0 is decreased to $M_0 = 2.83$. This point is known as the Detachment condition. As it can be seen, the RI configuration is given at the tangent point of the two reflected polars. This point is the minimum M_0 at which a RI is physically possible. This is due to the fact that lower M_0 polars will further separate the two reflected polars reaching a configuration such as the one in Figure 2.1.2(e), where there is no intersection between the reflected polars. At this point, only a MI is physically possible.

2.1.3 Regular, Mach and Dual Solution Domains

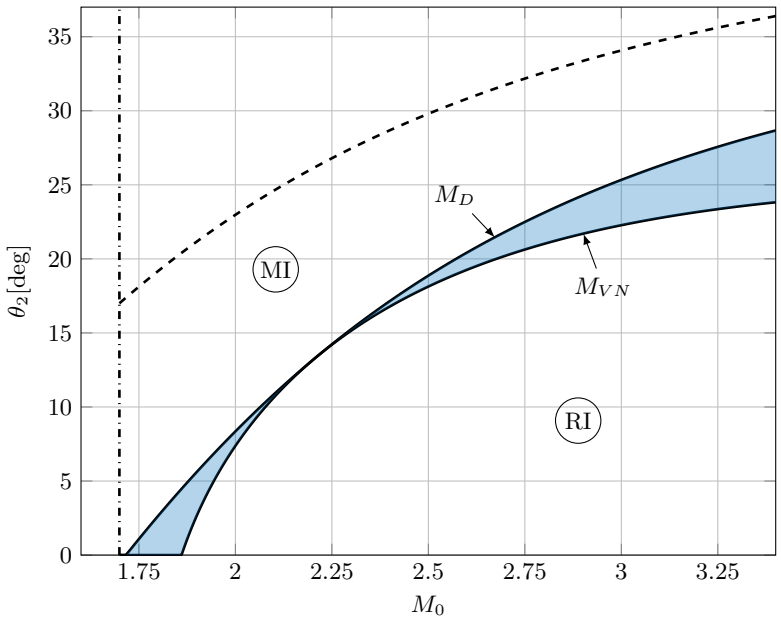

Figure 2.4: $M_0 - \theta_2$ plane for $\theta_1 = 17°$ showing the dual solution domain through the shaded area. The θ_2 and θ_1 attached shock boundaries are shown through the dashed and dash-dotted lines, respectively. M_{VN} represents the von Neumann curve and M_D the Detachment one.

As mentioned, stability boundaries between RI and MI are defined by the von Neumann and Detachment conditions (M_{VN} and M_D). M_{VN} and M_D take different values depending on the θ_1, θ_2 combination considered. M_{VN} can be computed by finding the M_0 value at which the reflected and incident polars intersect at a single point. On the other hand, M_D can be calculated by finding the M_0 value at which both reflected polar curves become tangent. If these two values are computed for multiple conditions where θ_1 is fixed, the von Neumann and

Detachment curves are obtained. These curves can be represented through a $M_0 - \theta_2$ plane, such as the one in Figure 2.4. Two additional lines can be seen here: the attached θ_1 and θ_2 lines. These lines represent the boundaries beyond which the wedges are no longer capable of producing an attached shock, which would lead to a bow shock configuration ahead of the wedges. Three domains can be distinguished on any $M_0 - \theta_2$ plane: RI, MI and dual solution. These domains can be used to predict the resulting shock configuration by identifying in which area the current configuration lies.

The RI domain can be found under high M_0 and low θ_2 conditions. In these regions, polars such as those in Figure 2.1.2(a) can be expected. Under steady conditions, RI configurations always prevail here. The MI domain exists for low M_0 and/or high θ_2 conditions. Here, polars similar to Figure 2.1.2(e) can be found. In this region the only physically possible solution is the MI configuration. The region which appears where $M_{VN} > M_0 > M_D$ is satisfied is known as the dual solution domain. In this region, both MI and RI configurations are theoretically possible.

Even though shock polar theory is a very useful tool to estimate the shock configuration that will prevail under a set of given conditions, mismatches between theory and experiments have been observed. This is especially common in the dual solution domain. This issue has acted as the starting point of many research studies, some of which are discussed in Section 2.2.

2.2 State of the Art

The analytical tools presented in Section 2.1 are very useful when analyzing the shock-shock interaction phenomenon. At the same time, due to the complexity of this physical phenomenon some unknowns remain that these simplified models cannot address. For this reason, and despite the significant progress achieved on the topic over the last half century, shock-shock interactions still remain up to today as a topic of interest in the field of Gas Dynamics. The current section aims to give the reader an overview of the completed research in this area and place the current project in its appropriate context. At the same time, this summary of the available literature is used to identify relevant gaps in the knowledge that are used to formulate the Research Question of the current project, presented in Section 2.3.

2.2.1 Transition and Hysteresis

As it was already mentioned in Section 2.1.3 the MI to RI and RI to MI transition points are still an active research topic in Gas Dynamics. In early studies, it was believed that the transition point in both directions was always the von Neumann condition. One of the earliest papers on the topic is Henderson and Lozzi (1975) where one of the first campaigns aimed at observing the transition process is presented. It is hypothesized that the transition point is the von Neumann condition, based on the assumption that transition would have to occur in a smooth way, without pressure jumps, which is only possible at the mechanical equilibrium point. The appearance or disappearance of a slipline was used as the transition criterion due

to the symmetric wedge configuration studied. It was found that almost all of the transitions occurred near the von Neumann condition which reinforced the initial hypothesis.

The first publication to suggest the existence of a hysteresis phenomenon is Hornung et al. (1979). Here, it is hypothesized that, in steady flows, transition always happens near the von Neumann condition. A series of experiments were performed where the incidence angle of a pair of symmetric wedges was varied, with the aim of looking for transition. As in previous studies, it was indeed found that transition always happened at the von Neumann condition, but in this case a length scale seemed to also be involved in the problem which made the MI more stable than the RI in the dual solution domain. It is suggested that the transition point is not exactly at the von Neumann condition but at a point such that a line of information between the length scale of the problem and the interaction point is opened, usually through the subsonic pocket that appears after a Mach stem. It is argued that this phenomenon makes the MI a lot more stable than the RI so in every point where it is possible (von Neumann condition and above) a MI appears. It is predicted that an hysteresis phenomenon could be theoretically possible but, due to the stability issue, the MI configuration tends to dominate within the dual domain. In another study, Hornung and Robinson (1982a), an attempt was also made to find the hysteresis phenomenon by using a double wedge symmetric configuration in which the incidence angle was gradually changed. It was not found and all transition points were recorded at the von Neumann condition. The stability hypothesis of Hornung et al. (1979) is used to theorize that the reason for this could be that the perturbations in the experiment were large enough to destabilize the RI and trigger the MI as soon as it becomes possible at the von Neumann condition.

The confirmation of the existence of the elusive hysteresis phenomenon arrived in 1995 through the publications of Ivanov et al. (1995) and Chpoun et al. (1995). In Ivanov et al. (1995) a numerical investigation of the transition phenomena is performed by simulating a symmetric wedge configuration. The incidence angle was gradually changed in both directions and the transition point was recorded. The results supported the conclusion that an hysteresis effect exists in the transition from RI to MI and vice versa. It was found that if the initial deflection angle is below the von Neumann condition and it is gradually increased, transition from RI to MI tends to occur near the Detachment condition. On the other hand, if the angle is initially above the Detachment condition and it is slowly decreased, transition from MI to RI can be detected at the von Neumann point. The simulation was run in an ideal environment which led to the hypothesis that the premature transitions recorded in previous studies could be caused by wind tunnel noise and other perturbations. The Chpoun et al. (1995) study is an experimental one. A two wedge symmetrical configuration was used where the incidence angle was changed both discretely and continuously through a rotation device that kept the wedge inlet area constant. The results experimentally proved the existence of the hysteresis loop. It was found that transition in the MI to RI direction always happened at the von Neumann condition, like in all the previous experiments. On the other hand, it was observed that RI to MI transition could happen anywhere within the dual solution domain. It is argued that the apparent randomness in this last transition type could be due to experimental issues. Finally, they also observed a slight variation of the RI to MI transition angle with the h/w geometrical parameter, where w is the wedge's hypotenuse length and h the inlet height.

One of the most important papers on the topic is Ivanov et al. (2003b), where the hysteresis

loop is finally characterized and confirmed through experiments. The two main goals of the study were to experimentally validate the numerical results of Ivanov et al. (1995) and to study the effect of wind tunnel perturbations on the transition points. To do this, an experimental campaign was performed in a low noise wind tunnel specially conditioned to eliminate noise and other perturbations from the test section. The setup was done with a pair of symmetric wedges that could vary their incidence angle. The main results are shown in Figure 2.5, where RI configurations can be seen where the Mach stem length becomes zero and MI where it is nonzero. The hysteresis loop is clearly visible with MI to RI transition always happening in the vicinity of the von Neumann point and RI to MI near the Detachment point. It can also be seen how the match is not perfect, specially in the RI to MI transition with most of them happening about 1 degree below the detachment point, probably due to some residual perturbations. Despite this, the results are strong enough to suggest that, under ideal conditions, the RI to MI transition point is the Detachment point. This study was later expanded in Ivanov et al. (2003a), where the results of Ivanov et al. (2003b) were compared to those obtained in various wind tunnels of different types. The final results reinforce the theory that wind tunnel perturbations can trigger premature transition from RI to MI.

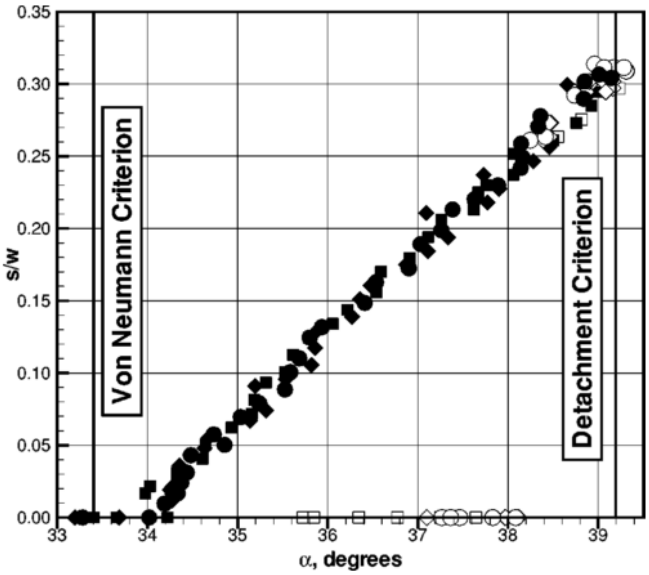

Figure 2.5: Low noise wind tunnel results presented in Ivanov et al. (2003b) showing the Mach stem growth with the deflection angle. Closed symbols represent decreasing angle experiments and open symbols increasing ones. Each shape represents a separate wind tunnel run.

One of the most recent contributions to the field is Mouton (2007). The main findings in this project are a Mach stem growth model and a set of experimental campaigns focused on the hysteresis phenomenon. The hysteresis experiments focused on recording transition for varying deflection angles with the main innovation being that an asymmetric shock configuration was used instead of the more conventional symmetric type. Most RI to MI transitions were detected about half way through the dual solution domain, which confirms the unstable nature of the RI within this domain and that the von Neumann condition is not the RI to MI transition point in ideal conditions.

2.2.2 Mach Number Induced Transition

Until now, all the presented studies focused on inducing transition by maintaining M_0 constant and changing the wedge deflection angles. As discussed in section 2.1.3, the shock configuration is determined not only by these angles but also by the inflow Mach number. This means that, theoretically, transition should also be achievable by keeping the deflection angles constant and changing the inflow Mach number. By looking at Figure 2.4 it is also visible that a dual solution domain exists when changing M_0 so it would also be reasonable to assume that a hysteresis phenomenon could be induced by a M_0 change. This assumption opens up another research branch within the field which can focus on exploring the influence of the change in M_0 on the shock system. As of today, the available research on this topic is quite scarce. The main reason commonly attributed to it is that experiments of this type require a variable inflow Mach number, something that requires fairly complex and uncommon wind tunnels.

The first paper published on the topic is Ivanov et al. (2001a). Here, it is hypothesized that a dual solution domain could exist in the $M_0 - \theta_2$ space in the same way as it exists in the $\theta_1 - \theta_2$ one. To prove it, a numerical simulation is run on a symmetric shock configuration with varying inflow Mach number. RI to MI transition was detected at the Detachment condition and MI to RI at the von Neumann condition. There is a small disagreement with the MI to RI transition but it is attributed to the small Mach stem length which introduces some uncertainty at this point. The results of this study point to not only the existence of a hysteresis loop for changing Mach number but that it also seems to match very closely the theoretical values.

The first and only experimental study done in this area is Durand et al. (2003). Here, the effect of changing the inflow Mach number for both symmetric and asymmetric wedge configurations is studied. This is done with the goal of finding and characterizing the hysteresis loop. To achieve the variable M_0, a wind tunnel with an adjustable nozzle that could be modified during runs was used. For the symmetric cases, no hysteresis was observed, with transitions happening half way through the dual solution domain in the cases where the RI domain existed. An additional case was tested where only MI and dual solution domains existed. No transition from MI to RI was detected. The results for the asymmetric configuration are presented in Figure 2.6. It can be seen how both transition points are located about half way through the dual domain. The difference between the two points is considered too small to assume the existence of an hysteresis loop. The absence of the hysteresis phenomenon is attributed to the presence of noise and perturbations in the tunnel.

2.2.3 Reflection Stability

As mentioned through this chapter, flow perturbations and noise seem to play an important role on transition within the dual solution domain and they appear to be a dominant factor when analyzing hysteresis. This has sparked a debate over the years about the stability of RI and MI solutions within the dual solution domain and the type of perturbations that can

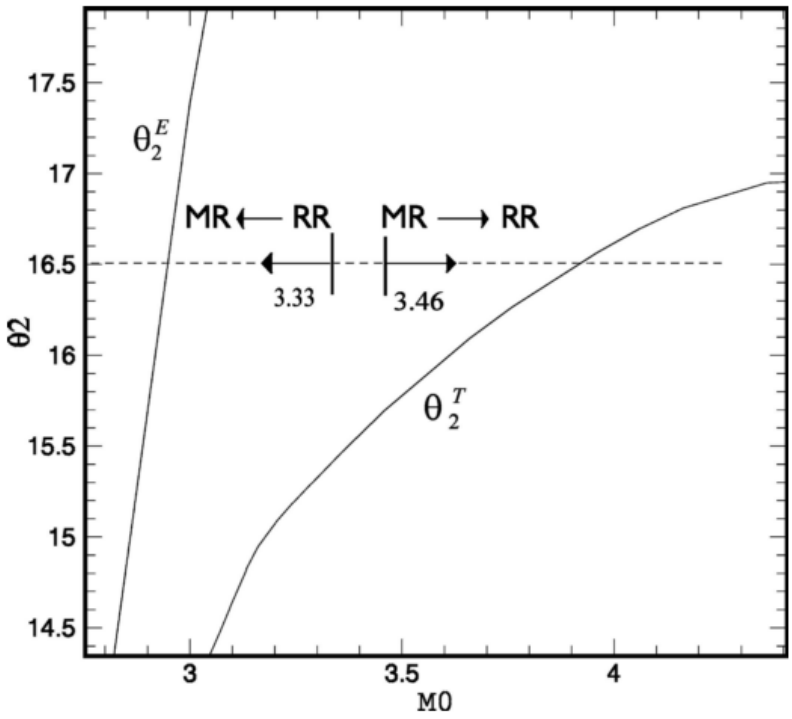

Figure 2.6: Asymmetric configuration results presented in Durand et al. (2003) for $\theta_1 = 25°$, $\theta_2 = 16.5°$. Where θ_2^T is the von Neumann line and θ_2^E the detachment one.

trigger transition from one to the other. This section will focus on giving an overview of this topic and the most relevant research done in this area.

A theoretical approach to the problem was done in Hornung (1996) where the stability of MI versus RI was studied from an analytical point of view. A typical symmetric shock polar of a configuration within the dual solution domain can be seen in Figure 2.7. It is argued that, in the dual solution domain, a change from MI to RI (B to A in Figure 2.7) would require an increase in pressure which would, in turn, result in an increase of the Mach stem size leading to an unstable situation. On the other hand, a transition from RI to MI (A to B in Figure 2.7) would require a perturbation that would result in a pressure decrease. If this perturbation is large enough to reach point B, it would generate a Mach stem, resulting in a stable configuration. This reasoning leads to the conclusion that the MI is the stable solution within the dual solution domain. This derivation is also consistent with the principle of maximum entropy, if the assumed perturbations are small enough.

Another interesting experiment to study the influence of perturbations on transition was done in Sudani et al. (2002). To test the influence of perturbations on transition, a series of experiments were performed where water vapor was injected in the test section in order to generate an artificial and controlled perturbations in the flow. In one of these tests, an asymmetric wedge deflection configuration was placed slightly above the von Neumann condition. In previous experiments without the water vapor it was found that the RI was stable enough and no transition to MI was recorded for this configuration. Once the water was

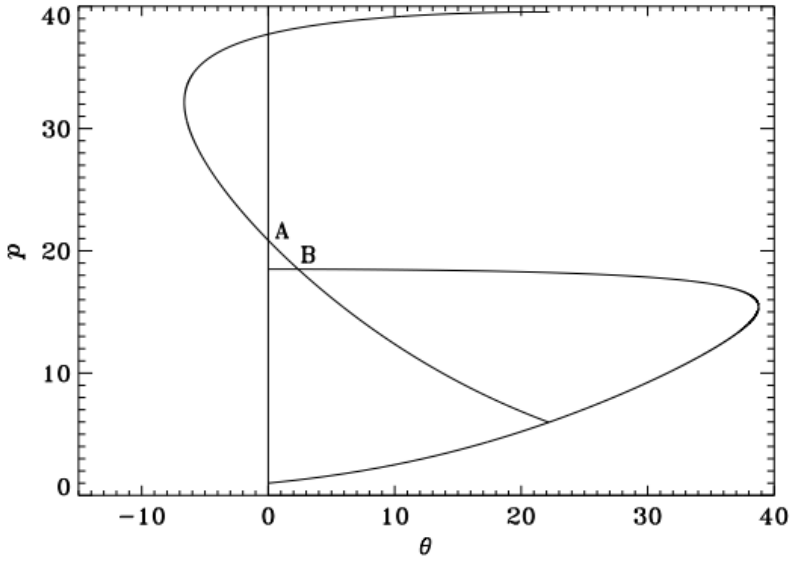

Figure 2.7: Shock polar of a symmetric reflection within the dual solution domain (Hornung, 1996).

injected, the reflection transitioned from RI to MI as soon as the vapor reached the test section. It was found that this transition happened for even very low water vapor concentrations where the disturbance generated was almost negligible. In a second type of tests, water was injected while in the RI or MI domain and the deflection angle was changed in order to reach and surpass the dual solution domain. It was found that transition in both directions always happened at the von Neumann condition and no hysteresis phenomenon was recorded. The physical mechanism of the water vapor induced transition was still not fully understood but it is hypothesized that a hysteresis loop may not be possible within a perturbed flow.

In Ivanov et al. (2003b) a series of experiments were performed in a specialized low noise wind tunnel where flow perturbations were reduced to a minimum. This was the first study in which the transition phenomenon was studied experimentally in an almost perfectly uniform flow. As mentioned in section 2.2.1, this was also the first study to find solid experimental evidence of the hysteresis loop and reached the conclusion that, in absence of perturbations, the RI to MI transition point is the Detachment condition. These results emphasize once more the importance of perturbations in transition. In a similar way that in Sudani et al. (2002) it was shown that flow perturbations can completely suppress the hysteresis loop, in Ivanov et al. (2003b) it was proven that the absence of them can widen the loop all the way to the theoretical limits of the dual solution domain. It can be again inferred from these results that the RI tends to be an unstable solution within the dual solution domain.

At this point, it is certain that flow perturbations play an essential role in shock interaction transition and they seem to be directly related to the stability of the RI within the dual solution domain. This line of study was further expanded in Sudani et al. (2003) where a series of experiments, very similar to those in Ivanov et al. (2003b), were performed in a regular wind tunnel, where flow perturbations were expected. Two experimental campaigns

were conducted, yielding the results presented in Figure 2.8. As it can be seen, the repeatability of the the experiments was very low, with the transition points varying significantly between runs. It is suggested that transition is dominated by flow perturbations, which would explain the highly irregular transition points. These perturbations are divided into uniform perturbations, such as pressure and freestream fluctuations, and irregular perturbations, like dust particles or water vapor, for example. In an attempt to characterize these irregularities, a series of pressure measurements were done in the settling chamber and the test section with the aim of correlating uniform pressure fluctuations with the changes in the transition point. The results obtained showed no clear correlation between these pressure fluctuations and the transition point, so it was concluded that the transition point has to be dominated by irregular perturbations while uniform ones play a minor role. With these results it is hypothesized that the level of uniform perturbations in the flow determine the maximum theoretical angle where an RI can be observed in the dual solution domain. At the same time, if irregular perturbations exist, it seems like transition can be triggered at any point between the von Neumann condition and this maximum angle. It is also suggested that the RI becomes more unstable as the deflection angle increases, requiring lower perturbations to trigger transition but no definitive proof of this is provided due to fact that the perturbations were not controlled.

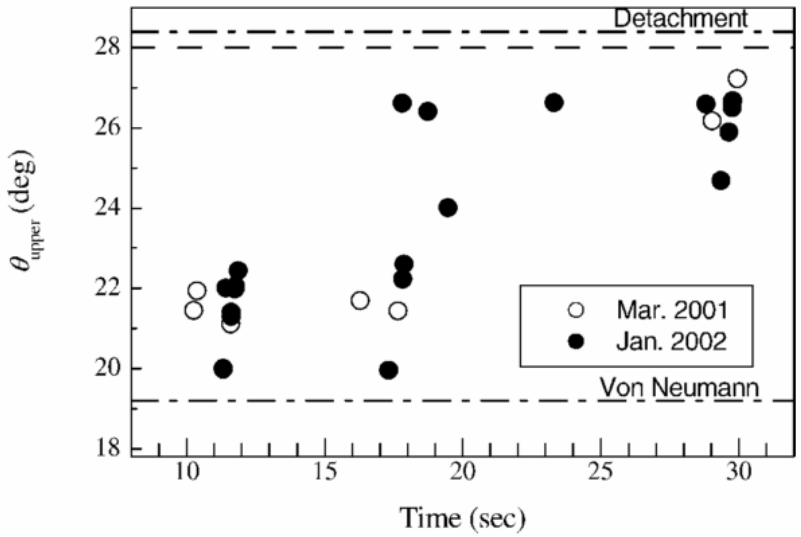

Figure 2.8: Transition points recorded in Sudani et al. (2003) for varying top wedge deflection angles in two different experimental runs.

2.2.4 Three-dimensional Effects

All of the discussion up until now has been done assuming a two dimensional flow. In reality, this will not always be the case with three-dimensional effects usually influencing the flow system. This is of great relevance in experimental studies, where 3D effects can contaminate the measurements and the results will no longer correlate with 2D theory. For this reason, multiple studies have been done to analyze these effects, some of the most important ones

being Skews (1997), Ivanov et al. (2001b), Sudani et al. (1999) and Sudani et al. (2002).

Skews (1997) focuses on the design of the wedges and inlet and how it can affect the 3D behavior of the system. An analytic approach is used to predict the requirements in order to avoid 3D effects in symmetric RI configurations. This is done through corner signal analysis. The signal that indicates that the wedges have a finite span propagates through the flow along two Mach cones, one for each wedge tip. The flow contained within these cones will no longer be two dimensional as it will be already influenced by the tip of the wedges. In a RI configuration, this will lead to two important points W and T, both of them shown in Figure 2.9. W represents the point where the corner signal reaches the center of the wedge, so the flow cannot be considered 2D beyond it. T is defined as the point where the two corner signals meet, beyond which the shock will always be curved.

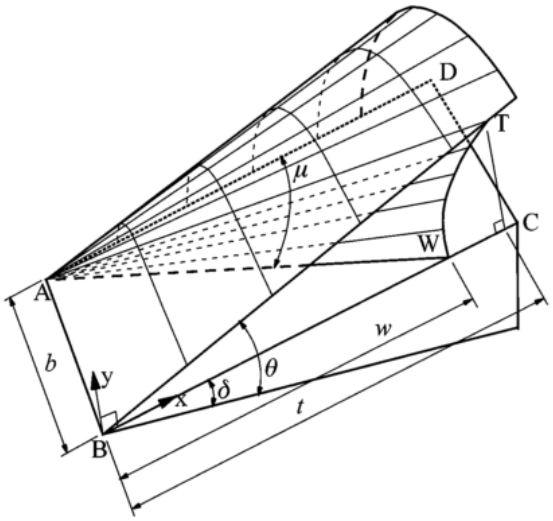

Figure 2.9: Schematic representation of a Mach cone corner signal over a finite wedge (Skews, 1997).

Both of the previous points can be obtained in non-dimensional form as (Skews, 1997):

$$w/b = \frac{1}{\tan \mu} \tag{2.6}$$

$$t/b = \frac{1}{\sqrt{\tan \mu^2 - \tan \mu^2(\theta - \delta)}} \tag{2.7}$$

Where t and w are the distances from the leading edge to T and W, respectively, b is the wedge's half span, θ the shock angle and δ the wedge angle. μ represents the Mach angle, which can be computed as:

$$\sin \mu = \frac{1}{M_0} \tag{2.8}$$

To ensure a 2D flow in the center plane of the system, the Mach cones must intersect it downstream of the reflection point. For a symmetric configuration, the reflection will always occur where the shock reaches half the vertical distance between wedges. Defining the position of this point along the wedge as s, it can be seen that it must always be smaller than t to avoid 3D effects at the reflection point. In order to avoid this, the theoretical minimum inlet aspect ratio must be (Skews (1997)):

$$(b/h)_{\min} = \frac{b}{t}\frac{\cos\theta - \delta}{\sin\theta} \tag{2.9}$$

Where h is half the vertical distance between the wedge leading edges. The conditions to avoid 3D effects in a certain region of the flow around an RI can now be computed by using Equations 2.6, 2.7 and 2.9. Although very useful for preliminary designs, they are fairly limited due to the fact that they are computed for symmetric RI configurations. Obtaining similar relations for a MI case is not possible due to the uncertainty of the Mach stem's shape and size. A series of experiments were conducted in Skews (1997) in order to validate this model. It was found that it is recommendable to use larger aspect ratios than the ones predicted by Equation 2.9. It is also concluded that the minimum inlet aspect ratio of 1.25 and wedge aspect ratio of 2.5 guidelines previously suggested in Fomin et al. (1996) seem to be sufficiently valid.

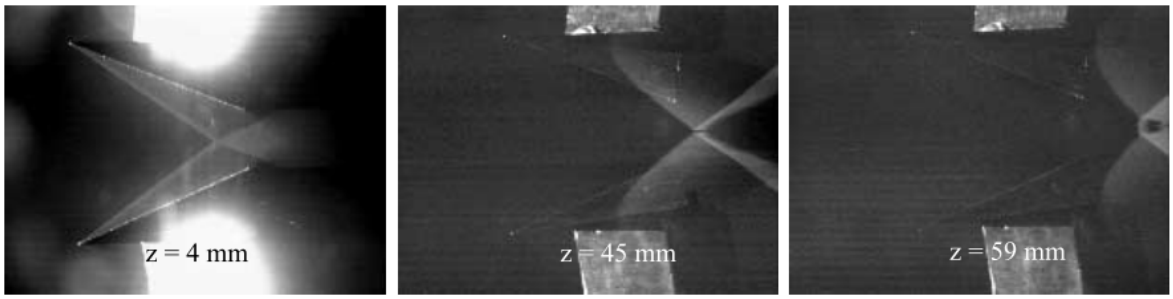

Figure 2.10: Laser sheet visualization of a symmetric shock-shock interaction obtained in Ivanov et al. (2001b) at different spanwise locations where $z = 0\,\mathrm{mm}$ corresponds to the center plane.

In Ivanov et al. (2001b), a series of experimental campaigns were performed where a laser sheet technique was used in the freestream direction to visualize the shock pattern at different spanwise sections along the wedge system. This was done for a series of wedge angles and inlet aspect ratios. The results proved that the shock reflection was nonuniform in the spanwise direction no matter the inlet aspect ratio. This can lead to different phenomena such as a MI with a varying Mach stem height along the spanwise direction or a coexistence of both RI and MI at different spanwise locations. An example of this is shown in Figure 2.10, where an RI exists in the center plane, where the flow is mostly 2D, but an MI can be seen towards the edges, where the flow becomes strongly three-dimensional. A similar experiment was performed in Sudani et al. (2002) where instead of placing the laser sheet in the freestream direction, it was placed in a spanwise way, perpendicular to the incoming flow. This allowed to see the whole interaction structure at a given streamwise location. Similar configurations

as the ones in Ivanov et al. (2001b) were found. It is hypothesized that they are caused by the 3D influence of the edges and they appear slightly downstream from the interaction point. This study confirmed the non-uniformity of the shock interactions in three-dimensional setups.

2.3 Research Question

Based on the literature survey summarized in Section 2.2, gaps in the current shock-shock interaction knowledge can be identified. The objective of this project is to cover some of these gaps by answering the Research Question formulated in this section.

Research Question: *In asymmetric shock-shock interactions, how does a variable inflow Mach number affect the transition process between Regular and Mach Interactions when the wedge deflection angles are kept constant?*

A lot of previous studies have focused on shock-shock interactions with a fixed M_0 and variable deflection angles. On the other hand, the only experimental investigation with a variable Mach number is Durand et al. (2003). Due to this, the Mach number induced transition process is still not well understood and some of its most important parameters, such as its transition points and a possible hysteresis loop, have still to be accurately defined. This main question is now broken down into a series of subquestions.

- **Subquestion 1:** *Is there any correlation between the transition points predicted by inviscid Gas Dynamics analytical theory and the experimental observations of a shock-shock interaction with a variable inflow Mach number?*

  As presented in Section 2.2.1, a lot of previous studies have proven that shock polar theory can accurately predict the transition between RI and MI for cases with variable deflection angles. At the same time, a hysteresis loop has been shown to exist under low noise conditions. It is still to be proven if this is also the case for experimental shock-shock interactions with a variable inflow Mach number.

- **Subquestion 2:** *What effects do flow non-uniformities have on the transition process between RI and MI in a shock system with a variable inflow Mach number?*

  As shown in Section 2.2.3, multiple studies have shown how flow perturbations can trigger a premature transition from RI to MI, although the physical mechanism behind this is still not well understood. At the same time, it is still not clear what type of perturbations are the ones responsible for this phenomenon. Experiments with a variable inflow Mach number could provide further insight into this problem.

- **Subquestion 3:** *Can the evolution of the Mach stem with the inflow Mach number be systematically measured with a Schlieren visualization system?*

  Despite the extensive theory presented in Section 2.1, there is still no analytical model that can predict the evolution of the Mach stem size with the inflow Mach number. Due

to this, any experimental data on the topic can be useful to solve this problem. One of the objectives of this project is to generate this type of experimental observations by systematically analyzing the Schlieren visualization images of variable inflow Mach number experiments.

- **Subquestion 4:** *Can the use of a Focusing Schlieren setup provide any further insights on the topology of a shock-shock interaction or the influence of three-dimensional effects on it?*

  No experiments were found in the literature where a Focusing Schlieren system was used to study a shock-shock interaction. The advantage of this type of visualization setup is that it has a finite depth of focus. This feature can be used in combination with Schlieren visualization to get a better understanding of the three-dimensional topology of a shock system.

Chapter 3

Experimental Design and Setup

The main elements of the experimental setup used in the current project are the experimental parameter space and the wind tunnel model. The present chapter is dedicated to giving an overview of the design process followed to obtain them and present the final setup used for the experimental campaign. The chapter begins in Section 3.1 by presenting the experimental facilities in which the current study takes place. After this, the design process and the final experimental parameter space are explained in Section 3.2. This is followed by an overview of the wind tunnel model used and the design process followed in order to obtain it in Section 3.3. The chapter is concluded in Section 3.4 by explaining the experimental procedure followed during all tests and presenting the Test Matrix.

3.1 Experimental Facilities

The experiments were carried out in the transonic-supersonic TST-27 wind tunnel, shown in Figure 3.1, located at the High Speed Laboratory of the TU Delft Aerospace Engineering Faculty. This is a blowdown type facility fed by an external vessel which is capable of holding air at pressures between 25 and 40 bar. It has a rectangular test section of 270×280mm where the model can be placed by either fixing it to the side walls or through a sting attached to a support located further downstream. For supersonic regimes, the tunnel uses a flexible convergent-divergent nozzle that can change the area ratio between the test section and the tunnel's throat, allowing this way Mach number variations during a run. The facility can generate Mach number ranges of 0.5 to 0.85 and 1.15 to 4.2 in the transonic and supersonic regimes, respectively. The total pressure (p_t) is controlled through a valve that regulates the pressure in the settling chamber. Possible total pressures that can be used during startup are shown in Figure 3.2. The upper p_t bound is determined by the maximum mass flow of $50\,\mathrm{kg} \cdot \mathrm{s}^{-1}$ that the system can supply. The minimum p_t, in turn, is limited by the maximum expansion the flow can experience without condensation effects at the test section. Given these limits, the total pressures used during the experiments ranged from 4 to 6 bar, de-

pending on the specific start-up requirements for each configuration. The selection of these startup conditions are further discussed in Section 3.3. The total temperature in the tunnel is determined by the temperature of the external vessel, kept at external ambient temperature. For the current experiments, this was approximately 280 K.

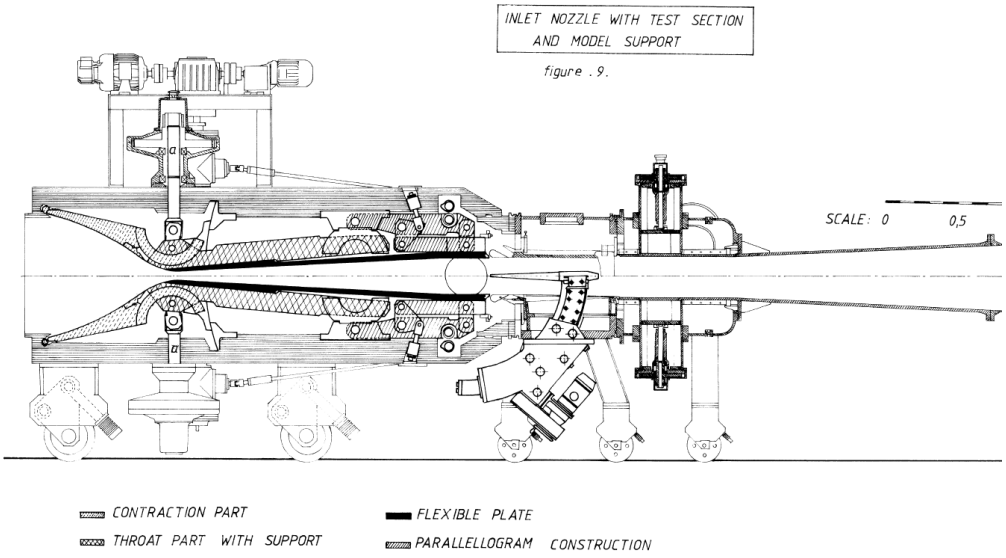

Figure 3.1: Drawing of the TST-27 Transonic-Supersonic Wind Tunnel.

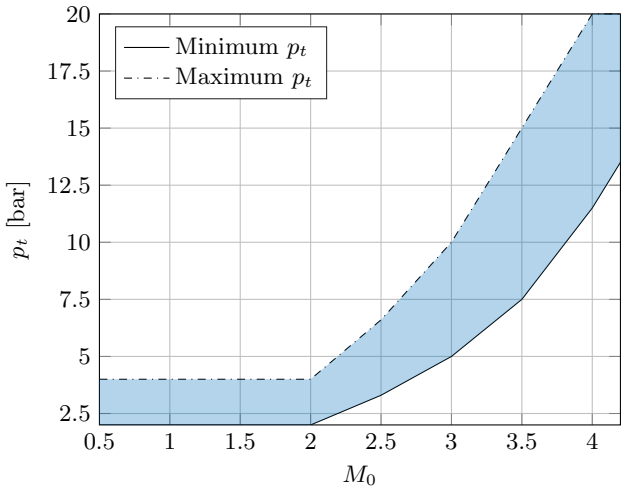

Figure 3.2: Total pressure limits of the TST-27. The shaded area represents the possible $M_0 - p_t$ combinations that can be used in an experimental run.

3.2 Experimental Parameter Space

Before designing the wind tunnel model, the experimental parameter space must be determined. As it was previously explained in Section 2.1.2, the shock-shock interaction system is

defined by four sets of parameters: the flow properties, through γ, the inflow Mach number (M_0) and the wedge deflection angles (θ_1 and θ_2). Given the experimental conditions, the flow properties do not change in a significant way, so γ can be considered constant at $\gamma = 1.4$. This leaves three variables that can be modified according to the experimental requirements: θ_1, θ_2 and M_0. The design process used to select them and the final values chosen are presented in Sections 3.2.1 and 3.2.2, respectively.

3.2.1 θ_1 Selection

The selection of θ_1 determines the shape of the von Neumann and Detachment curves on the $M_0 - \theta_2$ plane and the size of the dual solution domain. Two extreme cases for a very low and very high θ_1 are shown in Figure 3.3. As it can be seen, selecting two different θ_1 can lead to two completely different Detachment and von Neumann curves. Due to this, and in order to get a better understanding of how these curves affect the transition points, only one θ_1 value is selected for the current experiments, fixing the $M_0 - \theta_2$ plane.

As it can be seen in Figure 3.3, increasing θ_1 has different effects on the $M_0 - \theta_2$ plane. The first is a rightwards shift of the attached θ_1 boundary. This is due to the fact that an increase of the deflection angle requires higher Mach numbers in order to produce and attached shock. The second noticeable effect is that an increase in θ_1 causes a larger separation between the

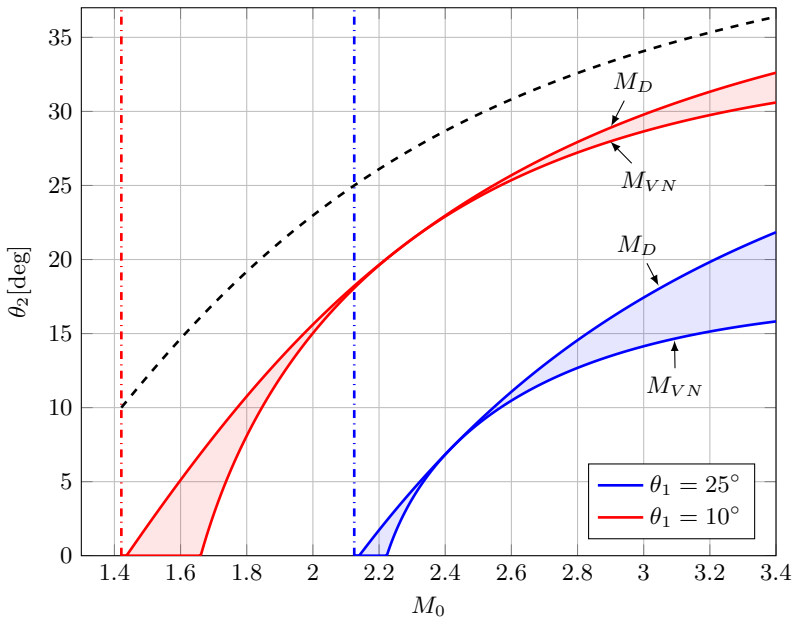

Figure 3.3: $M_0 - \theta_2$ plane for $\theta_1 = 10°$ and $\theta_1 = 25°$ showing the dual solution domain in the shaded areas. The θ_2 and θ_1 attached shock boundaries are shown through the dashed and dash-dotted lines, respectively. The attached θ_2 curve is shown in black due to it being the same for both configurations. M_{VN} and M_D represent the von Neumann and Detachment curves, respectively. For both θ_1 configurations, the RI domain is located below the von Neumann curve and the MI domain above the Detachment line.

von Neumann and Detachment curves, which results in a wider dual solution domain. At the same time, a higher θ_1 decreases the slopes of the von Neumann and Detachment curves, which in turn, requires lower θ_2 values to reach the dual domain. Another effect that cannot be seen in Figure 3.3 is that larger θ_1 angles result in larger area ratios between the inlet and the throat of the wedges. This is relevant for the startup problem of the model, which is discussed in Section 3.3.

These effects caused by a larger θ_1 can be translated into a series of advantages and disadvantages regarding the experimental design. The main advantage is that a larger dual solution domain allows a better study of the shock-shock system in this domain. This is due to the fact that a larger separation between the von Neumann and Detachment curves allows a more precise determination of the transition points within the dual solution domain. One of the disadvantages is a larger minimum M_0 required for an attached shock. At the same time, it results in a more difficult startup of the system due to the increase in area ratio generated by the large deflection angle. These trade offs show that the selection of θ_1 is not straightforward. In order to make this decision, a balance between the capabilities of the facilities used and the desired experimental space has to be made. To reach a final decision, a series of design requirements are formulated in order to address these conflicting requirements:

- The dual solution domain must be big enough to generate a clear distinction between the von Neumann and Detachment lines. In order to precisely study the transition and posible hysteresis in this region, the horizontal separation between these two lines on the $M_0 - \theta_2$ must be of at least $\Delta M_0 = 0.1$.
- The minimum M_0 must be low enough to be able to generate an attached shock system given the wind tunnel's capabilities. The possible M_0 ranges are limited by the maximum p_t that can be safely used in the TST-27. This value is established at $p_t = 6\,\text{bar}$. By looking at Figure 3.2, it can be seen that the maximum M_0 achievable under this restriction is approximately 3.30.
- The area ratio between the inlet and throat of the wedge system must be low enough to allow a startup of the system. This requirement is coupled with the design of the wind tunnel model, which is explained in more detail in Section 3.3.

After several iterations, the final value selected is $\theta_1 = 17°$. Its $M_0 - \theta_2$ plane is shown in Figure 3.4. This value satisfies the previously presented design requirements while complying with the capabilities of the wind tunnel used.

3.2.2 θ_2 and M_0 Ranges Selection

Once the $M_0 - \theta_2$ plane has been defined through the θ_1 selection, the remaining parameters to fully determine the experimental space are θ_2 and M_0. As explained in Section 2.3, the main goal of the current project is to study the effect of a variable M_0 on the shock system. To do this, discrete values of θ_2 are chosen while M_0 is allowed to vary.

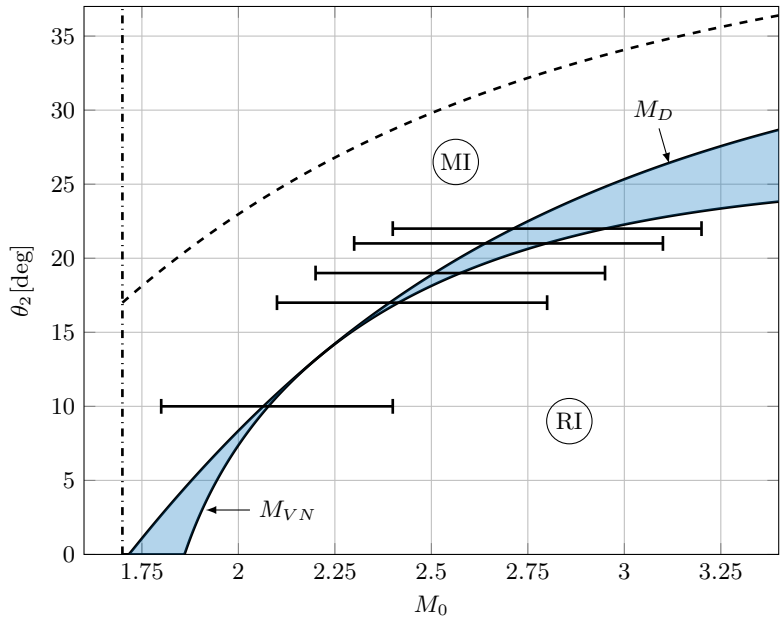

Figure 3.4: $M_0 - \theta_2$ plane for $\theta_1 = 17°$ showing the dual solution domain in the shaded area. The θ_2 and θ_1 attached shock boundaries are shown through the dashed and dash-dotted lines, respectively. M_{VN} represents the von Neumann curve and M_D the Detachment one. The M_0 ranges used in the experiments are represented through the black horizontal segments.

Five different θ_2 cases are investigated. This allows to study a big portion of the $M_0 - \theta_2$ plane while keeping the total number of required geometries within a manageable amount. The five selected values are $\theta_2 = 10°$, $17°$, $19°$, $21°$ and $22°$. These geometries, together with their corresponding M_0 ranges are shown in Figure 3.4. As it can be seen, the four highest θ_2 geometries are placed in a region with a large dual solution domain. This condition enables a clear distinction between the von Neumann and Detachment lines which aids with the determination of the transition points within the dual solution domain. The remaining geometry, $\theta_2 = 10°$, was placed where the dual domain is so small it can be considered negligible. Here the transition point can be considered unique due to the absence of any dual solution domain. This feature can be used to verify the custom data processing method developed for this project.

The possible M_0 ranges are bounded by the capabilities of the wind tunnel. During the experiments p_t is kept constant in order to reduce the complexity of the experimental procedure and limit the number of independent variables. As shown in Section 3.1, if p_t is kept constant, the possible M_0 values that the tunnel can generate have an upper and lower limit. This is illustrated through Figure 3.2 where it can be seen that every p_t value above 4 bar has a maximum and minimum M_0 attached to it. In order to maximize the M_0 range for a given run, every test is started at the maximum M_0 for the set p_t and then lowered to its minimum possible M_0. As explained in Section 3.3.2, one of the design challenges of the wind tunnel model is to solve the startup problem. It is also shown that larger startup M_0 values facilitate this startup process. The main disadvantage of choosing a high M_{Max} is that it will result in an also high M_{Min} which limits how far the system can penetrate the MI domain. This is detrimental for the Mach Stem Height (MSH) study, as it limits the maximum size the Mach

stem can reach. Thus, a compromise must be reached in order to achieve a high enough M_0 to allow a startup of the system but not too high in order to allow a MSH study. This is solved by computing the minimum M_0 needed for the startup of the model and setting it as M_{Max}. This value can be computed by using the theory presented in Section 3.3.2. The p_t needed to start the tunnel at $M_0 = M_{\text{Max}}$ is then computed by finding the corresponding p_t for this M_0 on the maximum p_t curve in Figure 3.2. The final selected M_0 ranges can be seen in Figure 3.4.

3.3 Wind Tunnel Model

Now that the desired experimental cases are established, an aerodynamic model capable of generating them in the wind tunnel has to be designed and manufactured. The general setup of the model is shown in Figure 3.5. It consists of two wedges placed opposite to each other, one facing upwards and the other downwards. This way, they can asymmetricaly deflect the freestream flow generating the desired interacting shock waves. Both wedges are rigidly connected to the side walls of the test section through two horizontal supports. The main geometrical parameters that define the model are shown in Figure 3.5(b). The top wedge imposes a flow deflection with an angle equal to θ_1. The second incident shock is generated by the bottom wedge through a flow deflection equal to θ_2. This way θ_1 and θ_2 can be selected by changing the angle of the wedges. This is done by manufacturing a separate wedge for each θ_1-θ_2 configuration. The required values for θ_1 and θ_2 are already defined through the experimental parameter space. θ_1 is unique, so only one top wedge is needed. On the other hand, five different θ_2 configurations are selected, so five different bottom wedges have to be designed. The other main parameter that needs to be defined is $2g/w$. This parameter defines the shape of the shock-expansion fan pattern. In order to control the total number of variables in the system, this parameter is kept constant for all configurations. $2g/w$ is crucial for the design of both the shock-shock interaction system and the wind tunnel model so special care has to be taken to define it. This is done by following three design aspects:

- **3D effects:** The system must be capable of generating a 2D flow in the center section of the system. For this reason, any three dimensional effects induced by the wedges or the tunnel must be minimized.
- **Tunnel startup:** The geometry of the model must be designed in such a way that it allows an easy startup of the tunnel for all the experimental cases selected.
- **Expansion fans and reflected shocks:** The expansion fans generated by the trailing edge of the wedges must not interfere with the interaction point of the incident shocks. At the same time, the reflected shocks must not impinge on the wedges to avoid an unstart of the system.

The following sections will be dedicated to giving an overview of how these aspects affect the design of the wind tunnel model and the procedure followed to address each of them to obtain the final design presented in Section 3.3.4.

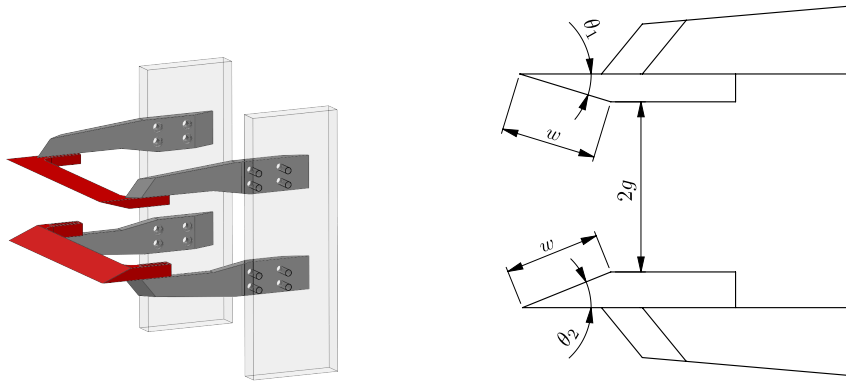

(a) (b)

Figure 3.5: (a) 3D render of the wind tunnel model used, (b) schematic representation of the main parameters that define the model.

3.3.1 3D Effects

As presented in Section 2.2.4, a significant amount of research has been done in order to understand the influence of three dimensional effects on shock-shock interaction systems. A useful practical guideline was presented in Fomin et al. (1996) and validated in Skews (1997). It is suggested that the aspect ratio of the wedges (AR_W) and of the wedge system's inlet (AR_I) must satisfy the following relations in order to keep the center section of the system as a two dimensional problem, (Fomin et al., 1996):

$$AR_W = b/c > 2.5 \tag{3.1}$$

$$AR_I = b/h > 1.25 \tag{3.2}$$

Where b is the span of the wedges, c their chord and h the distance between their leading edges. Regarding the wedges, by looking at Figure 3.5(b) it can be seen how Equation 3.1 can be expanded as:

$$AR_W = \frac{b}{w\cos(\theta)} > 2.5 \tag{3.3}$$

Because the wedges span the whole width of the test section, b is fixed at 272 mm. The only

variables remaining in Equation 3.3 are w and θ. Solving for them:

$$w\cos(\theta) < \frac{b}{2.5} \tag{3.4}$$

In the case of the inlet, Equation 3.2 can be expanded as:

$$AR_I = b/h = \frac{b}{2g + w(\sin\theta_1 + \sin\theta_2)} > 1.25 \tag{3.5}$$

Again, b is given by the width of the test section. Solving for the remaining variables, $2g$, w, θ_1 and θ_2 yields:

$$2g + w(\sin\theta_1 + \sin\theta_2) < \frac{b}{1.25} \tag{3.6}$$

It can be seen that the three dimensionality of the model can be evaluated through the relation between w, $2g$, θ_1, θ_2 and b defined in Equations 3.4 and 3.6. In order to avoid any influence of the edges of the wedges on the center part of the test section, the final model must satisfy these two equations for all test cases.

3.3.2 Startup Problem

A very important aspect when designing any experiment in a blowdown supersonic wind tunnel is the startup process of the system. When a tunnel of these characteristics is started, the system must go all the way from $u_\infty = 0$ to the desired supersonic conditions. The operational part of the TST-27 wind tunnel consists of four main sections (See Figure 3.1), following the flow direction: a settling chamber, a convergent-divergent nozzle that accelerates the flow to the desired conditions, the test section and a diffuser, where the flow is decelerated before being dumped into the atmosphere. The flow in the test section is driven by a pressure difference between the settling chamber (upstream of the test section), where the flow is held at a pressure equal to p_t, and the exit of the diffuser (downstream of the test section), where the flow reaches ambient pressure. This mechanism is not instantaneous and the flow through the tunnel must undergo a series of states before the system reaches steady state working conditions. As the tunnel is started and the flow becomes sonic at the tunnel's nozzle throat a normal shock is generated upstream of the test section. For the tunnel to reach working conditions, this normal shock must travel through the test section going through the four phases depicted in Figure 3.6.

For the shock to be able to travel through the test section two main critical conditions have to be satisfied: the total pressure losses through the test section must not be higher than a certain level and the test section with the model in it must allow a sufficiently high mass

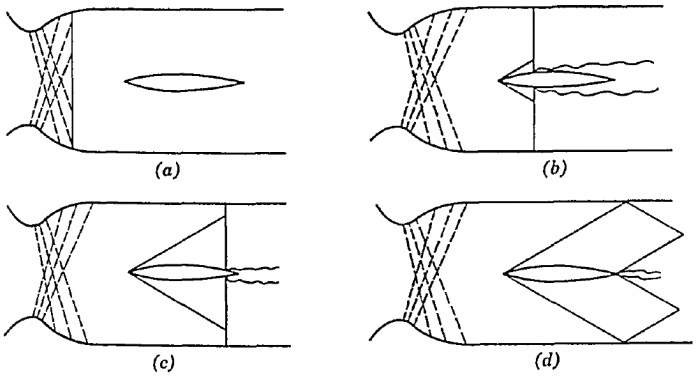

Figure 3.6: Four main phases the normal shock must undergo during the startup of a blowdown supersonic wind tunnel (Pope and Kennith, 1965).

flow in order for the normal shock to travel around it. Each of these conditions will be now discussed separately.

Total Pressure Losses

The initial p_t of the system is set by the pressure imposed at the settling chamber. As the flow travels downstream through the system, it will incur in various p_t losses caused by the different shock waves generated along the test section. In order to reach supersonic working conditions, the flow must be expanded through the convergent-divergent nozzle and overcome the back pressure imposed at the end of the diffuser. If the pressure losses are too high and the final p_t becomes too low, the system will not be able to overcome this back pressure and the normal shock will remain trapped in the test section. In previous projects carried out in the TST-27 it was estimated that the minimum p_t after the startup normal shock required for this facility to start is 1.6 bar. This is the criterion used in the current project.

During steady state conditions, p_t losses are not usually an issue due to most of the compression being carried by oblique shocks. This is usually a relatively efficient process and the losses are not high enough to trigger an unstart of the tunnel. On the other hand, during startup, these oblique shocks are combined with the traveling normal shock, as depicted in Figure 3.6. The critical case is given by the initial phase where the normal shock has not reached the model yet (Figure 3.6(a)). Under these circumstances, the flow has reached supersonic conditions before the shock and all of the compression is done by the normal shock, resulting in maximum p_t losses due to the low efficiency of this process. These losses can be computed through normal shock relations:

$$p_{t1} = p_{t0} \left[\frac{(\gamma+1)M_0^2}{(\gamma-1)M_0^2+2} \right]^{\frac{\gamma}{\gamma-1}} \left[\frac{(\gamma+1)}{2\gamma M_0^2-(\gamma-1)} \right]^{\frac{1}{\gamma-1}} \tag{3.7}$$

Where p_{t1} is the total pressure after the normal shock, p_{t0} the total pressure selected in the settling chamber and M_0 the selected Mach number in the test section. This way, Equation

3.7 can be used to compute the final total pressure after the normal shock during startup. Using Equation 3.7 and following the $p_{t1\text{Min}} = 1.6\,\text{bar}$ criterion, the following relation must be satisfied in order for the TST-27 wind tunnel to start:

$$p_{t0}\left[\frac{(\gamma+1)M_0^2}{(\gamma-1)M_0^2+2}\right]^{\frac{\gamma}{\gamma-1}}\left[\frac{(\gamma+1)}{2\gamma M_0^2-(\gamma-1)}\right]^{\frac{1}{\gamma-1}} > 1.6\,\text{bar} \tag{3.8}$$

Mass Flow Requirement

In order for the normal shock to be able to travel downstream of the model, the test section must be able to accommodate a mass flow high enough to achieve this. This is not usually an issue with an empty test section but it can become a problem once a model is introduced in it, specially if it covers the full span of the test section, such as the one used in this project. The reason for this is that a full span element in the test section can reduce the effective cross section of the system, which can in turn limit the mass flow that can travel through it. A schematic representation of the flow situation during startup with the current model in the test section is shown in Figure 3.7. As it can be seen, the two wedges form a convergent duct after the normal sock. Due to the fact that the flow becomes subsonic after the shock and that the duct is convergent, the flow undergoes an acceleration through the wedges. As in any convergent duct, the maximum Mach number that the subsonic flow can achieve through it is 1 at its narrowest cross-section. If the flow reaches $M = 1$ at a point before the throat of the system, the model will not be able to further expand the flow and the flow traveling through the wedges will reach an unsteady situation. The normal shock will not be able to pass through the model and the wind tunnel will not start.

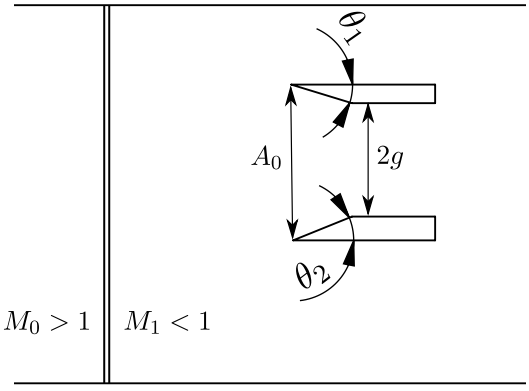

Figure 3.7: Simplified schematic drawing showing the wind tunnel model and the normal shock during the startup process.

The critical area ratio needed to achieve sonic conditions at the throat of the model can be computed by assuming an isentropic expansion through the convergent duct (Anderson Jr.,

2001):

$$\frac{A_0}{A^*} = f(M_1) = \frac{1}{M_1}\left[\frac{2}{\gamma+1}\left(1+\frac{\gamma-1}{2}M_1^2\right)\right]^{\frac{\gamma+1}{2(\gamma-1)}} \tag{3.9}$$

Where A_0 is the inlet of the convergent duct, M_1 the flow Mach number at the inlet and A^* the critical area or the area at which the flow becomes sonic. In order for the system to start and the normal shock to pass through the duct, the minimum area at the throat must be equal or larger than A^*. In Figure 3.7 it can be seen how A_0 can be computed as a function of $2g$, w and the two θ angles.

$$A_0 = (2g + w(\sin\theta_1 + \sin\theta_2))b \tag{3.10}$$

Where b is the span of the test section. Solving now for A^* in Equation 3.9 yields:

$$A^* = h^* b = \frac{[2g + w(\sin\theta_1 + \sin\theta_2)]b}{f(M_1)} \rightarrow h^* = \frac{2g + w(\sin\theta_1 + \sin\theta_2)}{f(M_1)} \tag{3.11}$$

Where h^* represents the minimum required vertical distance between the two wedges. As mentioned, M_1 represents the Mach number at the inlet of the wedges. During the startup situation this corresponds to the Mach number after the normal shock. Since the aim is to achieve working conditions, the Mach number before the shock will be the selected steady state Mach number (M_0). M_1 can now be computed as a function of M_0 through normal shock relations (Anderson Jr., 2001):

$$M_1 = f(M_0) = \left[\frac{1 + [(\gamma-1)/2]M_0^2}{\gamma M_0^2 - (\gamma-1)/2}\right]^{1/2} \tag{3.12}$$

Now the minimum required vertical distance between the two wedges for a successful startup can be computed as a function of the inflow Mach number and the inlet area through Equations 3.12 and 3.11.

3.3.3 Reflected Shocks and Expansion Fans

Once the wind tunnel is started and the model has reached steady state conditions, there are two extreme situations in which the experiment cannot be performed. The first one is when the reflected shocks impinge on the wedges and a set of reflected shocks emanate from them, leading to an unstart of the system. The second situation are configurations in which the trailing edge expansion fans impinge on the interaction point and disturb the interaction and

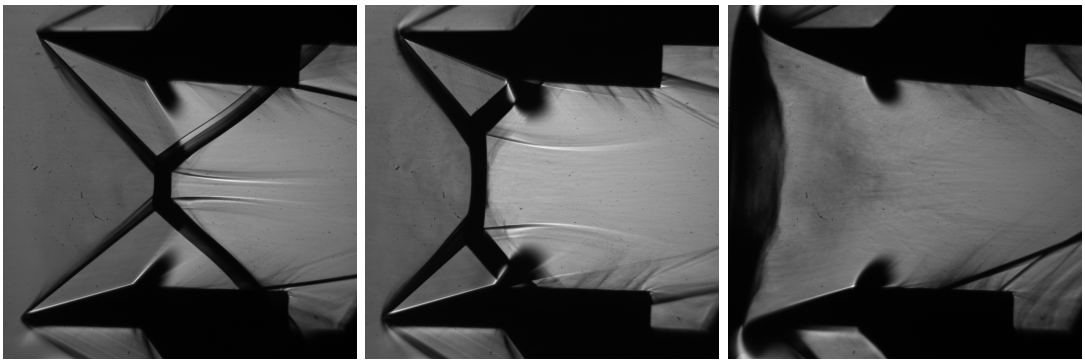

(a) (b) (c)

Figure 3.8: Schlieren image sequence of the model unstarting due to an impingement of the reflected shocks on the wedges. M_0 decreases from (a) to (c).

transition processes. These two situations must be always avoided in order to have a valid wind tunnel model.

A sequence of Schlieren images for decreasing M_0 obtained during the experiments is shown in Figure 3.8. It can be seen how, as M_0 is decreased, the incident shock angles increase, moving the whole shock pattern upstream. The situation is stable up to Figure 3.8(c) where, after the reflected shocks impinge on the wedges, the whole system unstarts and a bow shock is formed around the model. This image sequence illustrates the fact that, for a given wedge configuration, there is a minimum M_0 beyond which the model will unstart. This minimum M_0 is directly dependent on $2g$ and w. If $2g$ is decreased, the wedge line will intersect the reflected shock earlier, resulting in a higher minimum M_0 for an unstart. At the same time, if w is increased, the reflected shocks will intersect the wedge earlier, leading to an unstart at a higher M_0. It can be concluded that a decrease in $2g/w$ will always result in an unstart at a higher M_0. For this reason, $2g/w$ must be selected in combination with the lowest desired M_0 in order to avoid any unstarts during the experiments.

If the interaction point moves too far downstream, there is a risk of it being intersected by the expansion fans, disturbing this way the shock-shock interaction and the transition process. The shock angles decrease as M_0 is increased, which in turn moves the interaction point downstream and increases the risk of it interacting with the expansion fans. This means that the configurations with the highest risk of hitting the fans are the RIs with high M_0 values. If $2g$ is increased, the incident shocks will have to travel a larger distance before intersecting, increasing this way the risk of this interaction point hitting one of the expansion fans. At the same time, if w is decreased, the expansion fans will move upstream, reducing their distance to the interaction point. This way, it can be concluded that if $2g/w$ is increased, the risk of expansion fan interference grows. Because the worst cases are given by RI, analytical models can be used to predict the shock pattern under these circumstances and an accurate assessment of the risk of the expansion fans hitting the interaction point can be made.

It has been shown through the previous discussion that, in order to minimize the risk of the

shocks impinging on the wedges, $2g/w$ must be maximized. On the other hand, $2g/w$ must be minimized in order to avoid the expansion fans interfering with the expansion fans. This trade-off must be addressed when selecting the appropriate $2g/w$ value for the wind tunnel model.

3.3.4 Final Design

The final model is schematically shown in Figure 3.9 and its two main pieces, the top and bottom wedges, in Figures 3.10 and 3.11. The full technical drawings used for manufacturing can be found in Appendix A. The full model requires six additional parts: four horizontal supports, which link the wedges to the walls of the wind tunnel, and the two side plates, which act as a connection between the supports and the test section. These parts already existed before this project began so they are not further discussed here.

As seen in Figure 3.9, the final model is defined through $2g = 75\,\text{mm}$ and $w = 42\,\text{mm}$, resulting in $2g/w = 1.79$. As explained in Section 3.2.1 only one θ_1 case is analyzed, so the top wedge is unique. On the other hand, five θ_2 cases are studied, requiring five different bottom wedges. They are all designed with the same structure defined through two variables: α and θ_2, both of them shown in Figure 3.11. All remaining dimensions remain constant through all five wedges. One of these constant dimensions is w. As previously explained, $2g/w$ must be kept constant for all experiments, so with a constant w, $2g$ must also be fixed. This means that the distance between wedges must also remain constant. The side supports are also fixed for all runs, so the only way $2g$ can be controlled is by keeping the thickness of the bottom wedge constant. Because θ_2 is variable and w is constant, an additional negative angle, represented by α has to be added to the wedges to compensate for the change in thickness caused by θ_2. This angle is different for all wedges in order to accommodate the change in thickness created by a variable θ_2. For the $\theta_2 = 22°$ wedge, α is zero and increases as θ_2 is lowered. The model is designed to span the whole test section, so its span is kept constant for all top and bottom wedges at 272 mm.

In order to estimate if the model is sufficiently two-dimensional, the guidelines presented by Equations 3.3 and 3.5 will be used. In the case of the wedge, it can be seen how the left hand side of Equation 3.3 will decrease as θ does, making the minimum θ case the most critical. For the current model this is $\theta_2 = 10°$. This way, for $b = 272\,\text{mm}$, $w = 42\,\text{mm}$ and $\theta = 10°$:

$$\frac{b}{w\cos\theta} = 6.58 > 2.5 \tag{3.13}$$

Which indicates that all of the wedges are sufficiently two-dimensional for the current experiments. Regarding the wedge inlet, it can be seen in Equation 3.5, that the critical case will be the configuration with the largest $\theta_1 + \theta_2$. For the current model this is the $\theta_1 = 17°$, $\theta_2 = 22°$ configuration. Using $b = 272\,\text{mm}$, $w = 42\,\text{mm}$, $2g = 75\,\text{mm}$, $\theta_1 = 17°$ and $\theta_2 = 22°$,

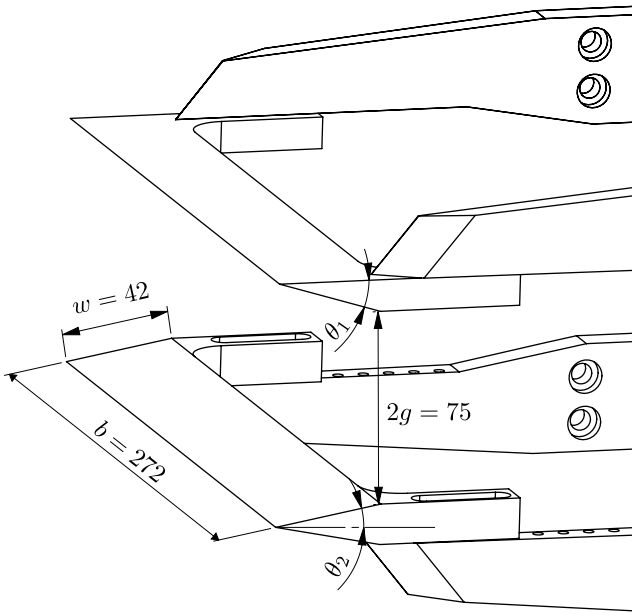

Figure 3.9: Schematic representation of the assembled final model with it's characteristic dimensions. All dimensions are in mm.

Equation 3.5 yields:

$$\frac{b}{2g + w(\sin\theta_1 + \sin\theta_2)} = 2.64 > 1.25 \tag{3.14}$$

Which also proves that the two wedge configuration is two dimensional enough for the current experiments.

Regarding the startup problem, in Section 3.3.2 it was explained how the experimental conditions and the model must satisfy two requirements in order for the tunnel to start correctly. Firstly, the total pressure after the startup normal shock (p_{t1}) must not drop below 1.6 bar. p_{t1} can be computed through equation 3.7. All of the $M_0 - p_t$ combinations that will be used during the experiments can be found in the test matrix in Table 3.1. The total pressure conditions after the startup normal shock can be computed by by plugging these $M_0 - p_t$ combinations into Equation 3.7. The obtained results are presented in Figure 3.12. As it can be seen, in all cases the total pressure after the startup shock is larger than the minimum required value for the tunnel to start. It can be concluded that the total pressure selected at startup is high enough to overcome the back pressure generated at the diffuser.

The second startup condition requires the model's throat to be big enough to accommodate the mass flow behind the startup normal shock. As explained in Section 3.3.2, the minimum vertical distance between the two wedges ($2g$ in this case) must be larger than a critical distance (h^*) where the flow would theoretically reach sonic conditions. h^* is a function of M_0, θ_1, θ_2 and the geometry of the wedges and can be computed through Equations 3.11 and 3.12. By plugging the startup M_0 conditions and the θ angles for all configurations, h^* can

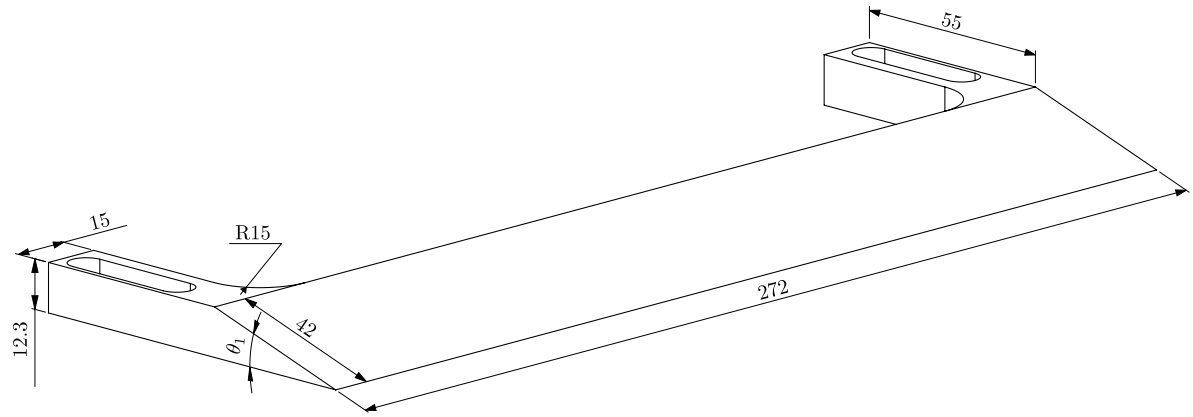

Figure 3.10: Schematic representation of the final design for the top wedge. All distances are in mm.

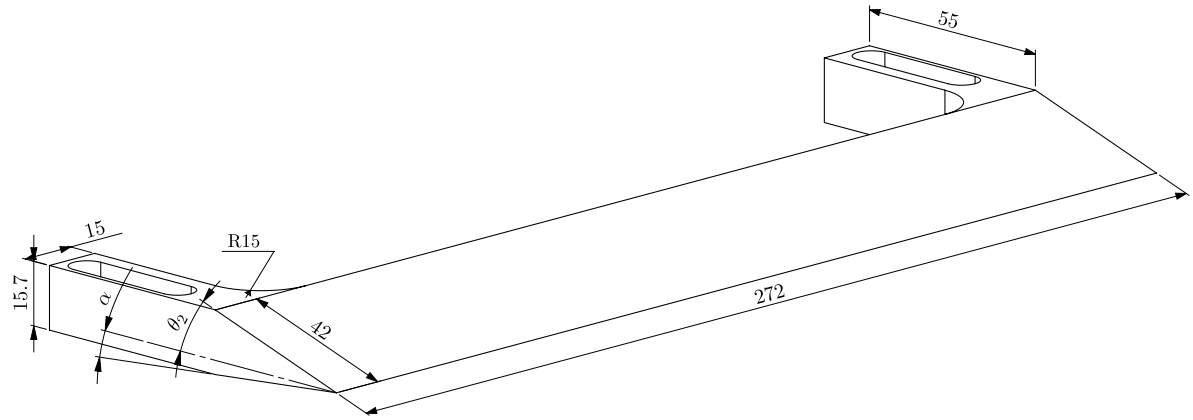

Figure 3.11: Schematic representation of the final design for the bottom wedges. α is the negative angle added to keep $2g$ constant. All distances are in mm.

be obtained for all experiments. The obtained results are shown in Figure 3.13. As it can be seen, $2g$ is about 2 mm larger than h^* for all startup conditions. This difference is assumed to be large enough for the model to accommodate the required mass flow during startup.

Finally, as explained in Section 3.3.3 the model should avoid any interference of the expansion fans with the interaction point and any reflected shocks impinging on the wedges. Regarding the first aspect, the most critical situation will always be at the startup point, due to the high M_0 values, which generate low shock angles. In order to estimate if there will be any interference, a prediction of the shock pattern at startup can be made by using analytical shock interaction theory. This is possible due to the fact that the model will always start in the RI domain. Through this it was found that there is a small separation between the expansion fans and the interaction point which is assumed to be enough to avoid any kind of interferences. In the case of the second requirement, the most critical situations will always be given in the MI domain, due to the low M_0 and large shock angles there. Due to the nonexistence of

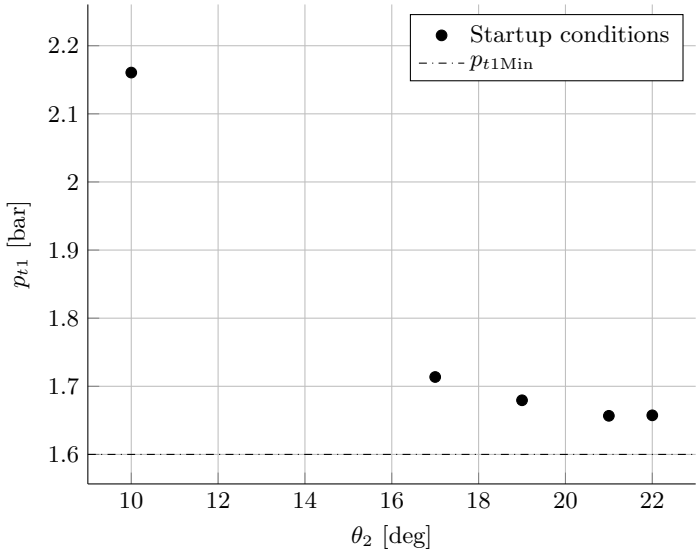

Figure 3.12: Total pressure losses during startup represented as the final total pressure after the startup normal shock (p_{t1}). The minimum estimated p_t required for the tunnel to start is shown as $p_{t1\text{Min}}$.

analytical methods in this domain, the shock pattern cannot be directly computed. In order to solve this, the RI shock pattern was calculated at the Detachment point, which is the lowest M_0 case in which an RI can exist. It was found that for these configurations, the distance between the reflected shock impingement point and the wedges was large enough to avoid any reflected shock impinging on the wedges. As previously explained, the distance between the interaction point and the expansion fans is expected to be relatively small. Because of this, the Mach Stem Height (MSH) at transition will also be small. This means that the location of the reflected shocks before and after transition should be very similar. The only issue is that the reflected shocks will move upstream as M_0 is decreased and the MSH grows. For this reason, special care must be taken during the experiments in order to not lower the M_0 too far and trigger an unstart of the model, as shown in Figure 3.8. Despite this, it can be concluded that there is a very low risk of the expansion fans interfering with the interaction point or the reflected shocks hitting the wedges and unstarting the system as long as M_0 is not excessively lowered.

In conclusion, the designed aerodynamic model should be two dimensional enough for the required experiments according to the empirical guidelines presented in Section 3.3.1. At the same time, the TST-27 wind tunnel should be capable of starting without excessive problems with the presented model inside it. Finally, the risk of any fan interference or an unstart due to the reflected shocks hitting the wedges is expected to be reasonably low.

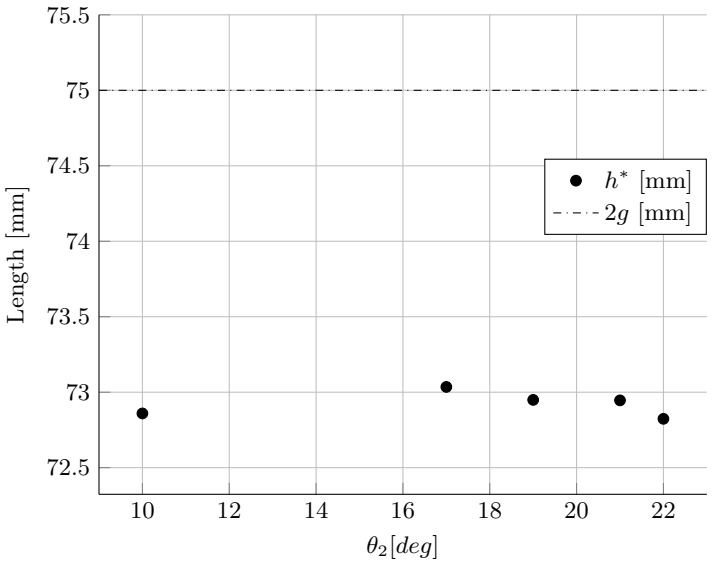

Figure 3.13: Plot showing the critical distance between the wedges needed for startup (h^*) compared to the actual distance ($2g$).

3.4 Experimental Procedure and Test Matrix

The Test Matrix containing the main parameters for the experiments performed in the current project is presented in Table 3.1. The experiments are divided into two main groups depending on the visualization technique used: Schlieren visualization or Focusing Schlieren. Schlieren visualization was the main flow visualization tool used in the project. For that reason, every geometry evaluated with this tool was tested five times in order to increase the statistical significance of the results. The Focusing Schlieren setup was used to qualitatively evaluate the flow topology of the shock system, so each geometry was tested only once with this visualization technique. The Maximum and minimum Mach numbers for each run were set following the design procedure presented in Section 3.2.2 and using the data presented in Figure 3.2. This was done by first setting M_{Max} and then computing the maximum p_t allowed by the tunnel for that flow condition. Doing this maximizes the Mach number range for that run due to the fact that M_0 can now be lowered all the way to the minimum M_0 allowed for that p_t.

All of the experiments are executed as follows. The tunnel is started at the highest M_0 value for that specific run which always corresponds to a configuration within the RI domain. The system then initiates the startup process until a steady state is reached. This moment is visually determined through a live Schlieren image feed sent to the control room. A typical starting process is shown in Figure 3.14. It can be seen how the steady state regime can be clearly distinguished from the unsteady startup flow. Once this steady state is reached, M_0 is slowly reduced all the way to its lowest value for that configuration. This makes the system traverse the whole dual solution domain to finally reach the MI domain. The process is then reversed until reaching again the initial M_0 condition and the tunnel is then shut down. The Schlieren image recording starts the moment the system reaches a steady state and is stopped

Table 3.1: Test matrix used for the experimental campaign.

Geometry	Run/s	θ_1	θ_2	p_t [bar]	M_{Max}	M_{Min}	M_{VN}	M_{D}	Visualization
1	1-5	17°	22°	6.0	3.20	2.40	2.98	2.64	
2	6-10	17°	21°	5.5	3.10	2.30	2.80	2.57	
3	11-15	17°	19°	4.9	2.95	2.20	2.56	2.44	Schlieren
4	16-20	17°	17°	4.4	2.80	2.10	2.38	2.33	
5	21-25	17°	10°	4.0	2.40	1.80	2.01	2.01	
1	26	17°	22°	6.0	3.20	3.20	2.98	2.64	
2	27	17°	21°	5.5	3.10	3.10	2.80	2.57	
3	28	17°	19°	4.9	2.95	2.95	2.56	2.44	Focusing
4	29	17°	17°	4.4	2.80	2.80	2.38	2.33	
5	30	17°	10°	4.0	2.40	2.40	2.01	2.01	

once the tunnel is shut down. This allows a visualization of the whole shock pattern evolution process.

In order to estimate the unsteadiness of the experimental procedure, the ratio of Mach number change rate (dM_0/dt) to the characteristic time scale of the problem (t_{Char}) needs to be evaluated. The problem becomes more unsteady the higher this ratio is. The Mach number rate of change can be approximated as:

$$\frac{dM_0}{dt} \approx \frac{(M_{\text{Max}} - M_{\text{Min}})}{t_{\text{Exp}}/2} \tag{3.15}$$

Where M_{Max} and M_{Min} are the maximum and minimum Mach numbers achieved during a given experimental run and t_{Exp} the time used for a given experimental run.

The characteristic timescale of the problem can be approximated as the time a freestream

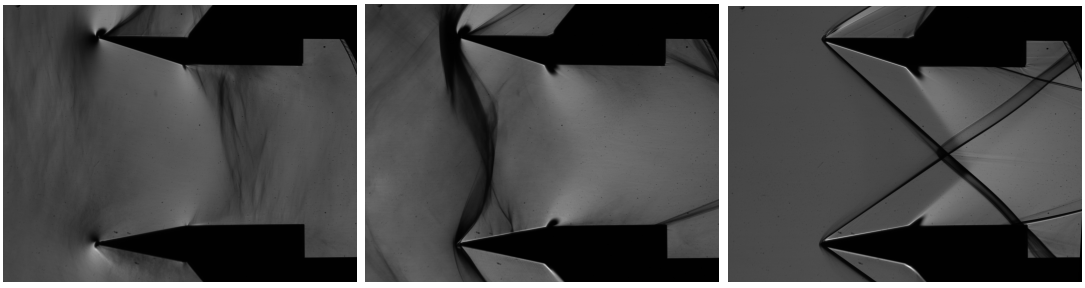

(a) (b) (c)

Figure 3.14: Starting sequence of the $\theta_1 = 17°$, $\theta_2 = 10°$ configuration. The flow starts in subfigure (a) and evolves to eventually reach steady state conditions in subfigure (c).

fluid particle takes to travel the length of the wedge hypotenuse. This can be computed as:

$$t_{\text{Char}} = u_\infty / w \tag{3.16}$$

Where u_∞ is the freestream flow velocity, which can be computed as a function of the Mach number and the freestream temperature:

$$u_\infty = M_0 \sqrt{\gamma R T_\infty} \tag{3.17}$$

Where T_∞ can be computed through isentropic flow relations:

$$T_\infty / T_t = (1 + \frac{\gamma - 1}{2} M_0^2)^{-1} \tag{3.18}$$

$M_{\text{Max}} - M_{\text{Min}}$ and t_{Exp} are approximately of the same order for all experiments. This way, it can be inferred that the most unsteady instant of the experiments is the point of lowest freestream velocity, which corresponds to the point of minimum M_0 within the $\theta_2 = 10°$ geometry. By looking at the parameters used during the experiments, $T_t = 280\,\text{K}$, $w = 42\,\text{mm}$, $t_{\text{Exp}} = 12\,\text{s}$, $M_{\text{Max}} = 2.40$ and $M_{\text{Min}} = 1.80$ can be assumed. By plugging these values into Equations 3.15, 3.16, 3.17 and 3.18 results in:

$$\frac{dM_0/dt}{1/t_{\text{Char}}} \approx 10^{-5} \tag{3.19}$$

This indicates that the Mach number rate of change is five orders of magnitude lower than the lowest characteristic time scale of the experiments. This is a clear indication that any experimental snapshot can be considered a steady state configuration.

Chapter 4

Flow Measurement Techniques

Three Flow Measurement systems were used throughout the current project: total and static pressure measurements, Schlieren visualization and Focusing Schlieren. Pressure readings were used to determine M_0 during the experimental runs. Schlieren visualization was the main flow visualization tool used to analyze the shock pattern. On the other hand, Focusing Schlieren was used to qualitatively asses possible three dimensional effects within the shock system. These three techniques and how they were implemented into the current project are discussed in Sections 4.1, 4.2 and 4.3.

4.1 Total and Static Pressure Measurements: M_0 Determination.

The main control variable in the present study is M_0. In order to determine its value, two pressure sensors were placed on the side walls of the test section and one in the settling chamber. This allowed to obtain continuous static and total pressure readings at a frequency of 5000 Hz during a run. Assuming an isentropic flow expansion through the nozzle, M_0 can be computed as:

$$\frac{p_s}{p_t} = \left(1 + \frac{\gamma - 1}{2} M_0^2\right)^{\frac{-\gamma}{\gamma - 1}} \rightarrow M_0 = \sqrt{\left[\left(\frac{p_s}{p_t}\right)^{\frac{\gamma - 1}{\gamma}} - 1\right] \frac{2}{\gamma - 1}} \tag{4.1}$$

Where p_s is the static pressure measured in the test section. Examples of typical pressure and M_0 profiles obtained during an experimental run are shown in Figure 4.1. As it can be seen in the example, p_s follows a rather smooth trend while p_t tends to oscillate around the nominal value of $p_t = 6$ bar. The effect of these oscillations on M_0 is almost nonexistent with M_0 showing a similarly smooth trend as p_s. Another important aspect in Figure 4.1 is the

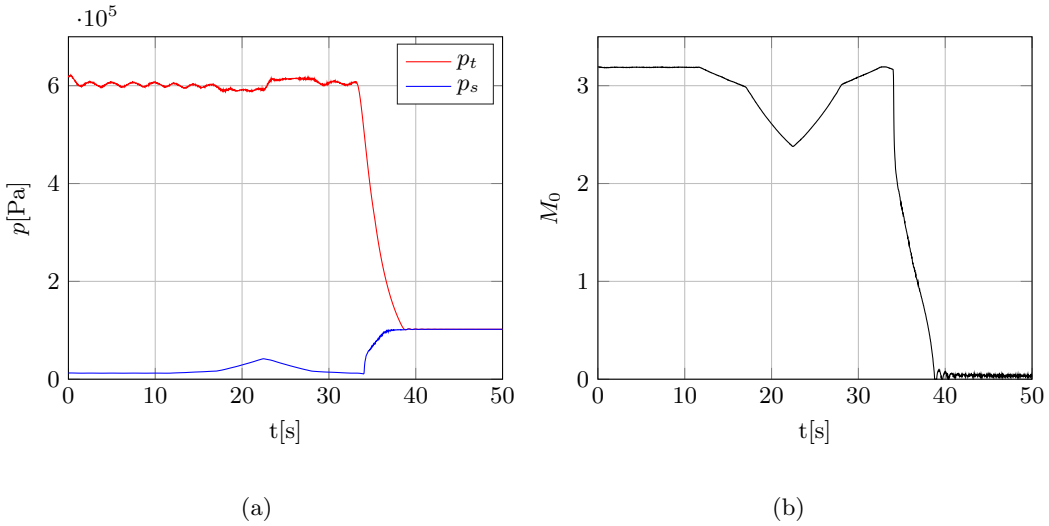

(a) (b)

Figure 4.1: Example of the pressure (a) and M_0 (b) profiles for an experimental run of the $\theta_1 = 17°$, $\theta_2 = 22°$ configuration. The nominal value for p_t was set at 6 bar.

shift in the rate of change of M_0 and p_s as soon as the system reaches approximately $M_0 = 3$. This was caused by the actuator system that changes the size of the nozzle throat. Once this system reaches $M_0 = 3$ it switches the mechanism and the rate of change of M_0 shifts. Despite this, the rate of change of M_0 is still small enough compared to the timescales of the problem in order to consider the flow steady at every snapshot.

4.2 Schlieren Visualization

Schlieren visualization was used as the main flow visualization tool for the current study, as it allowed a precise determination of the shock pattern at every instant of the run. The layout used is shown schematically in Figure 4.2. The light source was generated with a continuous white lamp, which was collimated through the first parabolic mirror, creating a parallel beam that traversed the test section. This beam was converged at the knife edge through the second parabolic mirror. In the case of the $\theta_2 = 10°, 17°$ and $19°$ experiments, the images were recorded with a LaVision High Speed 4M camera at a rate of 125 Hz and an exposure time of 100 µs. In the case of the $\theta_2 = 21°$ and $\theta_2 = 22°$ experiments, the camera used was a LaVision Imager sCMOS at a frame rate of 50 Hz and an exposure time of 100 µs. All images were obtained at a resolution of 2016×2016 pixels.

Different Schlieren and Shadowgraphy configurations were tested to asses the sensitivity and saturation threshold of the system and determine the ideal setup. The four main ones are shown in Figure 4.3. The Shadowgraphy setup was capable of generating very clean and clear images but it was not capable of capturing some of the details within the flow. Due to it only being capable of detecting the second gradient of the flow density field (Settles, 2001), some nuances of the expansion fans and slipline duct are lost. Once the knife edge is introduced,

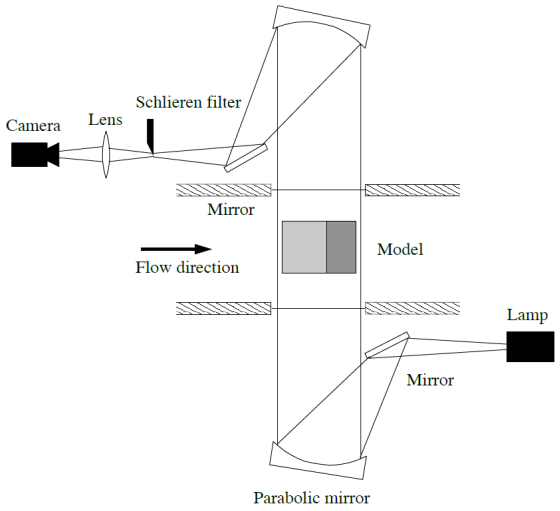

Figure 4.2: Diagram showing the Schlieren visualization setup used in the current study and its main components (Schrijer, 2010).

it can be seen how the horizontal knife configuration creates an asymmetric flow image, with a darker lower half due to the knife orientation. This feature would complicate the image processing needed to obtain the final results. At the same time, placing the knife vertically and on the left hand side of the camera can capture the shocks quite clearly but the expansion fans obscure the downstream part of the shock system loosing all information of the slip line duct. The final configuration chosen is shown in Figure 4.3(d). By placing the knife vertically and on the right hand side of the camera, the whole flow field can be seen in a very precise and clear way. The only downside is that the shocks appear considerably thicker than in the other configurations. As explained in Section 5.1, the Focusing Schlieren system shows that the actual shocks correspond to the trailing edge of the shock lines, the rest correlates with three dimensional effects on the window. Because of this, the thicker line issue can be solved by only analyzing the trailing edge of the shock lines.

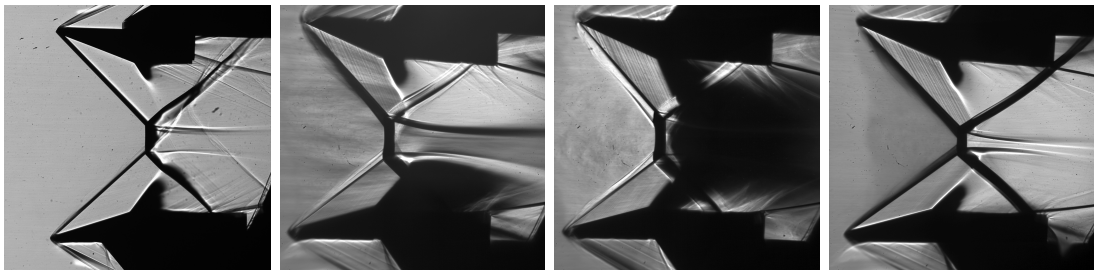

(a) Shadowgraphy (b) Schlieren with horizontal knife. (c) Schlieren with left vertical knife. (d) Schlieren with right vertical knife.

Figure 4.3: Resulting MI images for different conventional Schlieren and shadowgraph configurations.

4.3 Focusing Schlieren

Due to its infinite depth of focus, images recorded with a Schlieren visualization system are a composition of all density gradients present in the spanwise direction of the test section. This means that any undesired imperfections or flow features, such as three-dimensional effects near the edges, can contaminate the final image. A Focusing Schlieren setup can eliminate these unwanted features by reducing the depth of focus of the system to a thin slice around the plane of interest (Settles, 2001). A schematic of a typical focusing Schlieren setup is shown in Figure 4.4. As it can be seen, there are two main differences between a Focusing and a conventional Schlieren system: the converging light beam and the source and cutoff grids. These features enable its focusing ability in the following manner. The converging light beam that traverses the test section is no longer parallel or collimated as in the conventional setup. The depth of focus of any optical system depends on the maximum angle formed by the captured light rays that emanate from the observed object. A wide angle results in a thin depth of focus and a small angle in a large depth of focus, a parallel beam with an infinite depth of focus being the limiting case. This means that, due to the converging light beam, only a certain part of the test section can be kept in focus at the same time. The second key feature of a Focusing system is that the final image is constructed through a combination of source-knife pairs, as opposed to the single source and knife used in a conventional setup. This means that every point of the final image is composed by multiple light rays that converge at the image plane. Because all of these rays follow different paths before converging, not all of them will be affected by density gradients outside the plane of interest. This feature contributes to the elimination of unwanted features from the final image, such as 3D effects or window imperfections. More detailed information on the physical working principle of a Focusing Schlieren setup can be found in Weinstein (2010) and Settles (2001). The Focusing Schlieren system used in this project was the first of its kind built at TU Delft. For this reason, the following sections are dedicated to give a detailed overview of the design process followed and its integration in the TST-27.

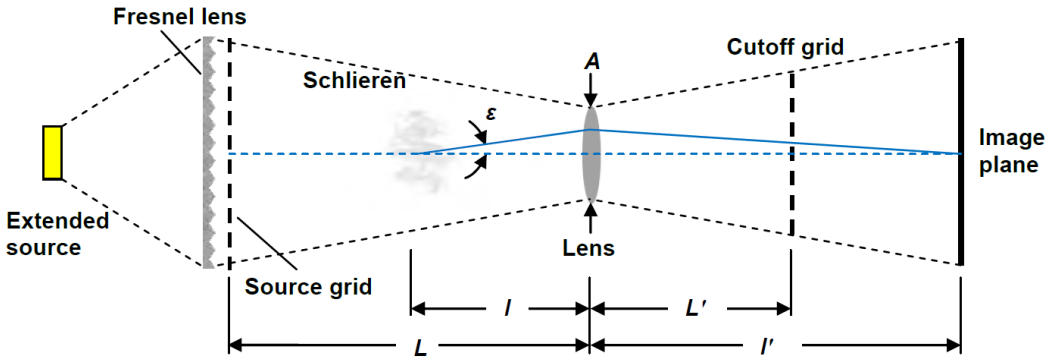

Figure 4.4: Schematic representation of the main elements involved in a Focusing Schlieren system (Floryan et al., 2012).

4.3.1 System Design

The performance of the Focusing Schlieren system was evaluated by using six sets of control variables:

- Characteristics of the focusing lens: Defined by its focal length (f) and its aperture (A).
- Optic elements distances: Defined through the distance between the focusing lens and the source grid (L) and the distance between the focusing lens and the plane of interest (l), see Figure 4.4.
- Size of the source grid (H_s).
- Sensitivity of the system: Defined through the minimum light deflection angle the system can detect (ε_{Min}).
- Unsharp resolution: Defines the blur size needed for a certain feature to blend into the background and disappear from the final image ($\Delta w'$).

These control variables define a set of dependent variables that can be grouped into five design aspects:

- Field of view (FOV): Defines the size of the flow field window that the system can observe.
- Depth of focus: Defines the thickness of the image plane that can be kept in focus at the same time. It can be divided into sharp depth of focus (Δz_s) and unsharp dpth of focus (Δz_u).
- Optic distances: Defined through the distance between the focusing lens and the image plane (l') and the distance between the focusing lens and the cutoff grid (L'), see Figure 4.4.
- Cutoff grid design: Defined through the width of the dark strips on the cutoff grid (d).
- Visual resolution of the system: Defined through the smallest distance that can be resolved in the resulting images (Δw).

Each of these design parameters and how they are affected by the independent and dependent variables are discussed in the following subsections.

Field of View (FOV)

This parameter determines the size of the flow field window that the system can capture. In the case of the current project and in order to capture the flow region of interest, FOV must be equal or lager than $2g$. In Figure 4.4 it can be seen how the tip of the source grid, the top

of the focusing lens and the horizontal form a right triangle. This way, assuming a square FOV, a simple proportionality rule can be applied to find the size of the FOV as a function of the optical distances, H_s and A:

$$\text{FOV} = \frac{l}{L}(H_s - A) + A \tag{4.2}$$

Figure 4.5 can then be obtained by plotting Equation 4.2 for different values of A and normalized with the selected $2g = 75\,\text{mm}$. As it can be seen, FOV is maximized when the aperture of the focusing lens is increased (increasing A) and when this lens is moved away from the test section (increasing l/L).

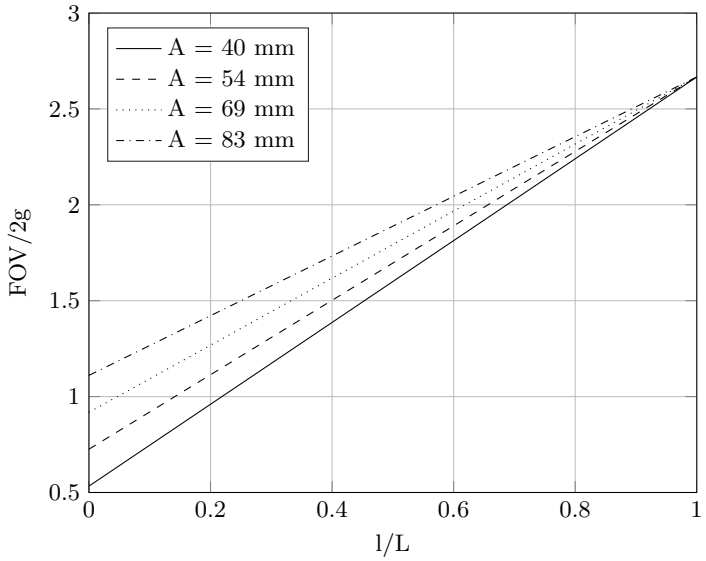

Figure 4.5: Change in FOV with the relative position of the focusing lens (l/L) and its aperture (A).

Depth of Focus (Δz)

Δz defines the thickness of the image plane which remains in focus in the final image, measured in the spanwise direction. This parameter can be defined in two ways: as a sharp depth of focus (Δz_s) or an unsharp depth of focus (Δz_u). The former defines the distance from the plane of interest at which a point of the image is no longer in focus but remains in the image. The latter defines the distance at which a point in the image disappears by blurring into the background. Because the objective of the current setup is to eliminate any 3D effects from the final image, the parameter of interest is Δz_u. This parameter can be computed as (Weinstein, 2010):

$$\Delta z_u = \frac{2w'l}{A} \tag{4.3}$$

Where $\Delta w'$ is defined as the necessary blur size for the image to properly blend into the

background. This value is very subjective and highly dependent on the flow features that must be blurred out. This dependency on $\delta w'$ is the main difficulty that arises when quantifying the depth of focus of the system. The evolution of Δz_u can be studied by plotting this parameter as a function of l/A for different values of $\Delta w'$, as seen in Figure 4.6. As shown, the depth of focus can significantly vary depending on the value selected for $\Delta w'$. This indicates that the depth of focus of the system changes depending on the flow feature that must be blurred out, with thicker flow features having a larger unsharp depth of focus. At the same time, Δz_u monotonically decreases with l/A due to the increase of light cone angle generated by this parameter. Because the aim of the current setup is to eliminate 3D effects from the final images, Δz_u must be minimized, thus l/A must be maximized. This can be done by moving the focusing lens closer to the test section (Decreasing l) or increasing the aperture of this lens (Increasing A).

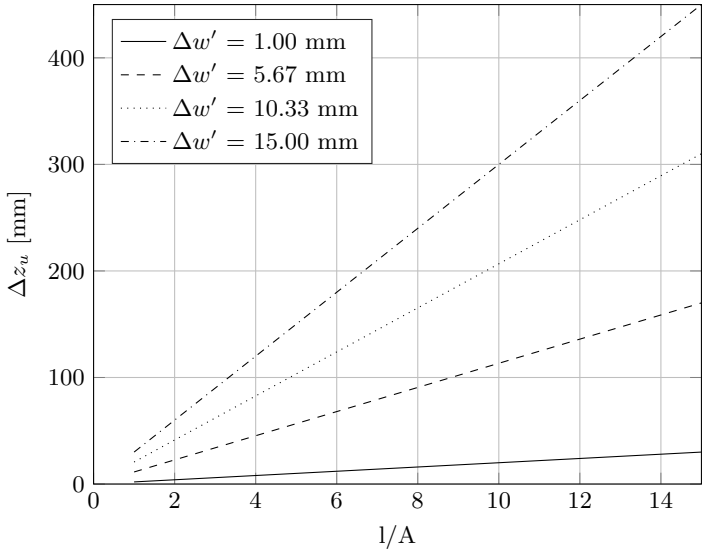

Figure 4.6: Evolution of unsharp depth of focus with l/A and the selected blur size ($\Delta w'$).

Optic Distances

In Figure 4.4 it can be seen that the image plane of the region of interest is located at a distance l' from the focusing lens, while the image plane of the source grid is placed at a distance L', with a distance $l' - L'$ between both planes. In order for the cutoff grid to disappear from the final image, it must go out of focus before the light reaches the final image plane. This way, $l' - L'$ must be large enough to avoid any black horizontal lines in the final image. l' and L' can be computed by using the thin lens equation:

$$\frac{1}{f} = \frac{1}{L} + \frac{1}{L'} \rightarrow L' = \frac{fL}{L - f} \tag{4.4}$$

$$\frac{1}{f} = \frac{1}{l} + \frac{1}{l'} \rightarrow l' = \frac{fl}{l - f} \tag{4.5}$$

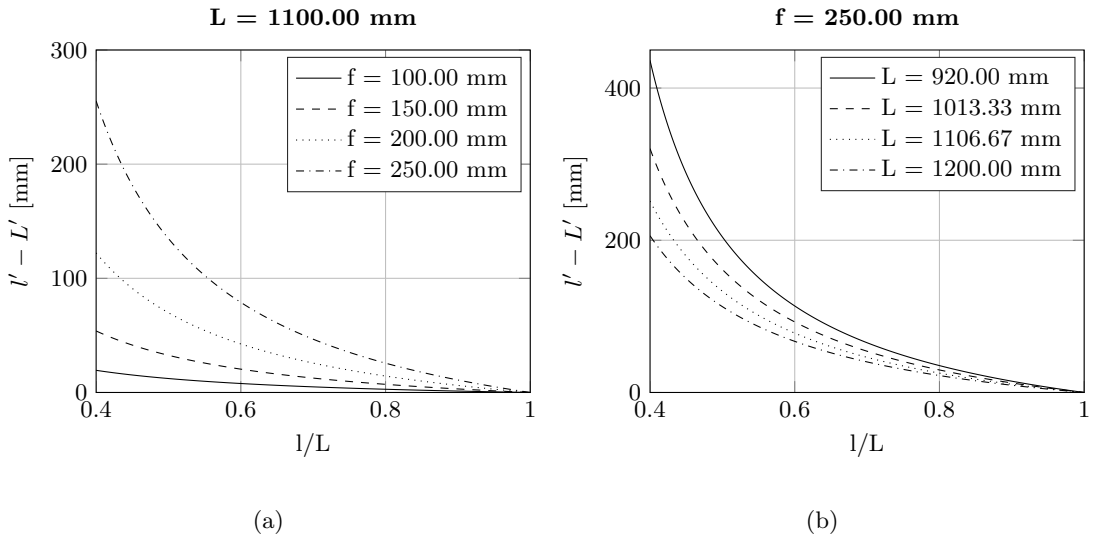

(a) (b)

Figure 4.7: Change of $l' - L'$ for a given value of f (a) and L (b).

Where f is the focal length of the focusing lens. Subtracting both equations yields:

$$l' - L' = \frac{fl}{l - f} - \frac{fL}{L - f} \tag{4.6}$$

This relation is plotted in Figures 4.7(a) and 4.7(b) assuming a fixed f and a fixed L, respectively. As shown, $l' - L'$ is increased by increasing f or decreasing l/L or L. The effective $l' - L'$ distance needed for the darks strips to properly blend in with the background in the final image is very subjective and highly dependent on the given problem, setup and grid design used. For this reason, for preliminary designs it is advisable to maximize this parameter by increasing f or decreasing L as much as possible.

Grid Design

The grid design for the current setup is defined by d. This is the width of the dark strips of the cutoff grid. In order to achieve a more uniform background, it is recommendable to use a uniform grid with the same size for both the dark and clear strips (VanDercreek, 2010). The total size of the cutoff grid (H_c) can be computed by applying the magnification factor $\frac{f}{L-f}$ to the source grid (H_s), which is always maximized to cover the whole Fresnel lens. d depends on the sensitivity of the system (ε_{Min}). If it is assumed that the minimum change in brightness that the system can detect is of 10% and a 0.5 cutoff is used, the derivation presented in Floryan et al. (2012) can be used to obtain:

$$d = 2\varepsilon_{\text{Min}} \frac{L'(L - l)}{20626L} \tag{4.7}$$

Where ε_{Min} is measured in arcsec. Figure 4.8 can be obtained by plotting Equation 4.7 for different values of ε_{Min}. As it can be seen, d decreases as the sensitivity of the system is increased (ε_{Min} is decreased). The cutoff grid was created by printing it on transparent slides which limits d at a minimum value due to the finite resolution of the printer used. At the same time, as d decreases, the difficulty of aligning the two grids to make the system work increases. These two factors set the minimum value of d at approximately 0.5 mm. For this reason, any system designed for the current project must have a d equal or larger than 0.5 mm.

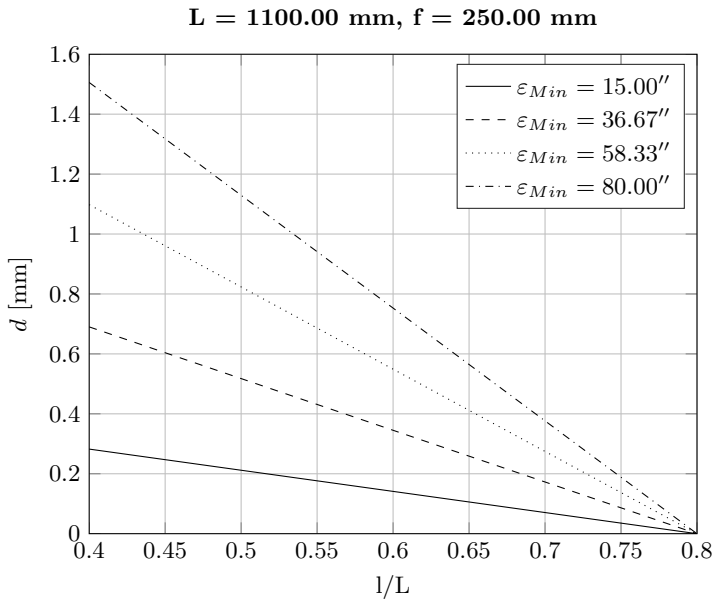

Figure 4.8: Variation of d as a function of l/L for different values of ε_{Min}.

System Resolution

If the quality of the camera and the optic elements used are assumed to be good enough, the resolution of the Focusing Schlieren setup is limited by diffraction effects. As discussed in Weinstein (2010) the slits the light must go through at the cutoff grid are thin enough to introduce a considerable diffraction error. If it is assumed that these effects dominate the resolution of the system, the maximum resolution that can be achieved is:

$$\Delta w = \frac{2(l' - L')\lambda}{(l'/l)d} \tag{4.8}$$

Where λ is the wavelength of the light used. Assuming a typical white light in the blue-green wave region, a value of $\lambda = 0.5\,\mu\text{m}$ can be used. Grouping up terms in Equation 4.8, the following relation can be obtained:

$$\Delta w = K\frac{l'^2 L - l'L'L}{lL' - l^2 L'} \tag{4.9}$$

Where K is a constant for a given sensitivity and wavelength, that can be obtained by replacing d through Equation 4.7:

$$K = 20626\frac{\lambda}{\varepsilon_{\text{Min}}} \tag{4.10}$$

Where ε_{Min} is measured in arcsec. By plotting Equation 4.9 for a given L and f and various values of ε_{Min}, Figure 4.9 is be obtained, showing how the resolution of the system decreases (Δw increases) as the sensitivity is increased (ε_{Min} is decreased). This means that the sensitivity of the system has an upper bound depending on the minimum resolution required for the system. At the same time, the resolution also decreases as the focusing lens is moved closer to the test section (l/L is decreased).

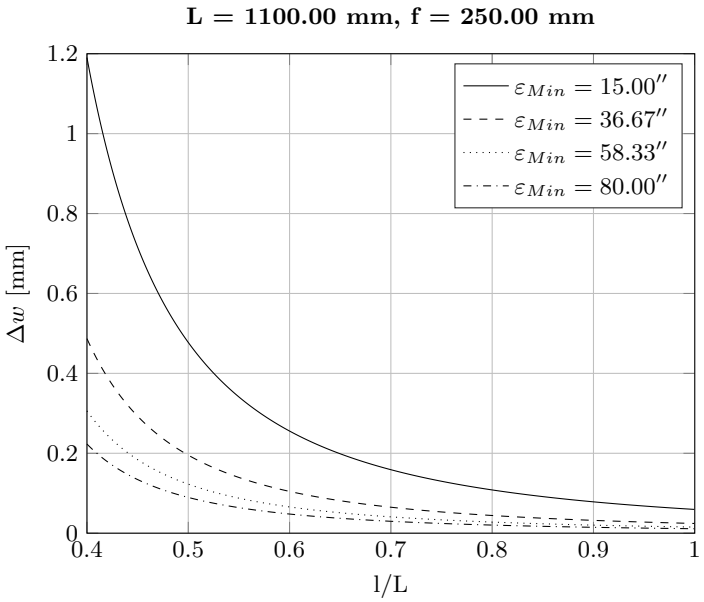

Figure 4.9: Change of the Focusing Schlieren system's resolution with ε_{Min} and l/L for a given L and f.

System Optimization

Now that the main variables of the system and their interactions are understood, the system can be designed and optimized for the current experiments. In order to get a good overview of the flow field, the FOV must be maximized, with a minimum required height of $2g$. Because the main goal of the system is to minimmize 3D and other unwanted effects, Δz_u must be minimized. In order to eliminate the cutoff lines from the final images $l' - L'$ must be maximized. Finally, regarding the grid design, the size of the dark strips on the cutoff grid must have a minimum size in order to maintain an acceptable resolution. Because some of these parameters conflict each other, the following iterative method was followed in order to reach the final design:

1. Maximize A: Figures 4.5 and 4.6 show it increases the FOV and decreases Δz_u.
2. Minimize l/L: It is proven through Figures 4.9 and 4.5 that this improves the resolution and FOV although it conflicts with the maximization of $l' - L'$, as seen in Figure 4.7.
3. Minimize l: This further reduces Δz_u but conflicts with the previous step. At the same time, if l reaches a value close to f the image size will rapidly grow, making the optical setup hard to assemble.
4. Maximize f: As seen in Figures 4.7 and 4.8, this maximizes $l' - L'$ and d.
5. Evaluate the performance of the resulting system. If it is not satisfactory, repeat steps 1 to 4.

The previous loop was executed for several iterations until final design was reached. This final setup is presented in the following section.

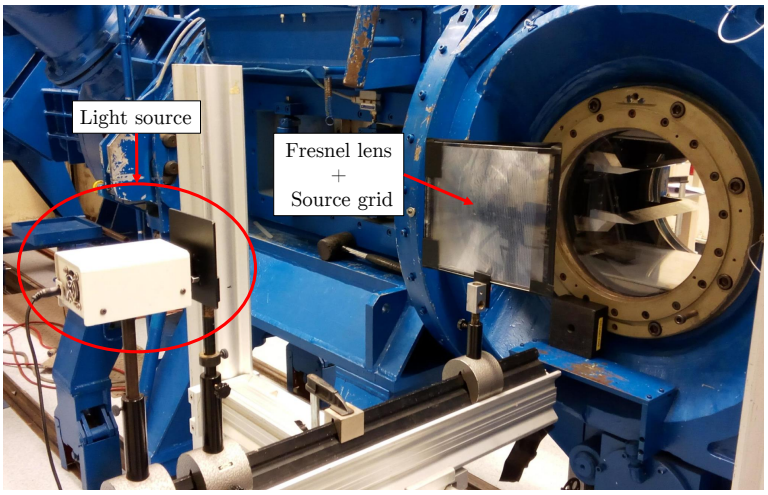

Figure 4.10: Source segment of the Focusing Schlieren system used for the current project, mounted around the TST-27 test section.

4.3.2 Final Setup

The parameters chosen for the final Focusing Schlieren setup are summarized in Table 4.1. The final system is built according to the diagram shown in Figure 4.4 with the addition of a relay lens of $f = 250\,\text{mm}$ placed between the cutoff grid and the Image plane, as shown in Figure 4.11. This is done in order to reduce the size of the final image so it can fit in the camera sensor. The system is built around the test section of the TST-27 wind tunnel with the source and camera segments on opposite sides of the tunnel. All of the elements are mounted onto a single rigid structure in order to ensure the correct alignment of all components. The source part of the setup is shown in Figure 4.10. The light source used is the same continuous white lamp that was used for the Schlieren visualization setup. The Fresnel lens, used to ensure a more uniform and brighter source, is mounted with the source grid placed directly

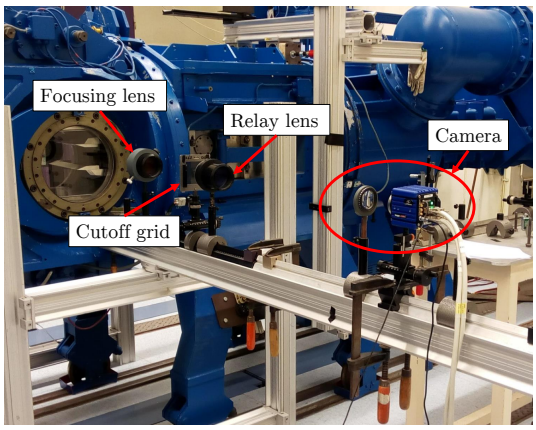

Figure 4.11: Camera segment of the Focusing Schlieren system used for the current project, mounted around the TST-27 test section.

Table 4.1: Design variables used for the final Focusing Schlieren setup.

Independent variables		Dependent variables	
f	250 mm	FOV	142 mm
A	83 mm	Δz_u	26 mm
l	550 mm	l'	458 mm
L	1100 mm	L'	324 mm
H_s	200 mm	d	0.47 mm
ε_{Min}	30″	Δw	0.24 mm
$\Delta w'$	2 mm		

in front of it. The camera side of the system is shown in Figure 4.11. The focusing lens is set directly in front of the test section at the distance prescribed by l and ensuring the whole light cone generated by the Fresnel lens is captured by it. The cutoff grid is mounted on a support that must be placed at exactly the image plane location of the source grid. One of the hardest parts of mounting any Focusing Schlieren system is the proper alignment of the bright stripes of the source grid image and the dark ones of the cutoff. To facilitate this, the cutoff support is equipped with a fine tunning mechanism that allows a precise alignment in the sideways and upwards/downwards directions. The relay lens is placed as close as possible to the cutoff grid in order to maximize the amount of light it can capture. All images are recorded with a LaVision Imager sCMOS camera at a frame rate of 50 Hz, an exposure time of 30 µs and a resolution of 2016×2016 pixels. All geometries were tested with a fixed focal plane in order to compare the resulting images with those obtained with the regular Schlieren setup. The results can be found in Section 5.1.1. In order to get a better insight of the flow topology of a MI system, an additional run is performed for a single geometry where the focal plane is slowly shifted through the test section in the spanwise direction while keeping a stable MI configuration. This is achieved by moving the camera in the spanwise direction while the tunnel is running. The results for this experiment can be found in Section 5.1.2.

Chapter 5

Results and Discussion

The current Chapter is dedicated to showing and analyzing the results obtained through the experimental setup and flow measurement techniques presented the previous Chapters. The discussion begins in Section 5.1 with the Focusing Schlieren results and how they compare to those obtained through the Schlieren visualization system. The latter are separately analyzed in Section 5.2. The Mach stem height results are presented in Section 5.4 together with a summary of the data processing methods used to obtained them. The Chapter concludes by discussing the transition points detected during the experiments . As explained in section 5.4, a noticeable deviation was found between the design θ_1 and θ_2 values and the actual angles measured during the wind tunnel tests. For the remaining of the report the nominal angles will be referred to as θ_{1N} and θ_{2N} and the actual angles measured at transition as θ_{1T} and θ_{2T}.

5.1 Focusing Schlieren and Three-dimensional Effects

As explained in Chapter 4, a qualitative understanding of the topology of the flow and possible influence of three-dimensional effects on the plane of interest was obtained by means of Focusing Schlieren visualization. Two type of tests were performed in order to achieve this. The first one was done by fixing the plane of focus of the system in the center of the test section while the M_0 was varied. In the second type, M_0 was kept constant while maintaining a stable MI shock pattern and the plane of focus was moved through the test section in the spanwise direction. Each of these experiments and the corresponding results are discussed in Sections 5.1.1 and 5.1.2.

5.1.1 Fixed Plane of Focus Diagnostics

In order to perform the fixed focal plane experiments, the plane of focus of the Focusing Schlieren system is placed in the center of the test section. This is done in order to maximize the distance from any three-dimensional effects generated at the walls or at the edges of the wedges. To achieve this, the system is calibrated by adjusting the position of the camera until the image of the center plane of the test section appears as sharp as possible. Once the plane of focus is fixed, experiments are performed according to the procedure presented in Section 3.4 and images are continuously obtained to visualize the shock pattern evolution. This test is performed once for each geometry, as seen in Table 3.1. All of the runs lead to similar results and conclusions. For this reason, and for the sake of clarity and conciseness, only the results for the $\theta_{1N} = 17°$, $\theta_{2N} = 22°$ configuration are shown and discussed in the current section. RI and MI images obtained through the Focusing Schlieren system for the rest of geometries can be found in Appendix B.

Two pair of images obtained with the Schlieren and Focusing Schlieren systems for the same M_0 and $\theta_1 - \theta_2$ geometry are shown in Figure 5.1. Images (a) and (b) show a configuration deep in the RI domain, resulting in a stable RI configuration. Images (c) and (d) show the opposite case, with the system far into the MI domain, resulting in a stable MI shock pattern. As it can be seen, both techniques clearly capture the main flow elements of the interactions, namely the incident and reflected shocks, the expansion fans, the Mach stem and the sliplines, although there are some noticeable differences. The most important one is that images (b) and (d) show the shocks in a much thicker way than images (a) and (c). The reason for this is that the Focusing system is capable of only showing the flow features present at the plane of focus, while keeping everything else out of focus. On the other hand, the Schlieren system not only captures the shocks present in the plane of interest but also any flow features present anywhere along the span of the test section, including the side walls and wedge edge regions. By comparing both sets of images, it can be seen how the shocks captured with the Focusing system correspond with the downstream edges of the black lines captured at the shock locations in the Schlieren image. This match is highlighted in the Figure by the superimposed red dashed lines. It can then be inferred that the rest of the dark lines must be attributed to three-dimensional flow effects. This is further explained in Section 5.1.2. Focusing Schlieren images without the red lines can be found in Appendix B.

5.1.2 Variable Plane of Focus Diagnostics

The goal of this test is to study the three-dimensional topology of the MI shock patterns generated with the current setup. This test is only performed once, with the selected geometry being $\theta_{1N} = 17°$, $\theta_{2N} = 22°$. It is initialized in the same way as the conventional tests at the maximum possible M_0 for the given configuration ($M_0 = 3.2$ in this case). Once the tunnel is started, the M_0 is reduced until a stable MI pattern with a large Mach stem is obtained. At this point, M_0 is frozen and the image acquisition system is activated. Once this is achieved, the plane of focus is moved from one window of the test section to the other by moving the position of the camera. This guarantees the coverage of every spanwise plane of the of the

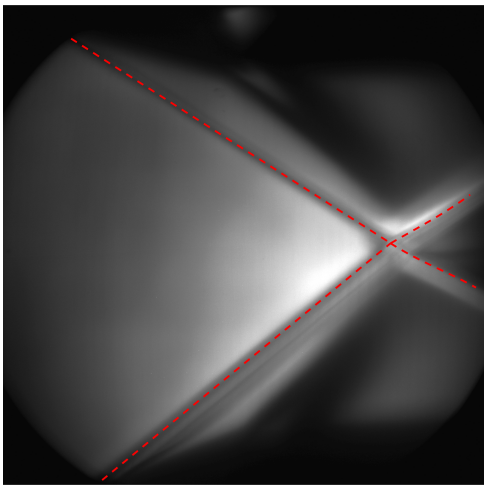

(a) RI, Focusing Schlieren, $M_0 = 3.13$.

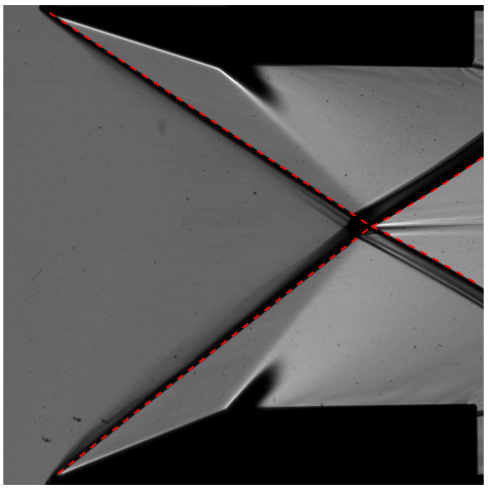

(b) RI, Schlieren visualization, $M_0 = 3.13$.

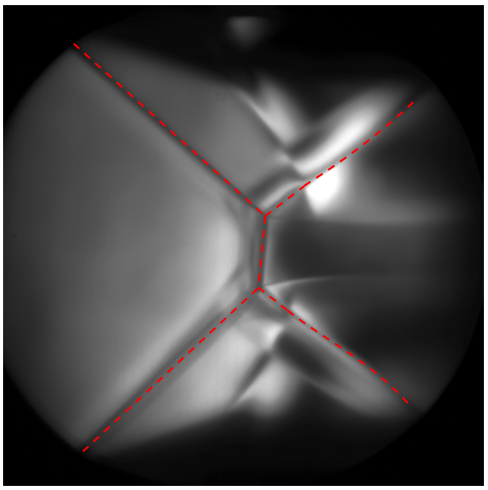

(c) MI, Focusing Schlieren, $M_0 = 2.45$.

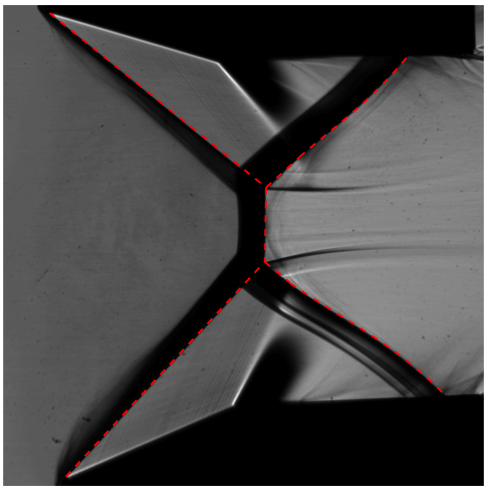

(d) MI, Schlieren visualization, $M_0 = 2.45$.

Figure 5.1: Comparison of two RI and MI images obtained with both the Focusing Schlieren and Schlieren visualization setups for the $\theta_{1N} = 17°$, $\theta_{2N} = 22°$ configuration. The red dashed lines are added to highlight the common features between the Schlieren visualization and Focusing Schlieren images.

test section.

Four different images obtained during the test are shown in Figure 5.2. Each image belongs to a different test section plane with Figure 5.2(a) being placed in the center of the test section, Figure 5.2(d) on the window closest to the camera and the remaining two images at equally spaced intermediate planes. As shown, when the plane of focus is placed in the center of the test section, the MI shock pattern, the expansion fans and the slipline duct appear in a very sharp way. At the same time, some additional features, such as some faint shadows ahead of the shock waves, can still be seen but they are considerably blurred out of focus. As the plane of focus is moved away from the center plane in Figures 5.2(b) and 5.2(c), it can be seen how the shock pattern becomes progressively fainter and less sharp. At the same time, the previously mentioned features ahead of the shocks start to appear darker and sharper. This tendency continues all the way to the final window plane, shown in Figure 5.2(d). In this last image it is shown how the original MI shock pattern that was seen in the center plane can no longer be seen, replaced by a different flow structure. In this case, the slipline tube seems to be hidden behind a cloud of non-uniform flow. At the same time, the incident shocks are preceded by two additional lines. Visual inspection of the recorded images reveals that both the flow behind the reflected shocks and the lines ahead of the incident shocks are more unstable and oscillate a lot more than the actual shocks. This leads to the conclusion that these new flow features probably correspond to a detached boundary layer flow at the window, caused by the sharp negative pressure gradient imposed by the incident and reflected shocks. This detached flow is convected downstream resulting in the large non-uniform flow region downstream of the reflected shocks. Because this phenomenon is generated at the windows, the slipline tube is obscured by it when the plane of focus is placed at the window closest to the camera. This conclusion is consistent with the one obtained after the fixed plane of focus experiment (see section 5.1.1), where it was found that the main three dimensional effect present in the current setup is the flow detachment at the windows.

In previous studies, such as Ivanov et al. (2001b) and Sudani et al. (2002), shock patterns, caused by edge effects, containing both MI and RI at different points along the span of the wedges were observed. As seen in Figures 5.2(a) through 5.2(c), the size of the Mach stem remains approximately constant throughout the test section. It must be noted that, due to the convergent light beam, images in the foreground are optically magnified. This means that features closer to the camera will appear larger even if they are the same size as others further away. Because of this, a small change in the Mach stem can still be seen in the images. The exception are the windows, where the Mach stem disappears in Figure 5.2(d) behind the large region of detached flow. It can be concluded that no flow fields containing RI and MI configurations simultaneously were found in the current setup. This could be attributed to the fact that the wedges covered the full span of the test section, minimizing this way the effect of the edges. Because these patterns are usually caused by the influence of the wedge edges on the interaction point, this reinforces the conclusion that the only significant three dimensional effect present in the current setup is the boundary layer separation present at the walls. As seen in Section 5.1.1 the error introduced by these effects can be minimized by considering only the downstream edge of the shocks when processing the Schlieren images.

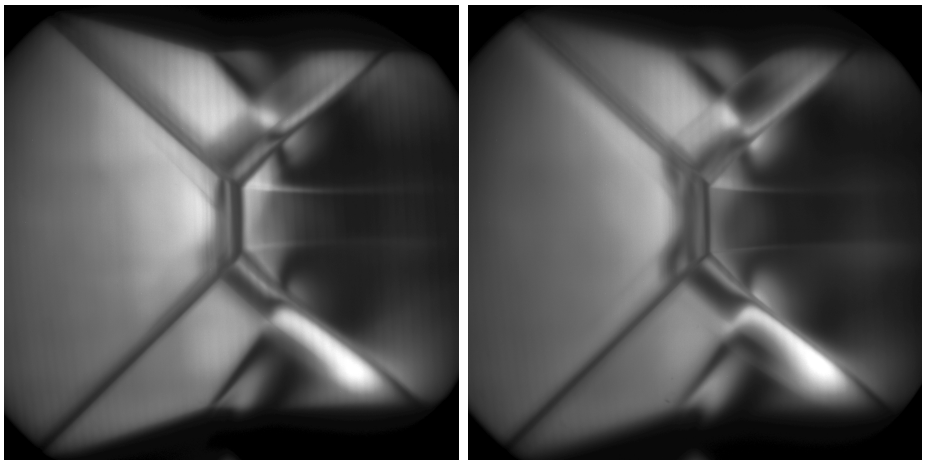

(a) Center plane (b) First intermediate plane

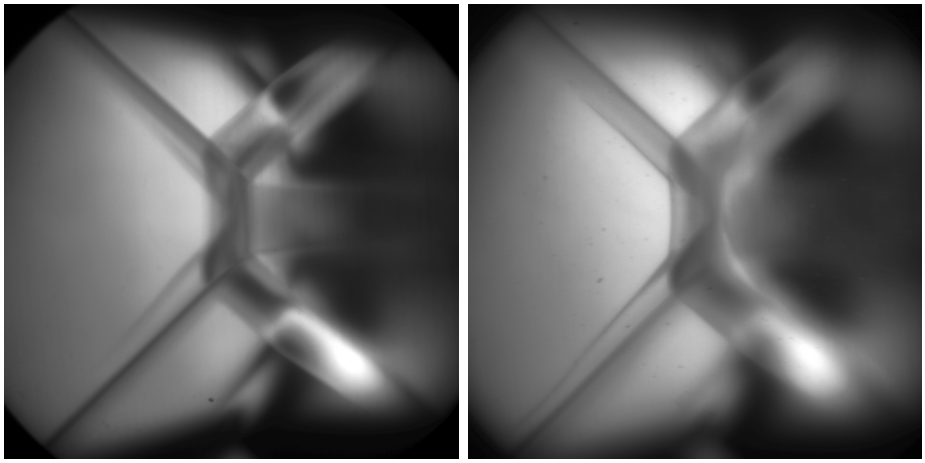

(c) Second intermediate plane (d) Window plane

Figure 5.2: MI images obtained with the Focusing Schlieren system at different image planes for the $\theta_{1N} = 17^{\circ}$, $\theta_{2N} = 22^{\circ}$ configuration at $M_0 = 2.26$. The image plane was moved from the center of the test section (a) to the window (d). Images (b) and (c) show intermediate planes between these two extremes with (c) being located at one third of the distance between the center plane and the window and (d) at two thirds of the same distance.

5.1.3 Focusing Schlieren Overall Performance

The experiments presented in this section show that a Focusing Schlieren system can be a useful tool to analyze shock-shock interactions. The setup used yields very useful results that give a deeper insight of the flow topology of a shock-shock interaction. Although, according to theory, the system can eliminate 3D effects from the final image, it can be seen in Figures 5.1 and 5.2 that some shadows of these features can still be found in the final images. There are two reasons for this. The first one is that, as explained in Section 4.3, the depth of focus needed for certain features to disappear is highly dependent on their shape and characteristics. The second is that no matter what the depth of focus is, some light rays will always have to traverse the 3D regions near the walls as they travel through the windows. Because of this, the light beam used for this type of setup will always be influenced by three-dimensional effects, although in a much lower degree than with a Schlieren visualization setup. This means that, although the depth of focus can always be reduced by optimizing the system, 3D effects will always have an influence on the final image. Another issue with the Focusing Schlieren system is the optic magnification caused by the convergent light beam. This can lead to some unwanted effects in the final images such as the obscuring of regions near the wedge tips due to the enlarged image of the wedge near the camera window. This feature becomes important in two dimensional geometries with slender models, it should not be an issue in other more three-dimensional geometries.

5.2 Schlieren Visualization

Schlieren visualization was used as the main flow visualization technique in the current project. The main reason for this is that this setup could generate clear and accurate images of the flow field at every instant. The current section is dedicated to presenting the qualitative information that can be extracted from these images. As shown in Table 3.1, this technique was used five times for each geometry. For the sake of clarity, only two of these runs will be discussed here: one for the $\theta_{1N} = 17°$, $\theta_{2N} = 22°$ geometry and one for the $\theta_{1N} = 17°$, $\theta_{2N} = 10°$ geometry. The former represents a case with a dual solution domain region and the latter a case without it.

5.2.1 $\theta_{1N} = 17°$, $\theta_{2N} = 22°$ Geometry

Figure 5.3 shows the shock pattern evolution of one of the runs obtained with the Schlieren visualization system for the $\theta_{1N} = 17°, \theta_{2N} = 22°$ geometry. According to the procedure presented in section 3.4, the run starts at the maximum possible M_0 value for that configuration, within the RI domain, where a clear RI shock pattern can be seen in Figure 5.3(a). The incident shocks interact in the center of the image generating the reflected shocks that are later curved due to the effect of the expansion fans. Due to the asymmetry of the wedges, a slipline is generated separating the two distinct regions behind the reflected shocks. As M_0 is reduced, the incident shock angles increase and the transition point is reached, as shown in

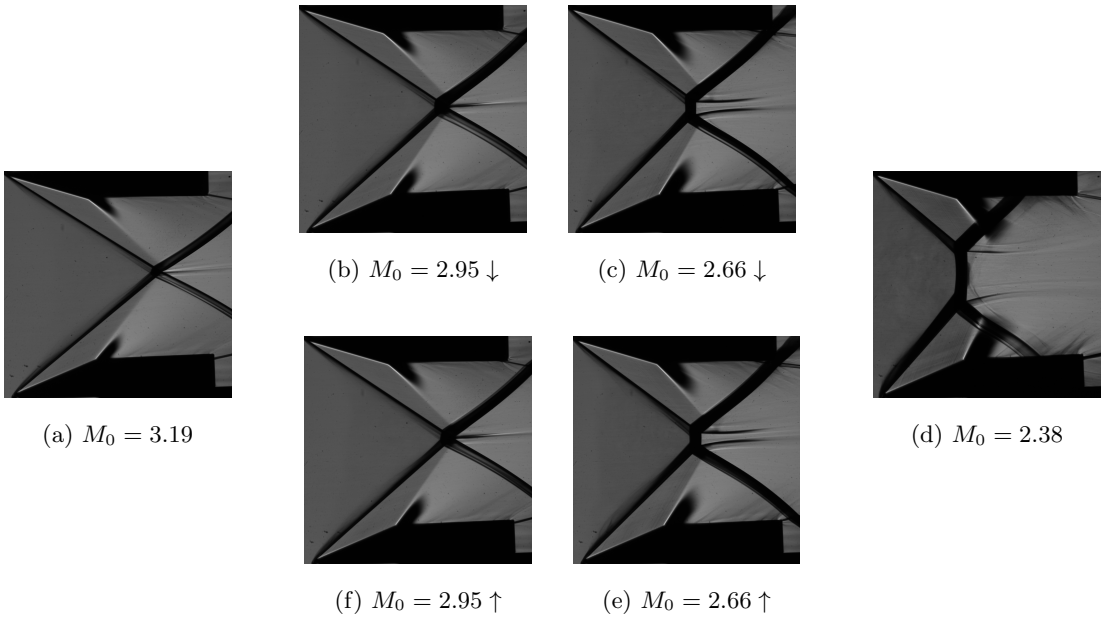

(a) $M_0 = 3.19$ (b) $M_0 = 2.95 \downarrow$ (c) $M_0 = 2.66 \downarrow$ (d) $M_0 = 2.38$ (f) $M_0 = 2.95 \uparrow$ (e) $M_0 = 2.66 \uparrow$

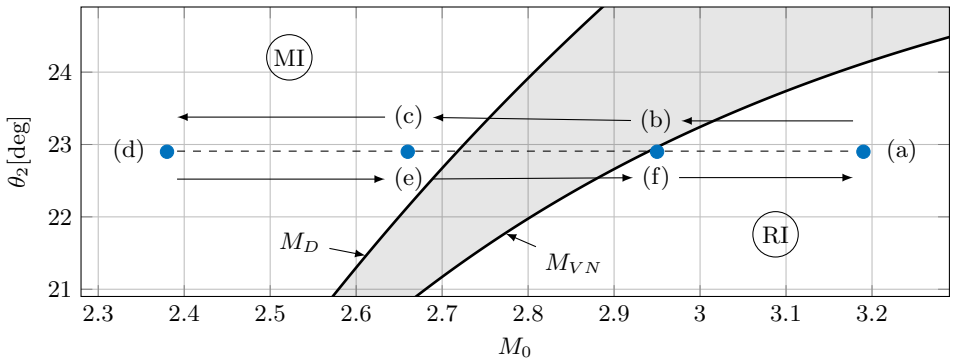

Figure 5.3: Shock pattern evolution obtained through Schlieren visualization for the $\theta_{1N} = 17°$, $\theta_{2N} = 22°$ configuration. The blue markers on the bottom subfigure show the position of each of the Schlieren images on the $M_0 - \theta_2$ plane, where M_{VN} is the von Neumann curve and M_D the Detachment one. The dual solution domain is shown through the shaded area. The dashed line represents the physical path the shock system followed during the experiment. The arrows are added to illustrate the order in which each point is reached.

Figure 5.3(b). At this point, the Mach stem is still too small to be appreciated in the image, but a second slipline can be seen appearing in a darker color than in previous images. The emergence of this second slipline can be considered as a sign of transition from RI to MI. The reason for the change in color of the sliplines is that, due to the creation of the normal shock, the density difference between the flow within the slipline duct and the flow outside it is increased. This change in density creates a sharper gradient, detected by the Schlieren system as a darker line. As M_0 is further decreased and the system moves deeper into the MI domain, the size of the Mach stem increases, which can be clearly seen in Figure 5.3(c). At this point, the convergent-divergent duct formed by the sliplines behind the reflected shocks is distinctly shown. The straight lines that emanate from the triple points slowly become curved as they interact with the expansion fans, forming the familiar convergent-divergent nozzle shape. This effect is consistent with the expected theoretical behavior presented in Section 2.1. The Mach stem reaches its maximum size at the minimum M_0, resulting in the shock pattern shown in Figure 5.3(d). As M_0 is increased again, the opposite process is observed, with the size of the Mach stem slowly decreasing to finally disappear and return to the initial state in Figure 5.3(a). It is important to notice how the shock patterns are identical at every instant and the transition point is detected at the same M_0 value. This can be considered as a first indication of the non-existence of the hysteresis loop within the current experimental setup.

5.2.2 $\theta_{1N} = 17°$, $\theta_{2N} = 10°$ Geometry

Figure 5.4 shows the shock pattern evolution of one of the runs obtained with the Schlieren visualization system for the $\theta_{1N} = 17°, \theta_{2N} = 10°$ configuration. There are two significant differences with the case presented in Section 5.2.1. The first one is that, as it can be seen in the bottom subfigure, the dual solution domain for this case can be considered nonexistent. The second is that this geometry represents a highly asymmetric case, with a 7° deflection angle difference between wedges. As in all cases, the experiment was initialized at the maximum possible M_0, resulting in a configuration far into the RI domain and the shock pattern presented in Figure 5.4(a). It can be clearly seen how the incident shocks emanate from the leading edge of the wedges at different ϕ angles due to the large deflection angle difference imposed by them. Due to this, the reflection point is no longer located at the center of the wedge system but slightly lower. The large asymmetry also generates a slipline with an angle far from the horizontal. Another effect of the asymmetry are the different post-shock Mach numbers, generating two different expansion fan angles. This results in each of them impinging on the sliplines at different streamwise positions, creating a highly asymmetric convergent-divergent duct. As M_0 is reduced, the transition point from RI to MI is eventually reached in Figure 5.4(b). As in the previous case, this point is characterized by the appearance of the double slipline that emanates from the interaction point. As M_0 is further decreased, the sliplines separate and generate again the familiar convergent-divergent duct, as seen in Figure 5.4(c). It is important to notice how the sliplines in this case appear in a much lighter color than in the case presented in Section 5.2.1. The reason for this is the considerably lower M_0 values used for this experiment (2.02 vs. 2.66 in the current image). This lower freestream Mach number leads to a weaker normal shock at the Mach stem which, in turn, generates a lower compression. This results in a lower density gradient which, as

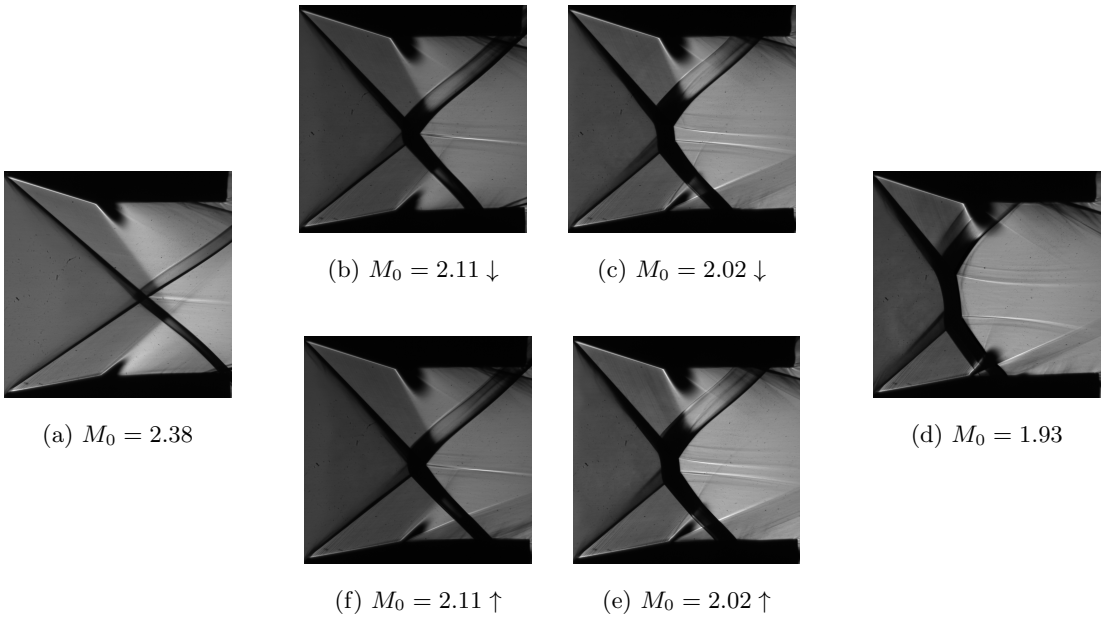

(a) $M_0 = 2.38$ (b) $M_0 = 2.11 \downarrow$ (c) $M_0 = 2.02 \downarrow$ (d) $M_0 = 1.93$ (f) $M_0 = 2.11 \uparrow$ (e) $M_0 = 2.02 \uparrow$

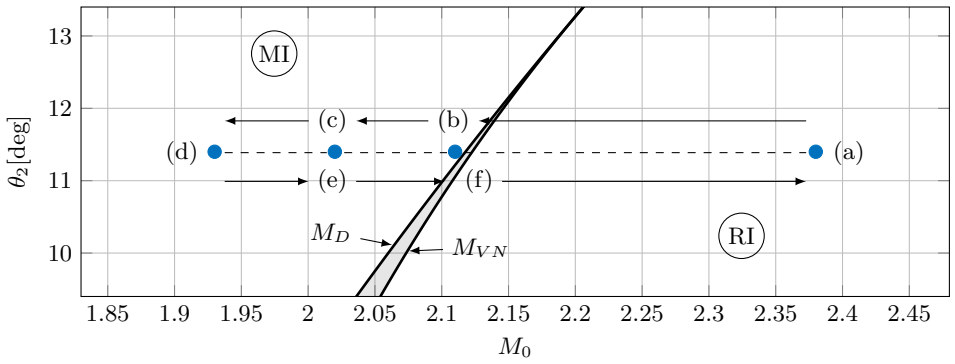

Figure 5.4: Shock pattern evolution obtained through Conventional Schlieren for the $\theta_{1N} = 17°$, $\theta_{2N} = 10°$ configuration. The blue markers on the bottom subfigure show the position of each of the Schlieren images on the $M_0 - \theta_2$ plane, where M_{VN} is the von Neumann curve and M_D the Detachment one. The dual solution domain is shown through the shaded area. The dashed line represents the physical path the shock system followed during the experiment. The arrows are just added to illustrate the order in which each point is reached.

explained in the previous section, results in a lighter slipline. As M_0 is further decreased, the system follows a similar behavior as the one presented in Section 5.2.1, with the Mach stem height first increasing and then decreasing as the system returns to its original state when M_0 is increased again. As it can be seen in Figures 5.4(a) through 5.4(f), the system follows a perfectly symmetric process with configurations with identical M_0 values yielding practically identical images and shock patterns. In this wedge configuration, this is the expected result due to the absence of any dual solution domain along the path the system follows on the $M_0 - \theta_2$ plane.

5.2.3 Schlieren Visualization Overall Performance

As shown through Figures 5.3 and 5.4, the Schlieren visualization system used for this project is capable of capturing the shock pattern and its characteristic flow features (shocks, sliplines and expansion fans) with great clarity. Because of the high quality of the images it can generate, it is used as the main data source for the quantitative analysis of the shock system presented in Section 5.3.1. This leads to the results presented in Sections 5.3.2 and 5.4. The only disadvantage of the current Schlieren visualization system is that, as shown in Section 5.1.1, the shocks appear considerably thicker than they are in reality due to the 3D effects near the windows. This can be overcome by analyzing only the trailing edge of these shock images. As shown through the Focusing Schlieren results of Section 5.1.1, these features correspond to the 2D shocks present in the center plane of the test section.

5.3 Mach Stem Height Evolution

The Schlieren visualization results can be used to compute the Mach stem height (MSH) for all images. This is done with an automated image processing method fully custom made and implemented in Matlab. Section 5.3.1 is used to give an overview of the code architecture used to process the Schlieren images and obtain the final MSH measurements. Section 5.3 is dedicated to presenting and discussing these results.

5.3.1 MSH Data Processing

In order to extract the MSH information from the Schlieren images, first, a preprocessing routine is implemented to facilitate further processing. Next, the shock angles are computed by combining the processed images and the M_0 measurements. This information is then used to compute the location of the interaction point, both for the RI and MI images. Finally, the MSH is computed. Each of these steps are now be explained in detail.

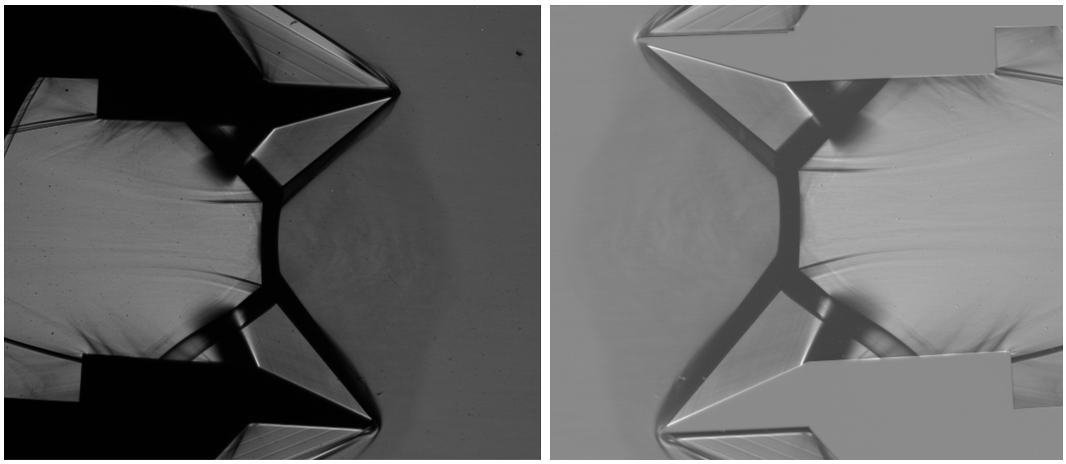

(a) Original image (b) Pre-processed image

Figure 5.5: Comparison of the original and a preprocessed images obtained for a MI configuration of the $\theta_1 = 17°$, $\theta_2 = 22°$ geometry.

Image Preprocessing

Before further processing the images, a preprocessing routine is applied in order to facilitate later phases of the analysis. The main modifications that are made to the raw images are: rotation, cropping and image subtraction. Rotation is done in order to align the images with a horizontal reference line and then simplify the angle measurement later on. Cropping is done in order to reduce the amount of unnecessary data around the image and zoom into the region of interest. Finally, the background is subtracted to the original image in order to reduce background noise and other unwanted effects. This is achieved by subtracting the experiment images from the average of a series of images of the test section recorded before the tunnel is started for the experiment. An example of a resulting image compared to the original is shown in Figure 5.5. As shown, the resulting image shows a smooth background and the shocks show a sharp contrast against it. Despite this, it can be seen how the wedges do not completely disappear from the final image. This could be attributed to the deformations the model endures due to the considerably high loads the flow applies on it, resulting in the wedges not being in the exact same position as before the tunnel starts. Despite this, this error is located near the wedges and does not interfere with any of the upcoming calculations.

Shock and Flow Deflection Angles Computation

The shock angle is computed by detecting the shock lines within every image. To do this, first an interrogation window has to be defined in order to look for the shock line. For the first image, this is done manually but for all subsequent ones, it is placed at a prescribed distance from the interaction point detected in the previous image. This window is placed as close as possible to the interaction point in order to better capture local shock angle oscillations near the interaction point. Once the window is defined, the processor scans each horizontal pixel

line within the window in search for the shock point within each line. As shown in Section 5.1.1, the results of the Focusing Schlieren system show that the shock is always located on the trailing edges of the black lines. This way, if each pixel line is scanned from left to right, the shock point along this line will be located at the point of maximum positive light intensity gradient, due to the sharp change from black to gray at the shock location. Once each line is scanned and the shock point for each of them has been found, a line fitting routine is applied to approximate the shock line contained in the current search window. An iterative method is implemented in order to optimize the R^2 value of the fitted line and reduce the number of outliers. The shock angle is then measured by computing the slope of this fitted line. An example of a search window containing the detected shock points and the line fitted through them is shown in Figure 5.6. As shown in the Figure, despite the relatively small window size used, the line fitting method is capable of capturing a line that matches the shock line near the interaction point.

In order to get a more accurate determination of the flow deflection (θ) near the interaction point, this parameter is calculated in an indirect way. This was achieved by combining the computed shock angles (ϕ) with M_0. This can be done through oblique shock relations by extracting the corresponding deflection angle for the given $M_0 - \phi$ combination:

$$\tan\theta = 2\cot\phi\frac{M_0^2\sin^2\phi - 1}{M_0^2(\gamma + \cos 2\phi) + 2} \tag{5.1}$$

As seen in Equation 5.1, θ can be fully defined through the M_0 value obtained through the pressure measurements (See Section 4.1) and the shock deflection angle computed through the process presented in this section.

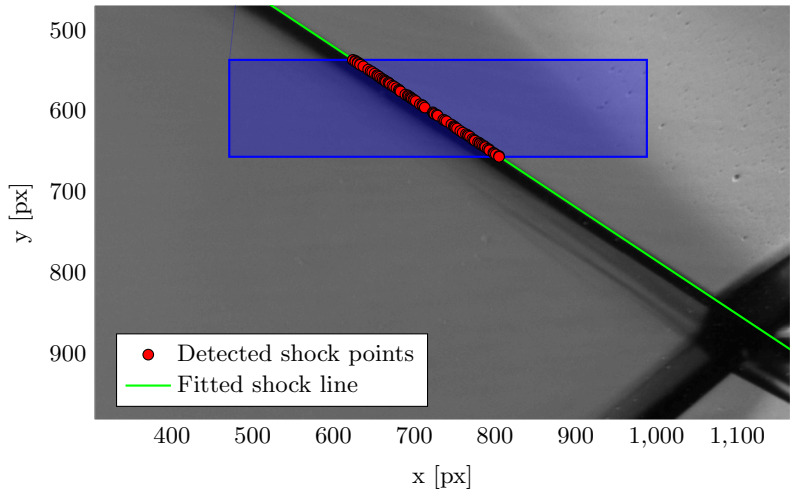

Figure 5.6: Example of a shock line detection for an MI image using the image processor presented in this section. The shaded blue box represents the interrogation window used to find the shock line.

Interaction Point Detection

In order to determine the MSH, the interaction point of every image needs to be defined. In the current analysis, the interaction point is defined as the furthest upstream shock point that can be found along the horizontal line defined by the incident shocks intersection. In an RI, the intersection and interaction point are coincident. In the case of a MI, the intersection point can be found by extending the incident shock lines and computing the intersection of these imaginary lines. The interaction point is located on the Mach stem at the same y position as the intersection point. An example of these two points in a MI can be seen in Figure 5.7(a).

In order to find the interaction point, the shock intersection point needs to be identified first. This is done by computing the intersection point of the two shock lines that are obtained by following the procedure presented in the previous subsection. Once the intersection is found, a horizontal line is established through this point in order to search for the interaction point along it. An example of this search line is shown in Figure 5.7(a). The interaction point is then computed by following a similar procedure used for the shock points (See previous subsection). If the horizontal line is scanned from left to right, the interaction point will be characterized by a sharp positive light intensity gradient, as shown in Figure 5.7(c). It can also be seen that this sharp gradient will always be located near the darkest point of the horizontal, which corresponds to either the Mach stem, in the MI case, or the interaction region, in the RI one, as shown in Figure 5.7(b). For this reason, the search for the interaction point is always started from this point and marching towards the right of the image. Once the gradient exceeds a pre-established threshold the interaction point is found. As it can be seen in 5.7(b), there are noticeable oscillations of the light intensity along the horizontal caused mainly by image noise. In order to reduce the outliers and facilitate the interaction point detection, a median filter was applied to the light intensity profile in order to minimize these oscillations cause by noise while still preserving the sharp gradient regions. A comparison of the filtered and original curves can also be seen in Figure 5.7(b).

MSH Computation

The computation of the actual MSH is done by using the information provided by the shock lines and the interaction point. Two different methods are used. The first one was applied to cases where the Mach stem was relatively vertical, namely the $\theta_{2N} = 22°$, $\theta_{2N} = 21°$, $\theta_{2N} = 19°$ and $\theta_{2N} = 17°$ geometries. The second method is applied to only the final $\theta_{2N} = 10°$ geometry where the Mach stem is highly oblique, due to the large asymmetry of the wedge deflections.

An example of a MSH obtained with the first method is shown in Figure 5.8(a). This method is the simplest of the two as it does not need any additional image information apart from the already computed shock lines and the interaction point location. To obtain the MSH, a vertical line is first drawn through the interaction point. This line will intersect the incident shock lines at two points, P_1 and P_2 in Figure 5.8(a). The MSH can then be approximated as the vertical distance between P_1 and P_2. This method is never perfectly exact, due to the curvature of the Mach stem and the asymmetry of the wedges, but the error introduced by this was found to be negligible in the first four geometries. Due to the high asymmetry of

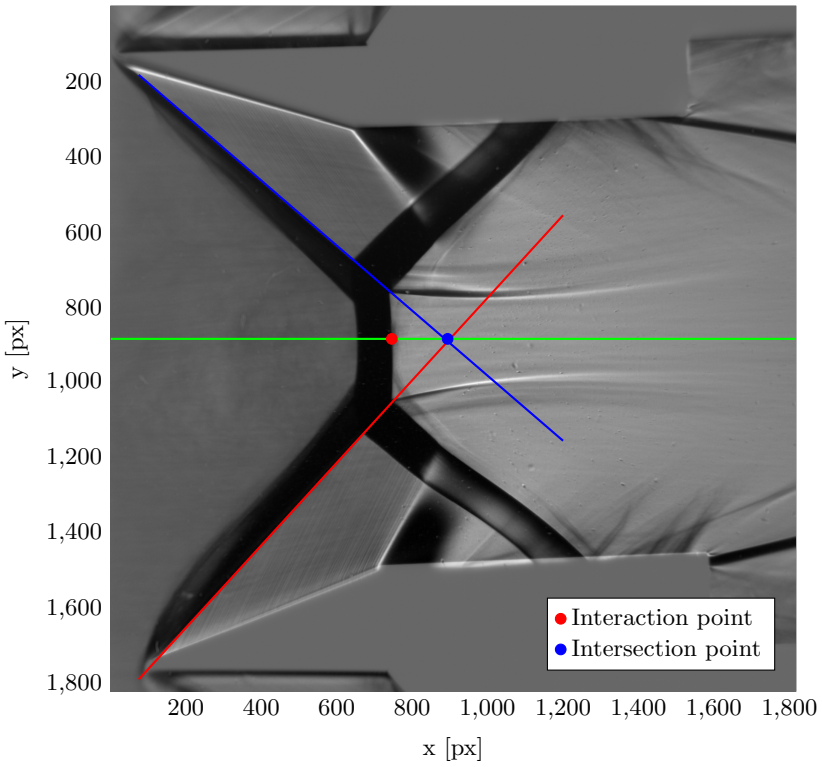

(a) Processed image. Incident shock lines are shown in red and blue, the horizontal search line in green.

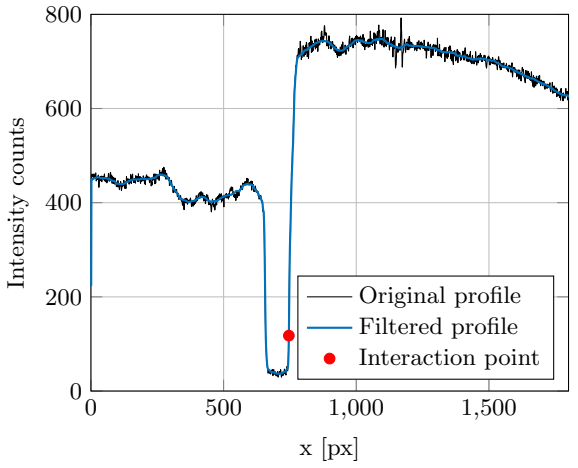

(b) Light intensity profile along the search line.

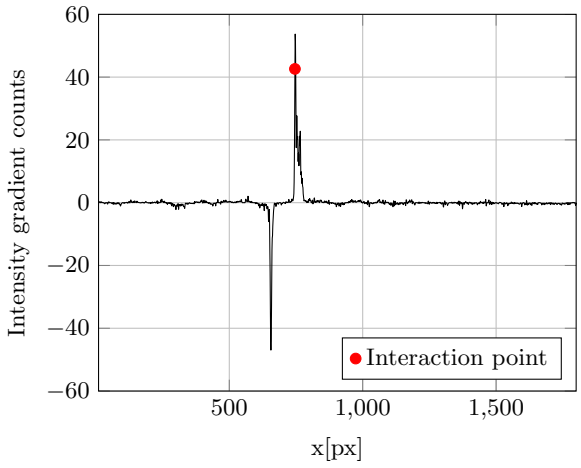

(c) Gradient of the filtered light intensity profile.

Figure 5.7: Example of the interaction point detection of an MI image of the $\theta_{1N} = 17°$, $\theta_{2N} = 17°$ geometry.

the $\theta_{2N} = 10°$ geometry, this error is no longer negligible, specially for large MSH values, so a more sophisticated procedure is needed there.

The second method is more complex and has a higher computational cost than the linear one. The reason for this is that, apart from the shock lines and interaction point, it also needs some information of the actual images. Specifically, it requires the y position of the Mach stem at various locations. An example of an MSH obtained using this method is shown in Figure 5.8(b). This method starts by computing the P_1 and P_2 points in the same way as the first method. In this case, as seen in the Figure, P_1 and P_2 are too far from the Mach stem's vertices, so approximating MSH as the vertical distance between P_1 and P_2 is no longer valid. To overcome this, the X_1 and X_2 points are computed. This is done by first finding the midpoints between I and P_1 and P_2 and drawing horizontal lines through them. X_1 and X_2 are then determined by the intersection between these horizontal lines and the Mach stem. The horizontal position of the Mach stem is found through a gradient search method, similar to the one used to find the shock and interaction points, presented in previous subsections. The final two points, Q_1 and Q_2 are found by intersecting the $I - X_1$ and $I - X_2$ lines with the top and bottom incident shock lines, respectively. The MSH can then be approximated as the vertical distance between Q_1 and Q_2.

Uncertainty Analysis

The data processor presented in this section is designed to generate two main sets of outputs: MSH and both θ angles. Regarding the MSH, it was observed that the measured MSH/w oscillates with an amplitude of roughly $MSH/w = 10^{-2}$ in the RI domain. Here, the MSH should be zero, so $MSH/w = 10^{-2}$ can be approximated as the uncertainty of the MSH computed with the method presented in the current Section.

As previously explained, θ is obtained through Equation 5.1. This relation can be rewritten as:

$$\theta = \arctan\left[2\cot\phi\frac{M_0^2\sin^2\phi - 1}{M_0^2(\gamma + \cos 2\phi) + 2}\right] \rightarrow \theta = f(M_0, \phi) \tag{5.2}$$

Equation 5.2 shows that, if γ is assumed to be known and constant, θ can be considered as the output of a nonlinear function with two variable inputs: M_0 and ϕ. Both of these inputs are determined experimentally, M_0 through the pressure measurements and ϕ through the processing of the Schlieren images, each of them having an experimental uncertainty associated to it. With this, it can be seen that the uncertainty of θ will be a nonlinear combination of the uncertainties of M_0 and ϕ. In order to find this relation, the error of M_0 and ϕ can be propagated by expanding θ through a Taylor expansion. This way, the uncertainty of θ at an arbitrary point i can be approximated as:

$$\Delta\theta_i \approx \left|\frac{\partial\theta}{\partial M_0}\right|_i |\Delta M_0| + \left|\frac{\partial\theta}{\partial\phi}\right|_i |\Delta\phi| \tag{5.3}$$

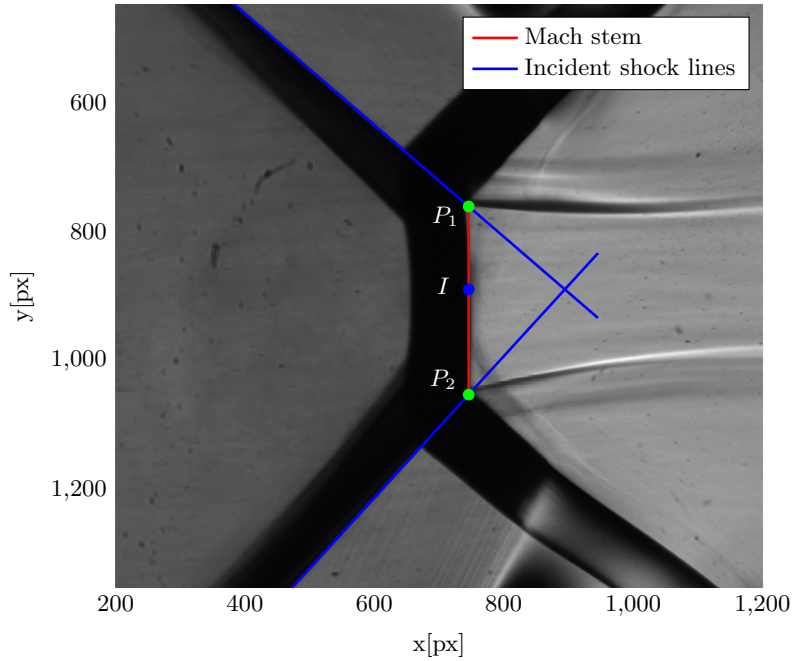

(a) Method 1

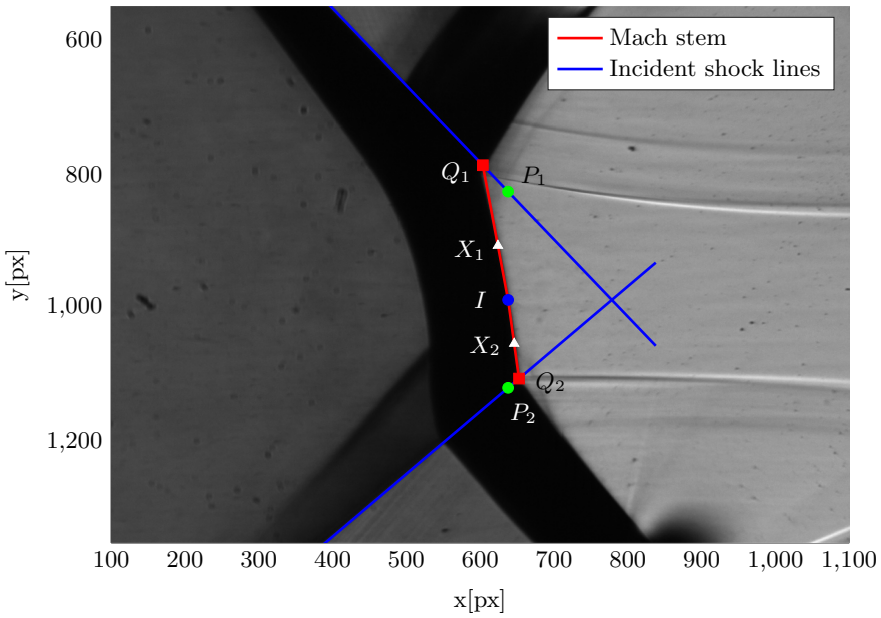

(b) Method 2

Figure 5.8: Illustration of the two methods used to compute the MSH. (a) corresponds to the $\theta_{1N} = 17^{\circ}$, $\theta_{2N} = 17^{\circ}$ geometry, where the Mach stem is vertical, and (b) to the $\theta_{1N} = 17^{\circ}$, $\theta_{2N} = 10^{\circ}$ geometry, where it is highly oblique due to the large asymmetry between deflection angles.

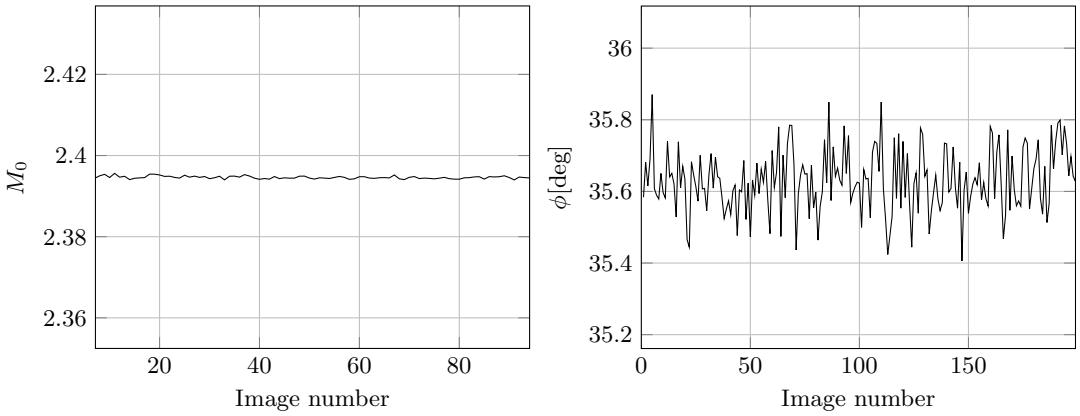

(a) M_0 oscillations

(b) ϕ oscillations

Figure 5.9: Example of the oscillations observed at the initial stage of the experiments, where M_0 is still static.

Where Δ represents the uncertainty of each variable. ΔM_0 and $\Delta\phi$ are assumed to be constant throughout each run. The partial derivatives can be obtained analytically by differentiating Equation 5.2 respect to M_0 and ϕ:

$$\frac{\partial\theta}{\partial M_0} = \frac{4(\gamma+1)M_0\cot(\phi)}{(\gamma^2+1)M_0^4 + 2\gamma M_0^4\cos(2\phi) + 4(\gamma-1)M_0^2 + 4\csc^2\phi} \tag{5.4}$$

$$\frac{\partial\theta}{\partial\phi} = \frac{4[\gamma M_0^4\cos(2\phi) + ((\gamma+1)M_0^2+2)\csc^2\phi + M_0^4 - 4M_0^2]}{2(\gamma^2+1)M_0^4 + 4\gamma M_0^4\cos(2\phi) + 8(\gamma-1)M_0^2 + 8\csc^2(\phi)} \tag{5.5}$$

Where csc is the inverse sine function. Equations 5.3, 5.4 and 5.5 allow the estimation of the uncertainty of θ at every instant of every run by using the corresponding values of M_0 and ϕ at each instant. In addition to this, the values of ΔM_0 and $\Delta\phi$ must be estimated. In order to approximate these parameters, the portion of the experiments where the tunnel has started but M_0 has not been varied yet is observed. An example of the behavior of M_0 and ϕ in this region is shown in Figure 5.9. As it can be seen, both magnitudes oscillate around an average nominal value. ΔM_0 and $\Delta\phi$ is approximated as the standard deviation of these oscillations in this region of the experiments.

In order to compute the final error of $\Delta\theta$, the parameters ΔM_0 and $\Delta\phi$ are computed for each run and are assumed to be constant through it. With this, the computed ΔM_0 and $\Delta\phi$ and the measured instantaneous M_0 and ϕ are used in Equations 5.3, 5.4 and 5.5 to compute $\Delta\theta$ at every instant of each run. The final uncertainty for each test is approximated as the average $\Delta\theta$ for that experimental run and the uncertainty of each geometry as the average $\Delta\theta$ of all five runs. The resulting uncertainties are presented in table 5.1. The full results containing all uncertainties for all runs can be found in Appendix C.

Table 5.1: Estimated average uncertainty for the measured M_0 and computed ϕ and θ angles for all geometries. The average is computed over the five runs of each geometry.

Geometry		**Uncertainty**				
θ_{1N}	θ_{2N}	ΔM_0	$\Delta\phi_1$	$\Delta\phi_2$	$\Delta\theta_1$	$\Delta\theta_2$
17.0°	22.0°	$7 \cdot 10^{-4}$	0.2°	0.1°	0.2°	0.1°
17.0°	21.0°	$5 \cdot 10^{-4}$	0.2°	0.1°	0.2°	0.1°
17.0°	19.0°	$8 \cdot 10^{-4}$	0.4°	0.2°	0.4°	0.1°
17.0°	17.0°	$6 \cdot 10^{-4}$	0.4°	0.2°	0.3°	0.1°
17.0°	10.0°	$5 \cdot 10^{-4}$	0.2°	0.1°	0.2°	0.1°

As seen in the table, the relative uncertainty of M_0 is about 2 orders of magnitude lower than the one of ϕ (M_0 is in the order of 10^0 while ϕ is in the order of $10^{1\circ}$ for most runs). This leads to the conclusion that the uncertainty of M_0 can be considered negligible against the one of ϕ. This is reflected on $\Delta\theta$, which is almost identical to $\Delta\phi$ for most geometries, with ΔM_0 having almost no influence on it. This indicates that almost all of the error of the final MSH and θ results will be dominated by the error of ϕ. This uncertainty has two sources. The first one originates from the image processing method used to obtain ϕ. As explained in the previous subsections, ϕ is obtained through a line fitting routine applied to the Schlieren images. This procedure introduces some uncertainty that depends on the method and fitting threshold used and the quality of the original images. The second source of uncertainties in ϕ are the physical oscillations of the shock waves during the experiments. After inspecting the videos of the experiments, it can be clearly seen that the shock angles oscillate in a noticeable way, indicating that part of the oscillations seen in Figure 5.9(b) have a physical origin and are not generated exclusively by uncertainties in the measurement. With the available data and the method used to obtain ϕ it is not possible to decouple the physical oscillations from the measurement error of ϕ.

5.3.2 Mach Stem Height Results

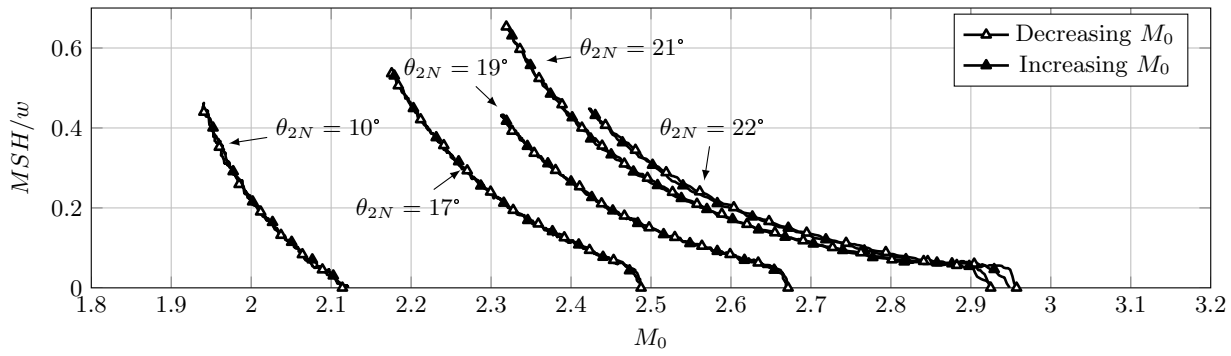

Figure 5.10: Evolution of the normalized MSH with M_0 for all geometries.

The recorded evolution of the MSH, normalized with the wedge hypotenuse (w), is shown in Figure 5.10. The MSH evolution was computed for all runs within each geometry following the procedure presented in Section 5.3.1. It was found that the variation of these curves between runs was minimal. For this reason and for the sake of clarity, only one run per geometry is shown in Figure 5.10. Similar plots for all other runs are presented in Appendix D.

These MSH curves confirm the expected behavior of a shock system with a variable M_0. In the current experiments, the system always starts at its maximum M_0, in the RI domain. In this region, the MSH is always zero until M_0 becomes low enough for the system to transition to MI. At this point, the MSH changes from zero to a finite value. As M_0 keeps decreasing, MSH/w increases in a nonlinear way, as seen in all five curves, until it reaches its maximum value at the corresponding minimum M_0 for each run. It can also be seen that the growth rate of MSH/w with M_0 grows as θ_{2N} is decreased. This means that for lower θ_{2N} geometries, MSH changes faster with M_0. An important feature to notice in Figure 5.10 is how there is an almost perfect overlap of the MSH/w curves for increasing and decreasing M_0. As explained in Section 3.4, the ratio of dM_0/dt to the characteristic time scale scale of the problem, computed as $\frac{dM_0/dt}{u_\infty/w}$ is in the order of 10^{-5}. This indicates that the rate of change of M_0 is negligible compared to the time scales of the flow. Under these conditions, the experiments performed can be analyzed under the assumption of quasi-steady freestream flow. This way, although M_0 is varying in time, each snapshot of the flow can be assumed to be representing a steady state. Under these steady state conditions, the size of the MSH at a given M_0 is determined by θ_1, θ_2 and $2g/w$ (Mouton and Hornung, 2007). θ_1, θ_2 and $2g/w$ were kept constant within each run, so the only possible range in which the MSH could take different values depending on if M_0 is increasing or decreasing is the dual solution domain. If a hysteresis loop exists, a different MSH curve would be observed for increasing and decreasing M_0 in this region. Because all of the MSH curves show a clear overlap in all geometries, it can be concluded that a hysteresis loop was not detected in the present study. This confirms the observations presented in Section 5.2. As presented in Section 2.1.3, steady inviscid Gas Dynamics theory predicts the existence of a hysteresis loop. The absence of it could indicate that the quasi-steady assumption may not be entirely valid for the current setup. Although the general freestream conditions can be considered quasi-steady, this assumption may not hold at a local flow level. As it is discussed in Section 5.4, the premature transition from RI to MI observed in the current study could be caused by local unsteady perturbations near the interaction point.

Two different types of MSH evolution curves can be seen near the transition points. In the case of the $\theta_{2N} = 17°, 19°, 21°$ and $22°$ geometries, it is clear that once the M_0 reaches the transition point, the MSH rapidly changes from zero to a finite value and then follows a smooth trend all the way to the maximum MSH value and back. In the case of the $\theta_{2N} = 10°$ geometry the transition happens in a smooth way, with the MSH evolving without any sharp jumps near the transition point. It seems from these results that the stable MSH at transition has a finite value for the first four geometries. On the other hand, it seems that the stable MSH at transition for the $\theta_{2N} = 10°$ is negligible or too small to be detected, which would explain the smooth trend observed within the $\theta_{2N} = 10°$ geometry.

As explained in Section 2.1, the Mach Stem size cannot be analytically computed in an exact way. For this reason, any experimental data that can give any information about the evolution of this flow feature can be very useful for model validations. In most previous studies, the MSH computation was done by visual inspection of the Schlieren images, introducing this way a significant error in the results. In the current study, the MSH was computed in a more robust and reliable way by automating the Schlieren image processing through the procedure presented in Section 5.3.1. This feature makes the curves presented in Figure 5.10 and Appendix D a very useful tool to better understand the MSH evolution phenomenon and validate models built to predict the behavior of this flow feature.

5.4 Transition and Hysteresis

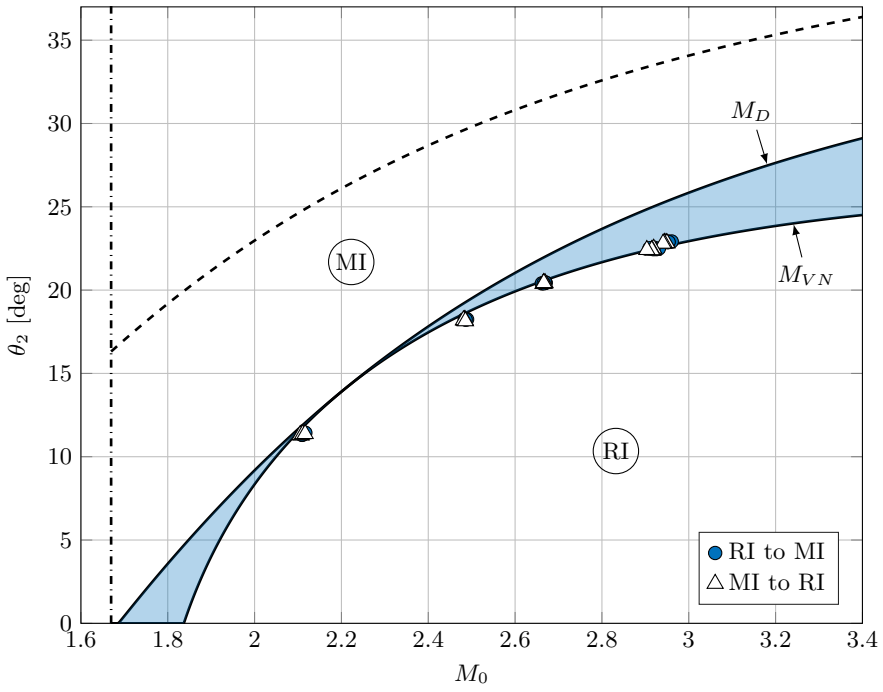

Figure 5.11: $M_0 - \theta_2$ plane for the average $\theta_{1T} = 16.3°$ together with the detected transition points of all runs. The dual solution domain is shown through the shaded area and the θ_2 and θ_1 attached shock boundaries through the dashed and dash-dotted lines, respectively.

The transition point for each run is determined through the MSH evolution measurements presented in Section 5.3. A shock interaction is assumed to have transitioned from RI to MI when the MSH exceeds a minimum threshold. A transition from MI to RI is assumed to happen in the opposite scenario when the MSH reaches a value below the previously established threshold. This threshold value is set at $MSH/w = 10^{-2}$ which, as explained in Section 5.3.1, is the expected uncertainty of MSH/w computed through the method presented in the same Section. Applying this criterion, the transition Schlieren image for each run can be obtained. The M_0 value at transition (M_{0T}) can then be determined by linking these Schlieren transition images to the corresponding M_0 at that given instant. The uncertainty

of M_0 is presented in Table 5.1. As it can be seen, it is in the order of 10^{-4} for all geometries, which, as discussed in Section 5.3.1, can be considered negligible compared to the uncertainty introduced by θ and ϕ. The remaining parameters needed to completely characterize the transition points are θ_1 and θ_2 at transition (θ_{1T} and θ_{2T}). During the experiments and the processing of the results it was found that there is a non-negligible deviation of the actual deflection angles from the nominal ones for which the experiments are designed. This deviation is attributed to wedge deformations caused by the large loads applied on the model and boundary layer development over the surface of the wedges. To account for this, θ_{1T} and θ_{2T} are determined in an indirect way, through the procedure presented in Section 5.3.1. The estimated uncertainty for these two parameters for all five geometries is shown in Table 5.1. As previously explained, the uncertainty of these two angles is considerably larger than the one for M_0. For this reason, it is expected that the uncertainty of the transition points will be dominated by the uncertainty in θ_1 and θ_2. The transition points are determined for all runs performed during the experimental campaign. The results obtained are presented on the $M_0 - \theta_2$ plane in Figure 5.11. In this plot, the von Neumann and Detachment lines are computed by using the average $\theta_{1T} = 16.3°$ computed over all runs and geometries. The transition points averaged over the five runs for each geometry are shown in Table 5.2. The exact transition points for all individual runs and geometries can be found in Appendix E.

Table 5.2: Transition values obtained for all geometries. Each θ_{1T}, θ_{2T} and M_{0T} value is computed as the average of the five runs completed for each geometry.

		RI to MI			**MI to RI**		
θ_{1N}	θ_{2N}	θ_{1T}	θ_{2T}	M_{0T}	θ_{1T}	θ_{2T}	M_{0T}
17.0°	22.0°	16.0°	22.9°	2.95°	15.9°	22.8°	2.95°
17.0°	21.0°	16.0°	22.5°	2.92°	15.9°	22.4°	2.92°
17.0°	19.0°	16.4°	20.4°	2.67°	16.3°	20.4°	2.67°
17.0°	17.0°	16.5°	18.3°	2.49°	16.4°	18.2°	2.48°
17.0°	10.0°	16.9°	11.4°	2.11°	16.9°	11.3°	2.11°

A noteworthy feature in Figure 5.11 is the excellent repeatability of the results, which can be seen through the almost perfect overlap of the transition points detected at different runs within each geometry. At the same time, it can be noticed how the RI to MI and MI to RI points also match almost exactly within every run. This is another clear indication that no hysteresis effects were present in the current experiments, which is consistent with the MSH evolution results discussed in Section 5.3 and the Schlieren images from Section 5.2.1. It can also be seen very clearly how all of the transition points lie almost exactly on the von Neumann line. In the $\theta_{2N} = 10°$ case, the von Neumann condition transition is expected. As explained in Section 3.4, the current experiment can be studied from a quasi-steady freestream point of view. Under these circumstances, and given the absence of any dual solution domain for $\theta_{2N} = 10°$, there is only one possible transition point, which is at the von Neumann condition. The excellent agreement with this theoretical prediction and the measured result is a convincing validation of the transition detection method used to obtain the present results. For the rest of the geometries ($\theta_{2N} = 17°, 19°$, 21° and 22°), according to inviscid Gas Dynamics theory, if a perfect uniform flow is assumed, a transition at the Detachment line for the RI to MI cases and at the von Neumann line for the MI to RI, as

reported in Ivanov et al. (2003b), would be expected. As shown in Figure 5.11, this is not the case, with all the transition points lying on the von Neumann line and no hysteresis loop detected.

The reason for the von Neumann transition is suspected to be the non-uniformities and noise present in the flow. The wind tunnel used, unlike the one in Ivanov et al. (2003b), cannot be considered a low-noise facility (Giepman et al., 2015). There are previous studies, such as Henderson and Lozzi (1975) or Hornung and Robinson (1982b), where transition was also always detected at the von Neumann condition. Other studies, such as Sudani et al. (2002) indicate that small freestream perturbations can play a crucial role on the premature transition from RI to MI. In light of the present results, it is likely that the perturbations and noise generated by the TST-27 wind tunnel are high enough to trigger a premature transition from RI to MI resulting in a transition on the von Neumann line in both directions. As explained in Section 2.2.3 the physical mechanism that allows flow perturbations to trigger early transition is still not understood. In order for a perturbation to be able to trigger transition, it must be capable of moving the shock system from a region with a stable RI to one where an MI can prevail. If inviscid Gas Dynamics theory is applied, transition between RI and MI depends on four parameters: γ, θ_1, θ_2 and M_0. By following this reasoning, it can be inferred that perturbations that are capable of triggering transition must modify one of these parameters in order to destabilize the RI system. The fundamental properties of the air used remain relatively unchanged during all experiments, so no oscillations in γ should be expected. On the other hand, the M_0 and ϕ profiles recorded during the experiments seem to show significant oscillations in these parameters, as shown in Figure 5.9, which could contribute to the von Neumann condition transition. On the other hand, in Sudani et al. (2002), it was found that freestream disturbances alone, such as fluctuations in pressure, were not enough to trigger early transition from RI to MI and that some unknown irregular, local perturbation is necessary for it. This way, it could also be speculated that other type of perturbations are needed, such as local high frequency M_0 oscillations or sharp changes in ϕ near the interaction point. This local M_0 could also be affected by high frequency oscillations in ϕ which could significantly change M_0 in the shock frame of reference. These hypothetical changes in the relative M_0 could displace the shock system from a stable RI region to one where an MI is the stable solution. This would mean that the quasi-steady flow assumption may not be valid for shock-shock interaction experiments in a non-uniform flow due to the possible existence of local unsteady oscillations. In order to study these dynamic oscillations, the local shock and M_0 oscillation frequencies are needed. In the experiments presented in this study, Schlieren images were all recorded at a maximum frequency of 100 Hz, so high frequency oscillations cannot be time resolved. At the same time, M_0 was determined by pressure measurements in the settling chamber and the test section walls, yielding only freestream values and no local information regarding the changes in M_0. Further experiments are needed in order to characterize these local perturbations and fully understand the physical mechanism responsible for premature RI to MI transitions.

Chapter 6

Conclusions and Recommendations

6.1 Conclusions

An experimental study on shock-shock interactions has been performed with the aim of analyzing the effect of a variable inflow Mach number on the evolution of the Mach stem and transition between Regular (RI) and Mach (MI) interactions. An aerodynamic model consisting of two opposing wedges of equal hypotenuse length was designed and tested in the TST-27 transonic-supersonic wind tunnel at TU Delft. The upper deflection angle was kept at $\theta_1 = 17°$ throughout the runs. On the other hand, five different bottom deflection angles of $\theta_2 = 10°$, $17°$, $19°$, $21°$ and $22°$ were investigated. The freestream Mach number (M_0) ranged from 1.8 to 3.2, depending on the geometry. For every run, the system was initialized in the RI domain, M_0 was then decreased until achieving a transition to MI, and finally increased again until the RI was recovered. The two flow visualization techniques used were Schlieren visualization and Focusing Schlieren.

The Focusing Schlieren system was built and implemented during the course of the current project, as it had never been used before in the experimental facilities used. By blurring out-of-focus elements from the test section center plane image, the system allowed a clear observation of the shock pattern. It also revealed a boundary layer detachment at the sidewalls, caused by the negative pressure gradient imposed by the incident shocks, as the main source of three-dimensional effects within the setup. Focusing Schlieren visualization also showed an almost constant Mach stem size throughout the test section, resulting in a MI covering the whole span of the model. This contrasts with previous literature, such as Ivanov et al. (2001b) or Sudani et al. (2002), where cases of a coexisting RI and MI in the spanwise direction were observed.

The Schlieren visualization system was able to sharply capture the shock system and its main flow features, namely the incident and reflected shocks, the sliplines and the expansion fans, at every instant of the runs. In all cases, for a given inflow Mach number and regardless of

the existence of a dual solution domain region, the system showed identical shock patterns no matter if M_0 was increasing or decreasing. This is an indication that no hysteresis loop could be observed in the setup used in the current project. The Schlieren visualization results were used as the data source for the quantitative analysis performed on the transition process.

A custom-made image processing system was built to compute the Mach Stem Height evolution with M_0 for every run. It was found that, within each geometry, the Mach stem height displayed identical values at each M_0 point for both increasing and decreasing Mach numbers. This confirmed the absence of the hysteresis loop already detected in the Schlieren images. At the same time, it was observed that the rate of change of the MSH with M_0 increased as θ_2 decreased. It was also seen that, for geometries of the current setup that contained a dual solution domain region, the MSH had a finite value at transition, with a sharp jump in the MSH profile at this point. This behavior was not observed in the $\theta_2 = 10°$ run, which contained no dual solution domain. The transition results showed a very good experimental repeatability with all transition points for a given geometry detected at the von Neumann condition. Inviscid Gas Dynamics theory predicts a transition from RI to MI at the Detachment condition and MI to RI at the von Neumann condition. In Ivanov et al. (2001a), it was numerically proven that, under the condition of a perfect, uniform freestream flow, inviscid Gas Dynamics theory can perfectly predict the transition points for a variable inflow Mach number. Through the current project it was shown that this model can fail when flow non-uniformities exist. A satisfactory agreement of analytical shock polar theory was found for MI to RI transition, but a more elaborate model is needed in order to predict MI to RI transition. This agrees with previous studies, such as Sudani et al. (2002), where RI to MI transition was also detected at the von Neumann line instead of the Detachment one.

Almost all previous investigations have been performed under the condition of variable deflection angles. Durand et al. (2003) is the only previous experimental study with a variable inflow Mach number. In that study, it was found that no hysteresis loop existed, with RI to MI and MI to RI transition points overlapping in all runs. In Sudani et al. (2002) and Sudani et al. (2003), among others, it was already shown that the hysteresis loop could be suppressed through flow perturbations when the deflection angles are variable. The current study, combined with the conclusions in Durand et al. (2003), confirms that this is also true for the case of a variable M_0. These results, in combination with previous literature, clearly show that flow perturbations play a crucial role in the transition of RI to MI, up to the point where they can be capable of impeding any penetration of the RI into the dual solution domain.

Over the last decades, many experimental studies have been completed on the topic of shock-shock interactions. Despite this, in order to fully solve the shock-shock interaction problem, the role of freestream perturbations on the transition from RI to MI and the physical mechanism behind it need to be fully understood. Due to the sensitivity of the RI to these oscillations, the results of any experiment performed on this topic will always be highly dependent on the characteristics of the wind tunnel used and the perturbations generated by it. The only previous study that was capable of investigating the shock-shock interaction phenomenon in an almost uniform flow was Ivanov et al. (2003a). All other experiments in the literature, including the present one, contained some level of noise in the freestream flow. In order to fully understand the effect of these perturbations on the transition process, the

turbulence level of the freestream flow needs to be controlled. Due to the complexity of any supersonic wind tunnel, this is not usually possible. This issue can be solved through CFD simulations where the turbulence level can be controlled by adjusting the boundary conditions accordingly. This way, future experimental studies should be complemented with CFD simulations in order to understand the effect of these perturbations on the shock system.

6.2 Recommendations for Future Work

The current section is dedicated to presenting some ideas on how the research performed through the current study could be expanded and some improvements that can be made to the current setup. All these ideas originate from the experience and lessons learned during the course of this project.

6.2.1 Focusing Schlieren

As explained in Section 4.3, the Focusing Schlieren setup used in the present project is the first visualization system of this type implemented in the High Speed Aerodynamics laboratory at TU Delft. Although the performance of the system was satisfactory, the system can be considered to still be in an early stage of development, which leaves a lot of room for improvement and optimization. Some ideas to achieve this are presented here.

An important part of any Focusing Schlieren setup is the segment containing the light source, Fresnel lens and source grid. In order to improve the quality of the final image, the background lighting has to be as uniform as possible, which depends on the light source and the Fresnel lens. The light source should not be a point source but an extended light source. In the case of the current experiment, this was done by opening the source diaphragm to its maximum size and placing translucent tape on it to make it as disperse as possible. Despite this, in some configurations the background was still not fully uniform with a noticeable light concentration in the center of the image. This could be improved by increasing the size of the light source by replacing it by an LED array, for example.

The Fresnel lens, does not only play a role in the uniformity of the background but it is also an important optic element that is in charge of creating the convergent light beam. The size of the field of view, as seen in Equation 4.2 is directly related to the size of the source grid and thus the Fresnel lens, so it should always be chosen with this parameter in mind. In the current project, due to time constraints, the system was built with a lens that was readily available in the lab. In order to optimize the system, a new and better Fresnel lens should be chosen with the highest possible quality and a size big enough for the required FOV. Increasing the quality of the lens would increase the uniformity of the light beam, improving the final images and creating a more uniform background.

The source and cutoff grids used in the present project were manufactured by printing them on transparent slide paper. This method can be accurate and reliable enough but it is not

practical. It takes a lot of time and effort to ensure that they are perfectly parallel and the right size. This can be alleviated by testing different manufacturing methods, such as 3D printing or laser cutting, which could also increase the robustness of the system. Additionally, the source grid was placed directly on the Fresnel lens and the support used for both was very fragile and unreliable. In order to optimize this segment of the setup, a system that allows the source grid to be placed without touching the Fresnel lens and at a small distance ahead of it is needed. At the same time, this system should be rigid and precise enough to facilitate assembly.

Among all components, the systems appears to be most sensitive to the focusing lens. First, the optic performance of this element has an important influence on the quality of the final image. Secondly, as seen in Figures 4.5 and 4.6, its aperture has a direct effect on the FOV and depth of focus of the setup. These two parameters are directly improved by increasing the aperture of this lens. In order to optimize the size of the FOV and reduce the depth of focus, a focusing lens with the largest possible aperture should be used. The camera used in the current project was good enough for the task at hand, leaving little room for improvement. The main downside it had was its relatively low maximum acquisition frequency of about 50 Hz. In possible future studies with the aim of studying flow perturbations and their role in transition (See Section 6.2.3), a camera with a higher acquisition frequency will probably be required.

6.2.2 Model Geometry

As explained in Chapter 3, the aerodynamic model used in the current project was designed with the aim of keeping $2g/w$ constant. As reported in Mouton and Hornung (2007), this parameter seems to have an influence on the size of the Mach stem and could affect the transition point. For this reason, it would be interesting to experimentally study the influence of this parameter by testing models with different $2g/w$ values. There are many challenges that would have to be addressed in order to design these new models. Most of them can be solved by following the guidelines presented in Section 3.3. The most difficult one would probably be solving the startup problem. As seen in Equation 3.11, $2g/w$ has an important influence on the critical area of the model. Special care must be put into choosing the correct deflection angles and startup Mach number in order for the wind tunnel to adequately start. If this becomes a challenge, the problem could be solved by either increasing the startup Mach number or the total pressure. The first solution increases the Mach number after the startup normal shock, reducing the minimum throat size the tunnel can start with. The second one increases the pressure after the startup shocks, helping the system overcome the back pressure at the tunnel diffuser.

6.2.3 Flow Perturbations

As extensively reported in the literature and in the conclusions of the current project, flow perturbations seem to play a major role in the transition between RI and MI. For this reason a

good understanding of these flow features is necessary in order to fully characterize transition. With the data obtained during this project, this is not possible and additional experiments are needed in order to characterize these fluctuations and their impact on the shock system.

The Schlieren and Focusing Schlieren systems can only detect the effect of the perturbations on the shock waves. In order to study the oscillations themselves, a different flow visualization technique is needed. One of them could be Particle Image Velocimetry (PIV). This flow measurement technique allows the observation of the velocity field within the test section. This way it could be used to resolve the flow perturbations in the freestream and the regions near the shocks. In order to achieve this, the acquisition frequency of the system must be high enough to resolve the high frequency oscillations. At the same time the size of the interrogation windows must be small enough in order to have a spatial resolution good enough to observe these oscillations. This could also be achieved through hot wire anemometry, which could potentially allow higher acquisition frequencies. Once the freestream oscillations are characterized, this information can be used to set a consistent inflow condition for a numerical investigation. This could potentially result in a flow study with a higher spatial and temporal resolution.

6.2.4 Mach Stem Modeling

One of the elements of a shock-shock interaction that still cannot be accurately modeled through analytical methods is the the Mach stem height. For this reason, experimental measurements of this feature are highly valuable for Mach stem model validation. As presented in Section 5.3.2, very precise and extensive MSH measurements were obtained in the current project. It would be really interesting to use this data for analytical or semi-analytical model validation. As seen in Figure 5.1 and Appendix B, the Focusing Schlieren system is capable of visualizing the Mach stem and the sliplines very clearly by blurring out three-dimensional effects that contaminate Schlieren images. In the current project, the image processing code was only applied to the Schlieren visualization images. It would also be interesting to adapt the code so it can also process Focusing Schlieren images and study the MSH evolution with this visualization technique. Finally, it would also be a good idea to validate the Mach stem size and growth rate obtained through CFD simulations.

Bibliography

J. Anderson Jr. *Fundamentals of aerodynamics*. McGraw Hill, 2001.

G. Ben-Dor. *Shock wave reflection phenomena*, chapter 1. Springer-Verlag, 1992.

C.J. Chapman. *High speed flow*, chapter 11. Cambridge University Press, 2000.

A. Chpoun, D. Passerel, H. Li, and G. Ben-Dor. Reconsideration of oblique shock wave reflections in steady flows. Part 1. Experimental investigation. *Journal of Fluid Mechanics*, 301:19–35, 1995.

A. Durand, B. Chanetz, R. Benay, and A. Chpoun. Investigation of shock waves interference and associated hysteresis effect at variable-Mach-number upstream flow. *Shock Waves*, 12: 469–477, 2003.

D. Floryan, J. Hofferth, and W. Saric. Design, assembly and calibration of a Focusing Schlieren system. *Technical Report, Texas A&M University*, 2012.

V.M. Fomin, H.G. Hornung, M.S. Ivanov, A.M. Kharitonov, and G.P. Klemenkov. The study of transition between regular and Mach reflection of shock waves in different wind tunnels. *Skews BW (ed) Book of Abstracts, 12th Int Mach Reflection Symp, South Africa*, 1996.

R.H.M. Giepman, F.F.J. Schrijer, and B.W. van Oudheusden. High-resolution PIV measurements of a transitional shock wave-boundary layer interaction. *Experiments in Fluids*, 56 (113), 2015.

Z. Han and X. Yin. *Shock dynamics*. Kluwer, 1993.

L.F. Henderson and A. Lozzi. Experiments on transition of Mach reflexion. *Journal of Fluid Mechanics*, 68(1):139–155, 1975.

H. G. Hornung and M.L. Robinson. Transition from regular to Mach reflection of shock waves part 2. The steady-flow criterion. *Journal of Fluid Mechanics*, 123:155–164, 1982a.

H.G. Hornung. On the stability of steady–flow regular and Mach reflection. *Shock Waves*, 7: 123–125, 1996.

H.G. Hornung and M.L. Robinson. Transition from regular to Mach reflection of shock waves. Part 2. The steady-flow criterion. *Journal of Fluid Machanics*, 123:155–164, 1982b.

H.G. Hornung, H. Oertel, and R.J. Sandeman. Transition to Mach reflexion of shock waves in steady and pseudosteady flow with and without relaxation. *Journal of Fluid Mechanics*, 90:541–560, 1979.

M.S. Ivanov, S.F. Gimelshein, and A.E. Beylich. Hysteresis effect in stationary reflection of shock waves. *Physics of Fluids*, 7(4):685–687, 1995.

M.S. Ivanov, G. Ben-Dor, T. Elperin, A.N. Kudryavstev, and D.V. Khotyanovsky. Flow Mach number variation induced hysteresis in steady shock wave reflections. *AIAA Journal, Technical Notes*, 39(5), 2001a.

M.S. Ivanov, D. Vandromme, V.M. Fomin, A.N. Kudryavstev, A. Hadjadj, and D.V. Khotyanovsky. Transition between regular and Mach reflection of shock waves: new numerical and experimental results. *Shock Waves*, 11:199–207, 2001b.

M.S. Ivanov, A.N. Kudryavstev, S.B. Nikiforov, A.A. Pavlov, and A.N. Shiplyuk. Study of transition between regular and Mach reflections in various wind tunnels. *41st Aerospace Sciences Meeting and Exhibit, Reno, Nevada*, 2003a.

M.S. Ivanov, A.N. Kudryavtsev, S.B. Nikiforov, D.V. Khotyanovsky, and A.A. Pavlov. Experiments on shock wave reflection transition and hysteresis in low-noise wind tunnel. *Physics of Fluids*, 15(6):1807–1810, 2003b.

R. Kawamura and H. Saito. Reflection of shock waves - 1, pseudo-stationary case. *Journal of the Physics Society of Japan*, 11:584–592, 1956.

H. Li, A. Chpoun, and G. Ben-Dor. Analytical and experimental investigations of the reflection of asymmetric shock waves in steady flow. *Journal of Fluid Mechanics*, 390:25–43, 1999.

E. Mach. Uber den verlauf von funkenwellen in der ebene und im raume. *Sitzungsbr. Akad. Wiss. Wien*, 78:818–838, 1828.

C.A. Mouton. Transition between regular reflection and Mach reflection in the dual-solution domain. *Doctoral Thesis, California Institute of Technology, Pasadena*, 2007.

C.A. Mouton and H.G. Hornung. Mach stem height and growth rate predictions. *AIAA Journal*, 45(8):1977–1987, 2007.

A. Pope and L.G. Kennith. *High-speed wind tunnel testing.* John Wiley & Sons, Inc., 1965.

F.F.J. Schrijer. Experimental investigation of re-entry aerodynamic phenomena. *Doctoral thesis, Delft University of Technology*, 2010.

G.S. Settles. *Schlieren and shadowgraph techniques: visualizing phenomena in transparent media.* Springer-Verlag Berlin Heidelberg, 2001.

B.W. Skews. Aspect ratio effects in wind tunnel studies of shock wave reflection transition. *Shock Waves*, 7:373–383, 1997.

N. Sudani, M. Sato, M. Watanabe, J. Noda, A. Tata, and T. Karasawa. Three-dimensional effects on shock wave reflections in steady flows. *37th AIAA Aerospace Sciences Meeting and Exhibit*, 1999.

N. Sudani, M. Sato, T. Karasawa, J. Noda, A. Tate, and M. Watanabe. Irregular effects on the transition from regular to Mach reflection of shock waves in wind tunnel flow. *Journal of Fluid Mechanics*, 459:167–185, 2002.

N. Sudani, M. Sato, T. Karasawa, H. Kanda, and N. Toda. Irregular phenomena of shock reflection transition in a conventional supersonic wind tunnel. *AIAA Journal*, 41(6), 2003.

C. VanDercreek. Hypersonic application of Focused Schlieren and deflectometry. *Master of Science Thesis, University of Maryland,*, 2010.

L.M. Weinstein. Review and update of lens and grid Schlieren and motion camera Schlieren. *The European Physical Journal Special Topics*, 182:69–95, 2010.

Appendix A

Technical Drawings

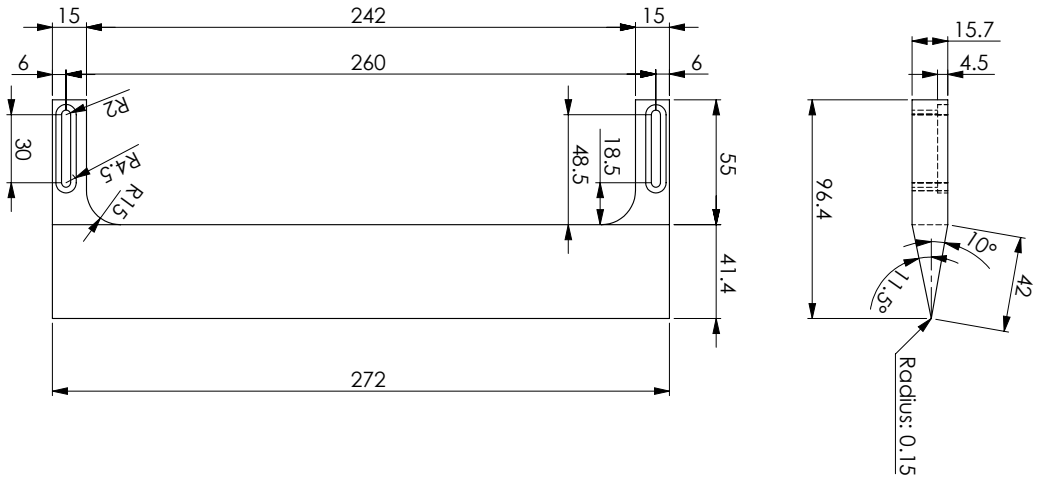

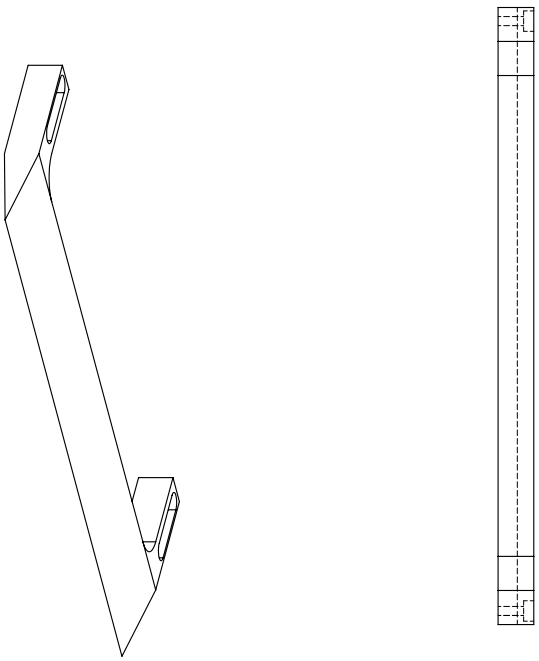

Figure A.1: Bottom 10° wedge

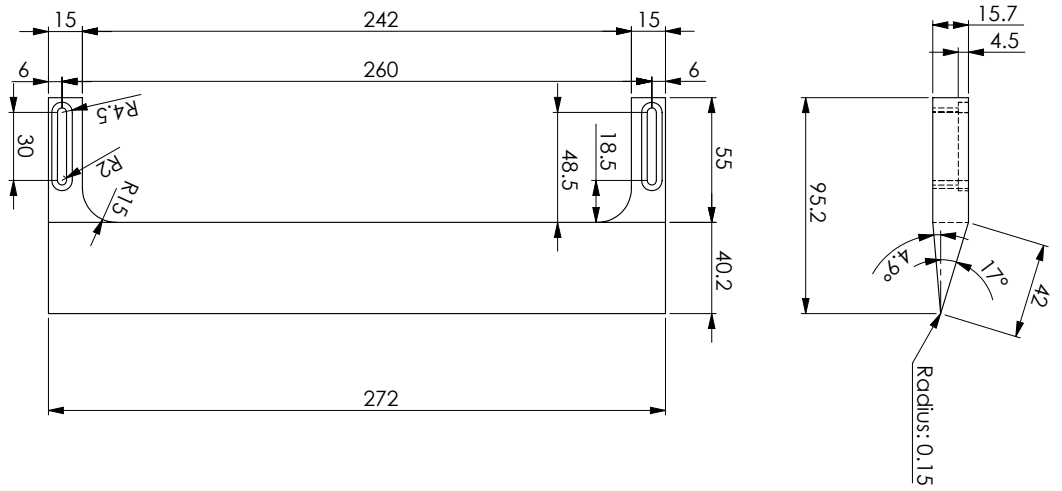

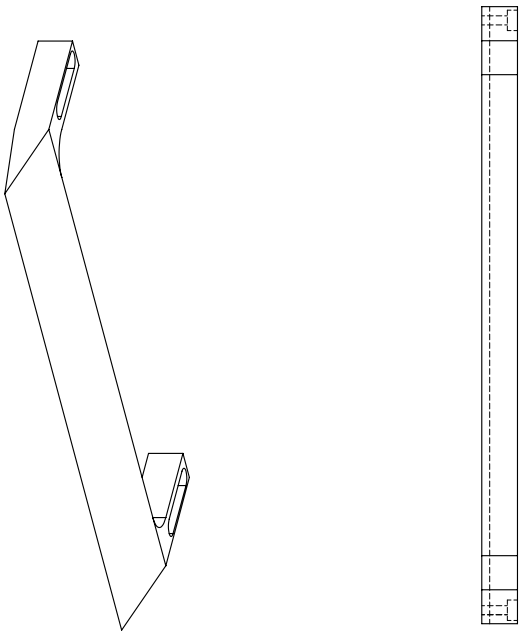

Figure A.2: Bottom 17° wedge

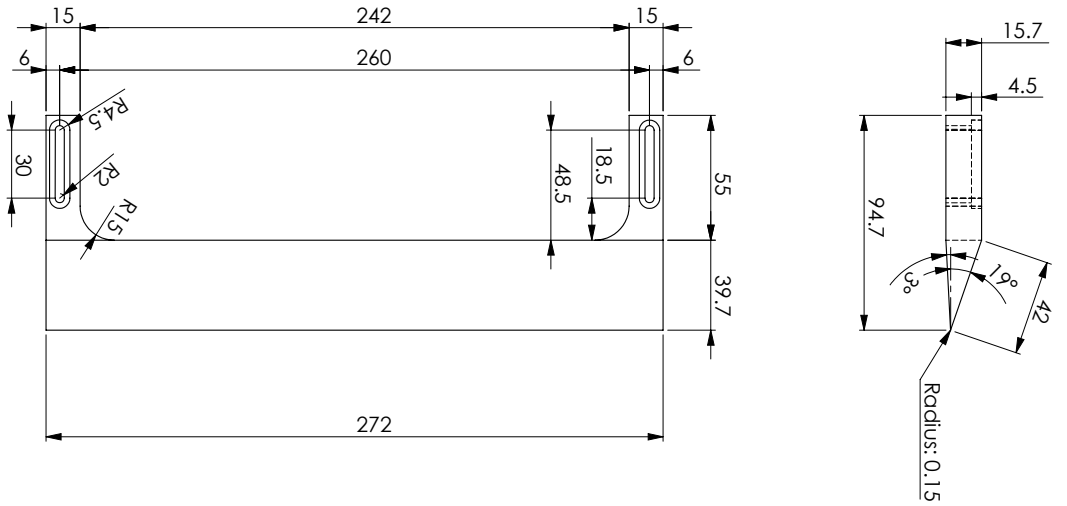

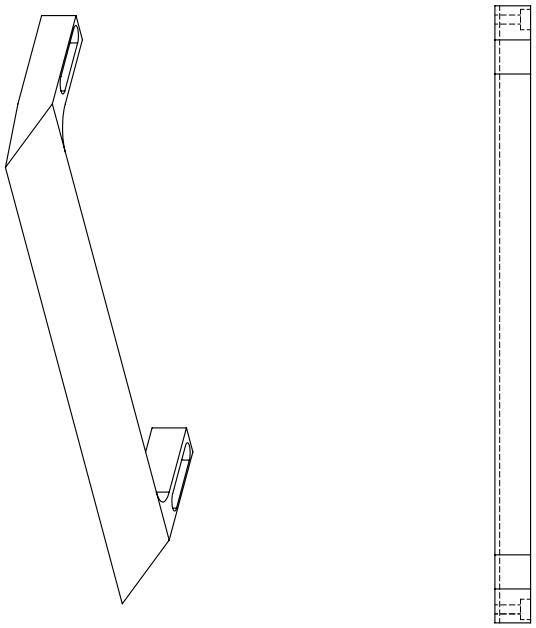

Figure A.3: Bottom 19° wedge

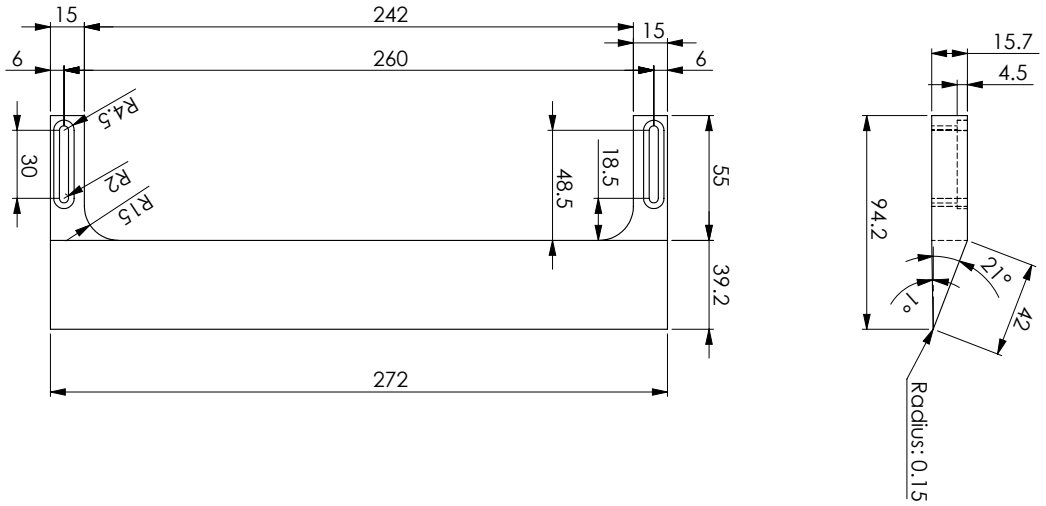

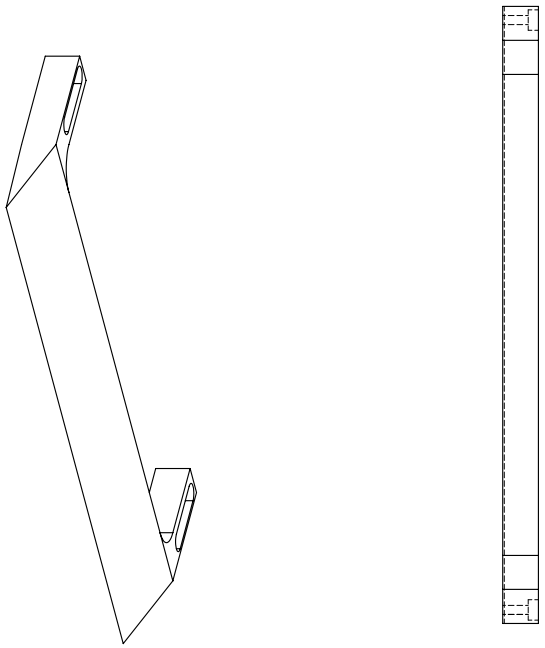

Figure A.4: Bottom 21° wedge

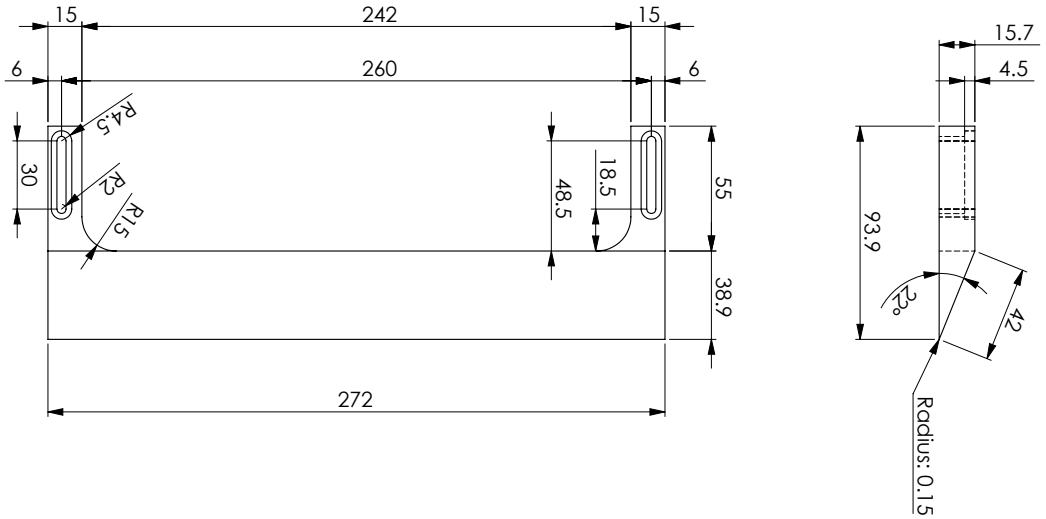

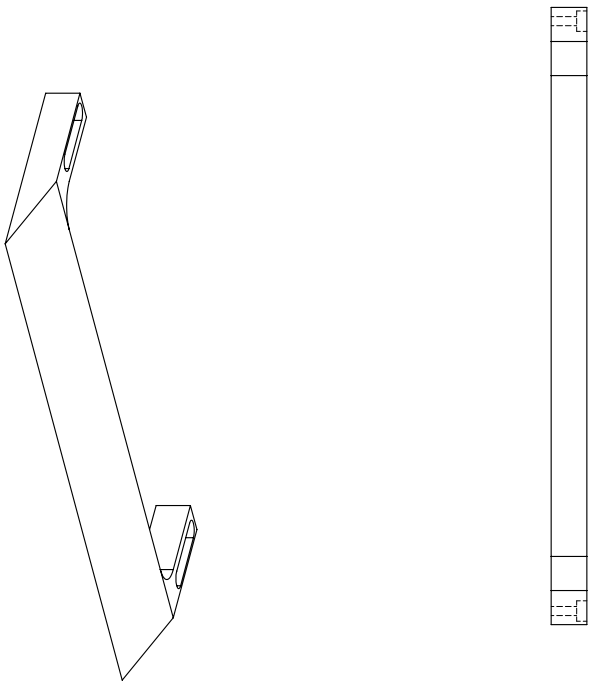

Figure A.5: Bottom 22° wedge

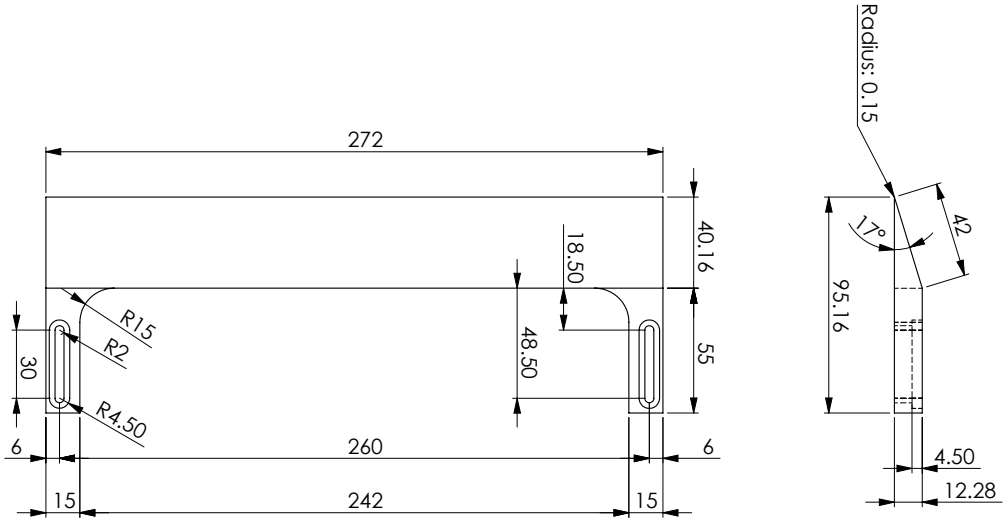

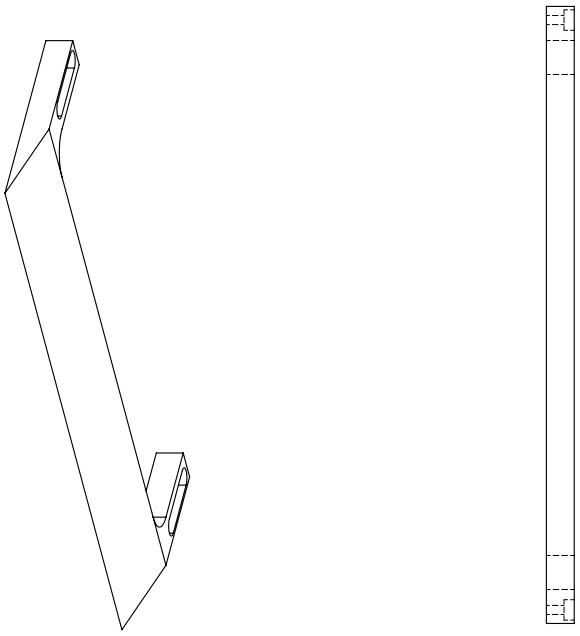

Figure A.6: Top 17° wedge

Appendix B

Focusing Schlieren Images

B.1 Geometry 1 ($\theta_{1N} = 17°$, $\theta_{2N} = 22°$):

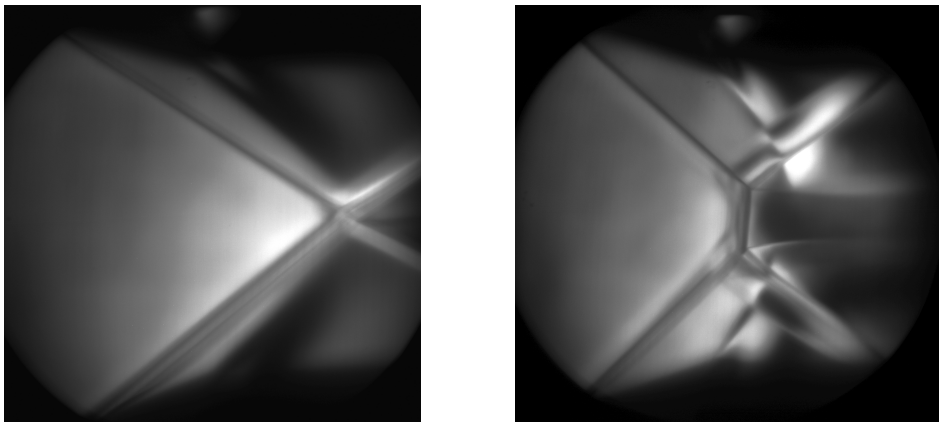

(a) RI configuration

(b) MI configuration

Figure B.1: RI and MI shock patterns observed with the Focusing Schlieren system for the $\theta_{1N} = 17°$, $\theta_{2N} = 22°$ geometry.

B.2 Geometry 2 ($\theta_{1N} = 17°$, $\theta_{2N} = 21°$):

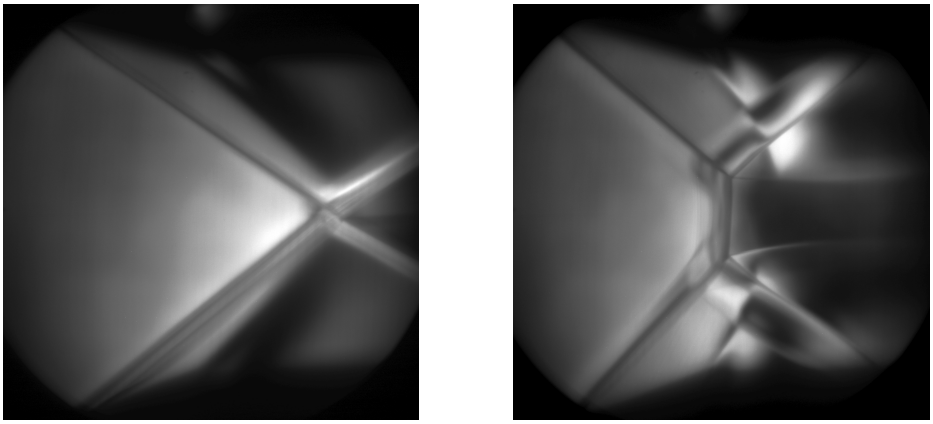

(a) RI configuration (b) MI configuration

Figure B.2: RI and MI shock patterns observed with the Focusing Schlieren system for the $\theta_{1N} = 17°$, $\theta_{2N} = 21°$ geometry.

B.3 Geometry 3 ($\theta_{1N} = 17°$, $\theta_{2N} = 19°$):

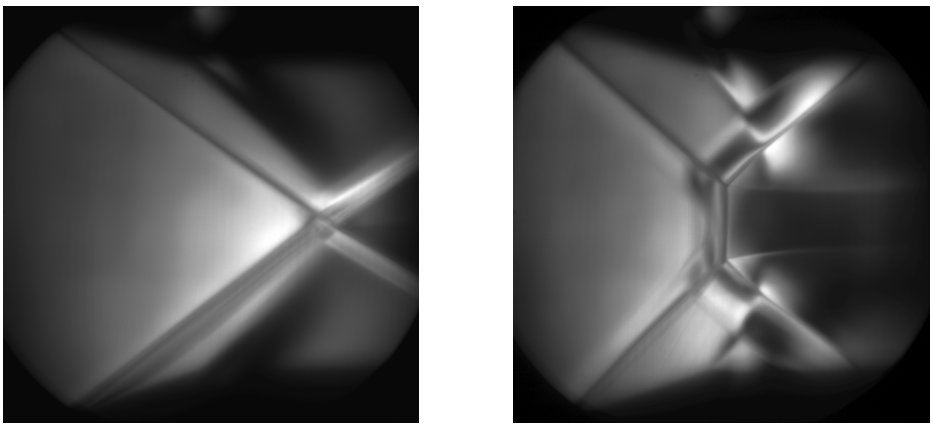

(a) RI configuration (b) MI configuration

Figure B.3: RI and MI shock patterns observed with the Focusing Schlieren system for the $\theta_{1N} = 17°$, $\theta_{2N} = 19°$ geometry.

B.4 Geometry 4 ($\theta_{1N} = 17°$, $\theta_{2N} = 17°$):

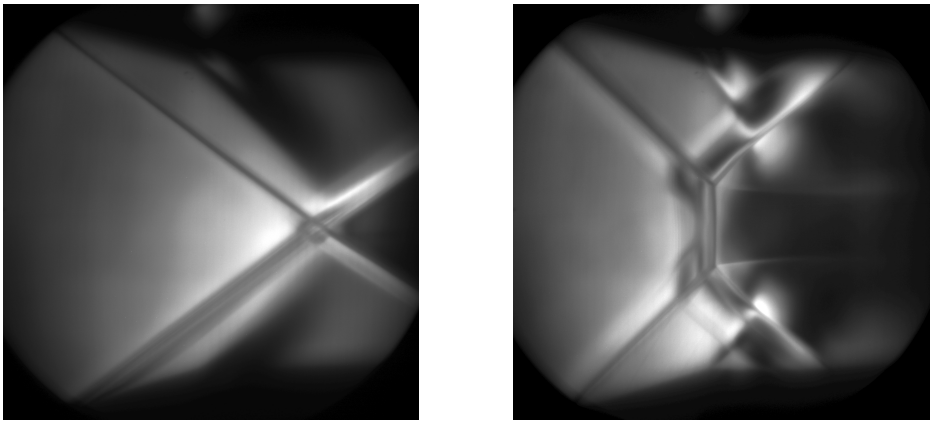

(a) RI configuration (b) MI configuration

Figure B.4: RI and MI shock patterns observed with the Focusing Schlieren system for the $\theta_{1N} = 17°$, $\theta_{2N} = 17°$ geometry.

B.5 Geometry 5 ($\theta_{1N} = 17°$, $\theta_{2N} = 10°$):

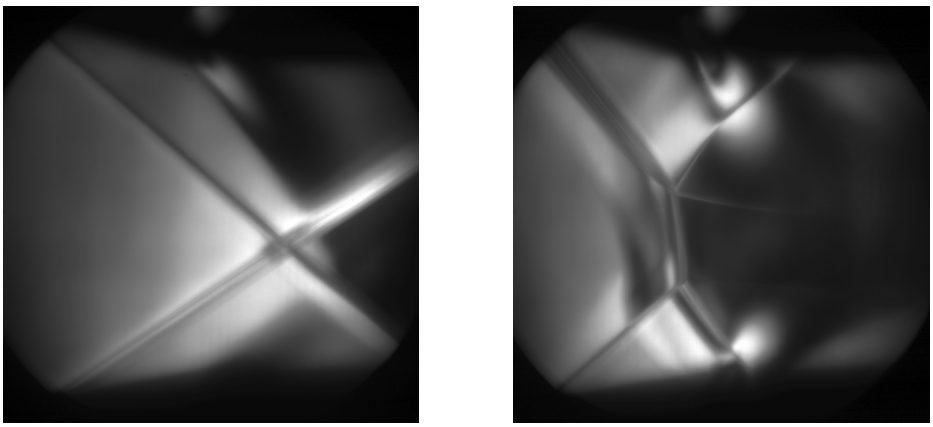

(a) RI configuration (b) MI configuration

Figure B.5: RI and MI shock patterns observed with the Focusing Schlieren system for the $\theta_{1N} = 17°$, $\theta_{2N} = 10°$ geometry.

Appendix C

Complete Uncertainty Estimations

Table C.1: Estimated uncertainty for the measured M_0 and computed ϕ and θ for all runs.

Geometry			**Uncertainty**				
θ_{1N}	θ_{2N}	Run	ΔM_0	$\Delta\phi_1$	$\Delta\phi_2$	$\Delta\theta_1$	$\Delta\theta_2$
17°	22°	1	$7 \cdot 10^{-4}$	0.2°	0.1°	0.2°	0.1°
17°	22°	2	$8 \cdot 10^{-4}$	0.2°	0.1°	0.1°	0.1°
17°	22°	3	$5 \cdot 10^{-4}$	0.2°	0.1°	0.2°	0.1°
17°	22°	4	$8 \cdot 10^{-4}$	0.1°	0.1°	0.1°	0.1°
17°	22°	5	$8 \cdot 10^{-4}$	0.2°	0.1°	0.2°	0.1°
17°	21°	1	$7 \cdot 10^{-4}$	0.2°	0.1°	0.2°	0.1°
17°	21°	2	$6 \cdot 10^{-4}$	0.2°	0.1°	0.2°	0.1°
17°	21°	3	$3 \cdot 10^{-4}$	0.2°	0.1°	0.2°	0.1°
17°	21°	4	$6 \cdot 10^{-4}$	0.2°	0.1°	0.2°	0.1°
17°	21°	5	$4 \cdot 10^{-4}$	0.2°	0.1°	0.2°	0.1°
17°	19°	1	$8 \cdot 10^{-4}$	0.4°	0.2°	0.4°	0.1°
17°	19°	2	$5 \cdot 10^{-4}$	0.4°	0.2°	0.4°	0.1°
17°	19°	3	$1 \cdot 10^{-3}$	0.4°	0.2°	0.4°	0.1°
17°	19°	4	$6 \cdot 10^{-4}$	0.4°	0.1°	0.4°	0.1°
17°	19°	5	$1 \cdot 10^{-3}$	0.4°	0.2°	0.4°	0.1°
17°	17°	1	$5 \cdot 10^{-4}$	0.3°	0.1°	0.3°	0.1°
17°	17°	2	$1 \cdot 10^{-3}$	0.4°	0.1°	0.4°	0.1°
17°	17°	3	$4 \cdot 10^{-4}$	0.4°	0.2°	0.3°	0.1°
17°	17°	4	$6 \cdot 10^{-4}$	0.4°	0.2°	0.3°	0.1°
17°	17°	5	$6 \cdot 10^{-4}$	0.4°	0.2°	0.3°	0.1°
17°	10°	1	$7 \cdot 10^{-4}$	0.2°	0.1°	0.2°	0.1°
17°	10°	2	$3 \cdot 10^{-4}$	0.2°	0.1°	0.2°	0.1°
17°	10°	3	$3 \cdot 10^{-4}$	0.3°	0.1°	0.2°	0.1°
17°	10°	4	$3 \cdot 10^{-4}$	0.2°	0.1°	0.2°	0.1°
17°	10°	5	$7 \cdot 10^{-4}$	0.2°	0.1°	0.2°	0.1°

Appendix D

MSH Evolution Curves

This Appendix presents the MSH evolution curves that do not appear in the main part of this report. The MSH curve for Run 1 can be found in Section 5.3 of the main report.

D.1 MSH Evolution, Run 2

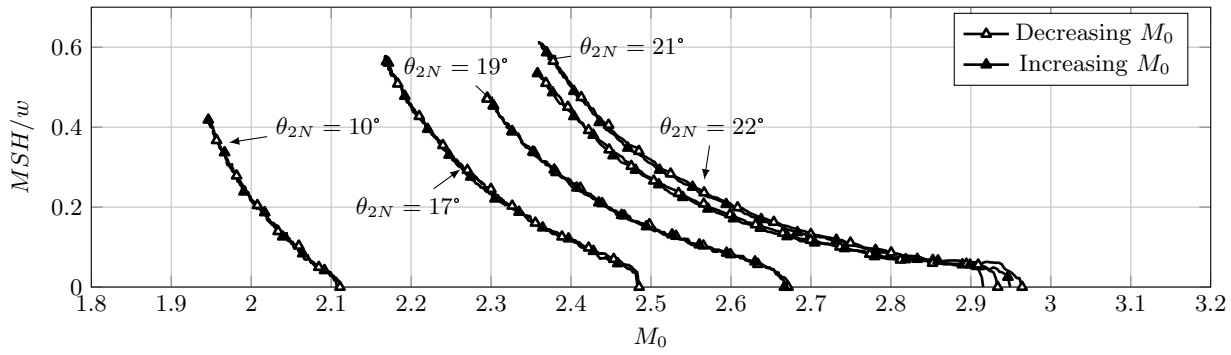

Figure D.1: Evolution of the normalized MSH with M_0 for all geometries, run 2.

D.2 MSH Evolution, Run 3

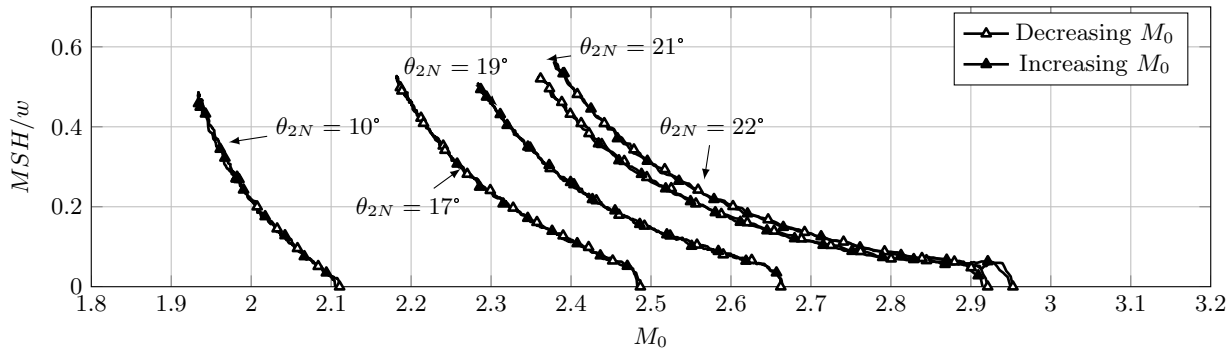

Figure D.2: Evolution of the normalized MSH with M_0 for all geometries, run 3.

D.3 MSH Evolution, Run 4

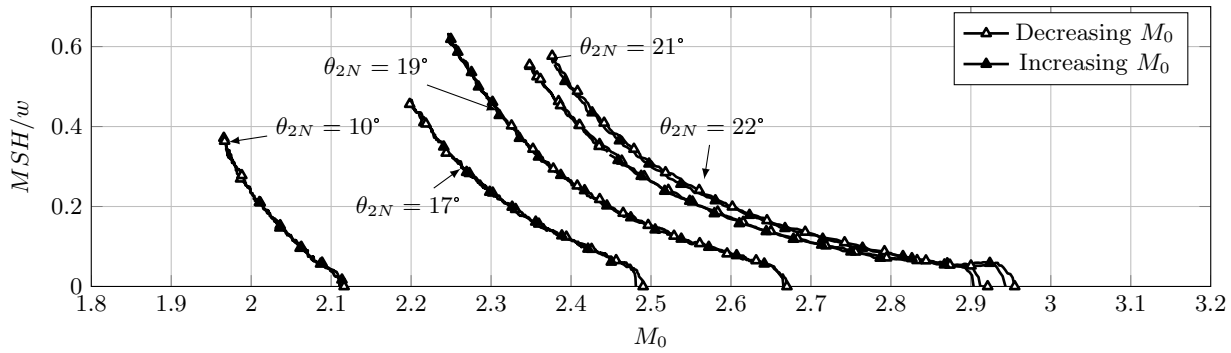

Figure D.3: Evolution of the normalized MSH with M_0 for all geometries, run 4.

D.4 MSH Evolution, Run 5

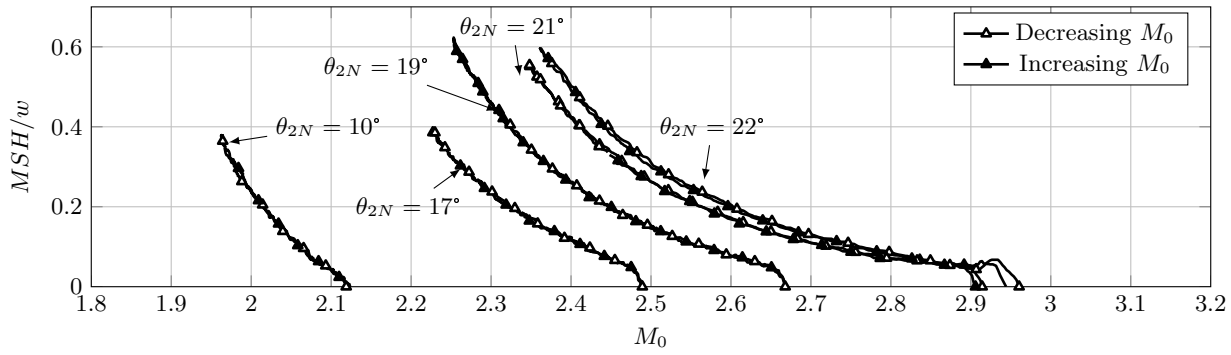

Figure D.4: Evolution of the normalized MSH with M_0 for all geometries, run 5.

Appendix E

Complete Transition Results

Table E.1: Transition points detected for all geometries and runs.

Geometry			RI to MI			MI to RI		
θ_{1N}	θ_{2N}	Run	θ_{1T}	θ_{2T}	M_{0T}	θ_{1T}	θ_{2T}	M_{0T}
17°	22°	1	16.0°	22.9°	2.95	15.9°	22.8°	2.94
17°	22°	2	16.1°	22.9°	2.96	15.9°	22.8°	2.95
17°	22°	3	16.0°	22.9°	2.95	16.0°	22.8°	2.95
17°	22°	4	16.0°	22.9°	2.95	15.9°	22.8°	2.94
17°	22°	5	16.0°	22.9°	2.95	15.9°	22.8°	2.94
17°	21°	1	16.1°	22.5°	2.93	16.0°	22.4°	2.92
17°	21°	2	16.0°	22.6°	2.92	15.9°	22.5°	2.92
17°	21°	3	16.0°	22.5°	2.93	15.9°	22.4°	2.92
17°	21°	4	16.0°	22.5°	2.92	15.9°	22.4°	2.91
17°	21°	5	15.9°	22.5°	2.91	15.8°	22.4°	2.90
17°	19°	1	16.4°	20.5°	2.67	16.4°	20.4°	2.67
17°	19°	2	16.4°	20.4°	2.67	16.3°	20.4°	2.67
17°	19°	3	16.3°	20.4°	2.66	16.2°	20.4°	2.66
17°	19°	4	16.4°	20.5°	2.67	16.4°	20.4°	2.67
17°	19°	5	16.4°	20.4°	2.67	16.3°	20.4°	2.67
17°	17°	1	16.4°	18.3°	2.49	16.4°	18.2°	2.48
17°	17°	2	16.5°	18.3°	2.48	16.4°	18.2°	2.48
17°	17°	3	16.5°	18.3°	2.49	16.4°	18.2°	2.48
17°	17°	4	16.4°	18.2°	2.49	16.5°	18.2°	2.48
17°	17°	5	16.5°	18.2°	2.49	16.4°	18.1°	2.49
17°	10°	1	16.9°	11.3°	2.11	16.8°	11.3°	2.11
17°	10°	2	16.9°	11.3°	2.11	16.8°	11.3°	2.11
17°	10°	3	16.8°	11.3°	2.11	16.9°	11.3°	2.11
17°	10°	4	16.9°	11.4°	2.12	16.9°	11.4°	2.11
17°	10°	5	16.9°	11.4°	2.12	16.9°	11.4°	2.12